CONTROLLING NITROGEN-VACANCY CENTER SPINS WITH A MECHANICAL RESONATOR

A Dissertation

Presented to the Faculty of the Graduate School

of Cornell University

in Partial Fulfillment of the Requirements for the Degree of

Doctor of Philosophy

by

Evan R. MacQuarrie

May 2017

CONTROLLING NITROGEN-VACANCY CENTER SPINS WITH A MECHANICAL RESONATOR

Evan R. MacQuarrie, Ph.D.

Cornell University 2017

The spin state of the nitrogen-vacancy (NV) center in diamond offers a promising platform for the development of quantum technologies and investigations into spin dynamics at the nanoscale. With a lengthy coherence time even at room temperature, NV centers enable precision metrology with atomic scale spatial resolution and present one path towards quantum information in the solid state. These applications require coherent control of the NV center spin state, and this can be achieved with resonant magnetic fields, electric fields, or, at cryogenic temperatures, optical fields. In this thesis, we demonstrate direct mechanical control of NV center spins by coherently driving magnetically-forbidden spin transitions with the resonant lattice strain generated by a mechanical resonator. We then employ mechanical driving to perform continuous dynamical decoupling and extend the inhomogeneous dephasing time of a single NV center spin. Finally, we demonstrate and quantify a spin-strain coupling within the NV center room temperature orbital excited state and propose a dissipative protocol to cool a mechanical resonator mode using this interaction. The methods of mechanical spin control developed here unlock a new degree of freedom within the NV center Hamiltonian that may enable new sensing modes and could provide a route to NV center-mechanical resonator hybrid quantum systems.

BIOGRAPHICAL SKETCH

Strictly speaking, an ensemble average of the days Evan MacQuarrie spent in graduate school would place him approximately 186 km underneath the Treasure Isle RV Park in Blossvale, NY. Omitting time spent outside of Ithaca, however, we find that his center of mass rests above the Earth's surface, and a typical day in his life starts with an 8:08 buzz from his alarm clock. His peace disturbed, he ambulates into the kitchen to pour himself a bowl of Raisin Bran Crunch in equal parts superstition and 2% milk. After a quick devotion to the hygiene overlords, he heads up Gun Hill on his daily commute. Winter chill and summer sweat average to a happy arrival in his basement office of Cornell University's Physical Sciences Building, and two mugs of coffee later, his day's launch sequence is complete.

In deference to the reader's patience, we won't fill this account with the tedium of daily work. Instead, while Evan keys away Mathematica code, aligns a sample in his confocal microscope, or wires up a new LabVIEW VI, we'll leave him to his efforts and diverge into the personal history that led him here.

Born in Nova Scotia, Canada, Evan spent the first years of his life watching sailboats race across Musquodoboit Harbour. He and his family migrated to the rural city of Shelbyville, Tennessee, before he learned how to spell the name of his Canadian hometown, and twelve years later, Evan graduated from Shelbyville Central High School. He spent his next four years at Vanderbilt University where he earned a B.A. in Physics and Mathematics, discovered an appreciation for country music, and uncovered a passion for experimental physics. The last of these led him to Cornell University in the gorge-country of Ithaca, New York, where the coffee is wonderful and the science is world-class.

The facts of a person's life don't always reveal the character beneath. To really get an idea of who Evan is, try asking him what his biggest fear is. If you're lucky enough to get an honest response, he'll tell you that one of the things that scares him the most is dying without having discovered his favorite author. That won't be him reproaching the novels he's had the pleasure of reading. Rather, it will be an acknowledgement that there is likely some story out there that resonates with him more strongly than Bolaño's *2666*, Neuman's *Traveler of the Century*, or any Borges story. In that sense, his response will be both a hopeful wish for things to come and a tragic reminder that life is short and we can never stop exploring. Extrapolating, we begin to understand why he travels as frequently as he can and why he has George Steiner's epigram "Trees have roots and I have legs" tattooed on his bed frame.

Ask him where his interest in quantum mechanics came from, and he might respond with a story of his first encounter with the double slit experiment. In the sci-fi thriller *Timeline*, Michael Crichton jumps from interference fringes to parallel universes, and a pre-teen Evan wanted to do the same. Unfortunately, a primitive understanding of length scales led to a null result. It turns out centimeter-wide slits cut into a cereal box don't significantly diffract a flashlight's beam. They do make pretty mediocre windows though.

Finish off your hypothetical interrogation by asking Evan what he is most proud of. He'll respond by first commending you for breaking the fascist grammarian's rule about ending sentences with prepositions. You'll then hear about a deck of cards he's been cultivating for almost a decade. At the time of writing, his deck contains eighteen and a half cards with only two pairs of duplicates. From Vietnam to Scotland, each card was found discarded in some country or another, often covered in dirt or half disintegrated in a puddle. Whether or not

this novelty is actual Evan's proudest accomplishment will be left for you to decide. As for myself, I choose to see it as a symptom of ataraxia, a condition Evan's been trying to contract for years.

Let's head back to the lab. Knocking on the door of Room B76, we see that Evan has finished off another day's work. He's heading home now to have a quick meal and his evening coffee. Then it's off to The Rink for an hour and a half of pick up hockey. He'll be back home by ten to spend time hanging from a hammock on his front porch, Genny Bock in hand, with friends and conversation bouncing around the rafters. Around midnight, the group will disperse, and Evan will spend the final hour of the day reading whatever novel he's nose deep in now, hoping to find his favorite author before time runs out.

Thanks to everyone who has made this work possible,
my time at Cornell enjoyable, and my life meaningful.

You are Ithaca. You are the journey.

– Andrés Neuman (*Traveler of the Century*)

ACKNOWLEDGEMENTS

To the members of my special committee, Professors Greg Fuchs, Dan Ralph, and Erich Mueller: thank you for your interest and support throughout the course of this project. I would like to extend a special thanks to Greg, who has served as an incredible adviser for the past five years. His infectious excitement around lab and genuine love for physics have made his group an invigorating and satisfying place to work. I hope that as my career continues to develop, I will be able to emulate his passionate and patient approach to teaching.

To fellow Fuchs group members, past and present: thanks for making the lab a great place to work. Thanks for the discussions, the happy hours, and the innumerable pots of coffee. In the future, please break down and recycle your empty cardboard boxes.

To Tanay Gosavi and Sunil Bhave: thanks for the friendship and for sharing your vast knowledge of mechanical resonators. To Matt Otten and Stephen Gray: thanks for providing a firm footing for our sally into theory. To Nate Ellis: thanks for the machine shop wisdom and all the great conversations. To Steve Kriske: thanks for your help with all the CCMR tools.

To my "Fallen Creek Family" (Ed Lochocki, Greg Stiehl, Jason Bartell, Lena Bartell, Summer Saraf, Sam Ahles, Eamonn O'Shea, Jessica Burton) and to my other friends in Ithaca (Maggie Chu, Dan Gonnella, Nick Jungwirth, Pranav Gupta, IAHA, CURH, and the Morning Rooster's crew) and elsewhere (Nick Alexander, Kevin Deweese, Mark Overcast): thanks for making the past six years incredible. It's been a blast.

And to my family: thanks for your support and patience throughout my grad school adventure. The shared vacations, relaxing trips home, and regular

phone calls were key moments of unplugged relief that helped keep me sane throughout this whole ordeal.

TABLE OF CONTENTS

LIST OF TABLES

LIST OF FIGURES

CHAPTER 1

INTRODUCTION

The nitrogen-vacancy (NV) center in diamond forms when a substitutional nitrogen impurity neighbors a vacancy within the diamond lattice (Fig. 1.1a). Electrons trapped at the vacancy form a either a neutral NV^0 or a negatively charged NV^- bound molecular state with ground and excited state orbitals lying inside the diamond band gap [6, 7]. The defect levels of the NV^- (hereafter NV) complex contain a triplet spin degree of freedom, and spin-dependent relaxation rates through an intersystem crossing into a singlet state enable optical initialization and fluorescence dependent readout of the spin state. Specifically, pumping the phonon sidebands of the orbital transition with a 532 nm laser initializes the spin state into $|(m_s =)0\rangle$. This same $|0\rangle$ state fluoresces more brightly than the $|\pm 1\rangle$ states under 532 nm illumination, enabling quantitative readout of the NV center spin state. This landscape is summarized schematically in Fig. 1.1b.

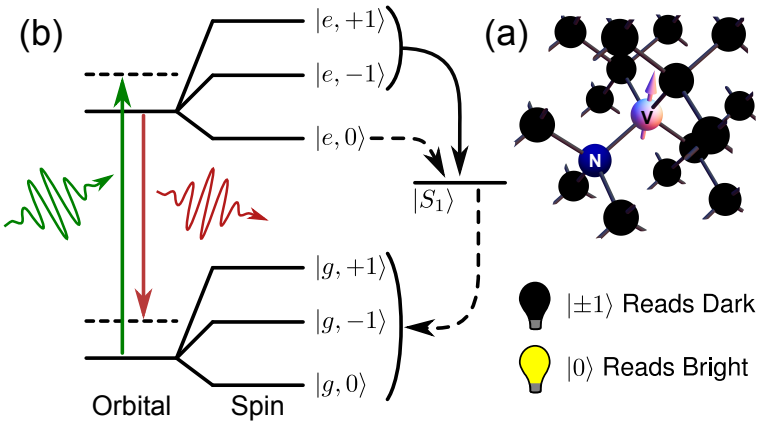

Figure 1.1: (a) Schematic of an NV center. (b) NV center level structure. Fast (slow) relaxation rates are indicated by solid (dashed) lines.

Due in part to diamond's low spin-orbit coupling, the electronic spin coherence times of NV centers can be very long, even approaching one second at

room temperature in isotopically-purified samples [8]. This has motivated the use of NV centers in quantum metrology, where the coherence time of a sensing qubit can dictate the precision of the measurement. Moreover, the defect's well-understood Hamiltonian and atomic size enable quantitative sensing with sub-nanometer spatial resolution. To date, the NV center has been demonstrated as a high performance magnetometer [9, 10, 11, 12], thermometer [13, 14, 15], and electrometer [16] in proof of principle experiments.

NV centers have also found application in quantum information technologies as solid state qubits [17, 18, 19]. In this realm, multiple methods of coupling to the NV center spin state make it a promising candidate for use as a node in a hybrid quantum network [20, 21, 22]. In such a system, an NV center could operate as a quantum transducer, translating information between disparate quantum degrees of freedom. To achieve such a conversion, the NV center spin must coherently couple to another quantum state.

At cryogenic temperatures, the NV center can coherently couple to photonic states through its orbital [23, 24] or spin [25, 26, 27, 28] degrees of freedom. It can also couple to phononic states via either an orbital-strain interaction within the excited state orbital manifold [29, 30] or a spin-strain interaction within the ground state [1, 31, 32, 2, 33]. The NV center orbital transition loses coherence for temperatures greater than ~ 10 K due to interactions with phonons [34]. Therefore, at room temperature, the spin state is the only coherent degree of freedom left to the NV center. A room temperature NV center can still directly couple to the phononic state of a mechanical resonator [1, 31, 32, 2, 33]. This spin-strain interaction is the focus of this thesis.

Original efforts to couple NV center spins and mechanical resonators used magnetic fields to mediate an interaction between the resonator and the spin [35, 20, 36, 37, 38, 39, 40]. Experimentally, this has been accomplished by either attaching an NV center to a large-amplitude mechanical resonator in the presence of an external magnetic field gradient [36] or by fabricating cantilevers with magnetized tips and placing a fixed NV center beneath the oscillating tip [37, 38, 39]. These approaches typically employ a longitudinal coupling of the magnetic field to the NV center spin energies through the Zeeman interaction and have been demonstrated as efficient methods for measuring the oscillation amplitude of the mechanical resonator. However, the precise alignment required by such indirect coupling protocols limits the scalability of these systems.

As an alternative to longitudinal spin-phonon coupling mediated by a magnetic field, we consider an intrinsic, transverse interaction that uses resonant lattice strain to directly mix the NV center spin eigenstates and enable coherent mechanical spin driving. This coupling is a manifestation of the spin-spin interaction between the two electrons comprising the NV center triplet state [7]. In the quantized resonator limit, the interaction can be written in a Jaynes-Cummings form where a spin flip up (down) corresponds to phonon annihilation (creation). This approach has motivated theoretical proposals that apply this intrinsic spin-phonon interaction to achieve spin-squeezing for enhanced magnetometry [41] or phonon lasing and cooling in a mechanical resonator [42]. In this thesis, we make the first forays into experimentally accessing this interaction, laying the foundations for future NV center spin-mechanical systems.

The layout of the thesis is as follows: In Chapter 2, we discuss the procedures for fabricating and characterizing the mechanical resonators used in this thesis. Chapter 3 describes the confocal microscope and microwave electronics used in our measurements. In Chapter 4, we present the first demonstration of mechanically driven spin transitions in NV centers. We extend these results to include coherent control of NV centers with a mechanical resonator in Chapter 5. Chapter 6 uses this coherent mechanical control to protect a single NV center spin from decoherence through a continuous dynamical decoupling protocol. Finally, in Chapter 7, we experimentally discover a spin-strain interaction within the NV center room temperature excited state and theoretically analyze a dissipative protocol that uses this interaction to cool a mechanical resonator to a fraction of its thermal phonon occupancy.

CHAPTER 2

DEVICE FABRICATION

2.1 NV Center Creation

The NV centers measured in this thesis were created by one of two methods. In samples designed to interrogate spin ensembles (Chapters 4, 5, and 7), the NV centers were by-products of the CVD growth process and were present in densities of $\sim 10^{14}$ cm^{-3} as purchased from Element Six Technologies. These diamonds are referred to as "optical grade" diamonds and are quoted by the supplier to contain < 1 ppm of nitrogen impurities.

Measurements of single NV centers were performed in higher purity "electronic grade" diamonds, once again purchased from Element Six Technologies. These diamonds are quoted to contain < 5 ppb of nitrogen impurities and contain a negligible quantity of NV centers as purchased. To create NV centers in a usable density, we irradiate the diamonds with 2 MeV electrons at a fluence of 1.2×10^{14} cm^{-2}, creating lattice vacancies within the diamond. The sample used in Chapter 6 was irradiated by J. Maxson, A. Bartnik, B. Dunham, and I. Bazarov at the Cornell University Cornell Laboratory for Accelerator-Based Sciences and Education (CLASSE). In other devices, the electron irradiation was performed by F. B. Bateman of the NIST Dosimetry Group.

After irradiation, the diamonds were annealed at 850°C for two hours in the Lindberg High Vacuum Furnace at the Cornell Center for Materials Research (CCMR). At this temperature, vacancies migrate within the diamond lattice and get trapped at native substitutional nitrogen impurities, forming NV cen-

ters [43, 44]. After loading the sample, the Lindberg furnace was evacuated to $\sim 10^{-7}$ Torr. For the sample used in Chapter 6, argon was then introduced as an inert background, raising the chamber pressure to ~ 200 mTorr. Other samples were annealed in high vacuum (no Ar). After annealing, the diamonds were cleaned in a $3:2$ mixture of nitric acid and sulfuric acid boiled under reflux for one hour.

Fig. 2.1a shows a photoluminescence map of the NV center distribution at the end of this procedure. The resulting defect density permits the isolation of individual NV centers. Fig. 2.1b displays the emission spectrum of one such defect, verifying its identity as an NV center.

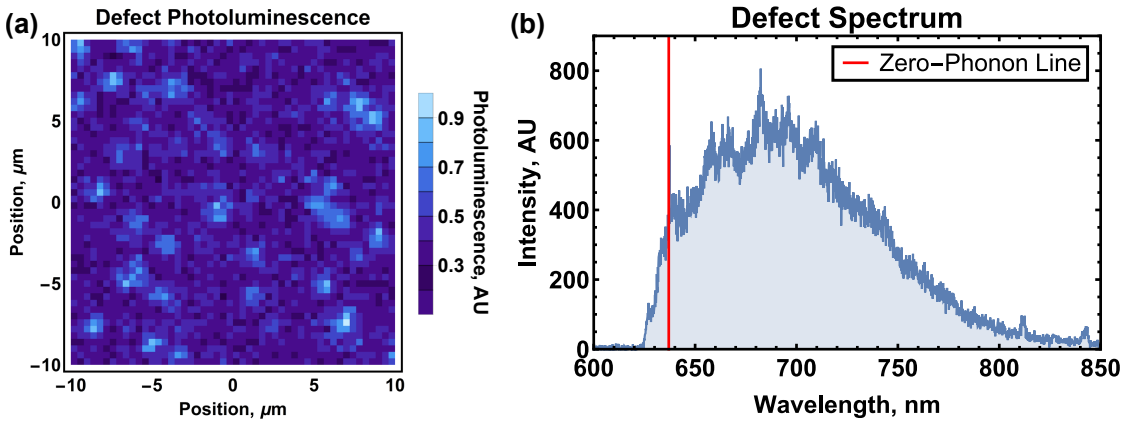

Figure 2.1: (a) Photoluminescence map of NV centers created by electron irradiation and annealing. (b) Spectrum of the photoluminescence emitted from a single NV center created by electron irradiation and annealing.

2.2 Mechanical Resonator Fabrication

The mechanical spin control experiments reported in this thesis used high-overtone bulk acoustic resonators (HBARs) fabricated from single crystal diamond to generate the lattice strain needed to resonantly drive NV center spin

transitions. These bulk mode resonators consist of a piezoelectric film sandwiched between two electrodes on top of a diamond substrate. Applying a high frequency voltage across the piezoelectric launches acoustic waves into the diamond substrate that reflect off the opposite face to form standing wave resonances with large amplitude strain at the antinodes.

The first generation of devices (Chapter 4) was fabricated according to the process flow shown in Fig. 2.2b. We began with a 300 μm thick "optical grade" diamond containing NV centers at a density of $\sim 3 \times 10^{14}$ cm^{-3}. After cleaning the diamond in a $3:2$ mixture of nitric acid and sulfuric acid boiled under reflux for one hour, a 400 μm diameter Ti/Pt ($25/225$ nm) ground electrode was patterned on one face of the diamond substrate by T. A. Gosavi. X-ray diffraction (XRD) (Fig. 2.2b) confirmed the $\langle 111 \rangle$ crystallographic orientation of the Pt film. This was critical for the proper orientation of the piezoelectric AlN film that was sputtered on the Pt to a thickness of 3 μm by OEM Group, Inc. T. A. Gosavi then patterned and evaporated a 100 nm thick Al electrode atop the piezoelectric to complete the HBAR fabrication. The HBAR was then coated in photoresist for protection while a Ti/Pt ($25/225$ nm) magnetic antenna was patterned on the reverse face of the diamond to enable conventional magnetic spin control. Table 2.1 provides the sputtering parameters used for all Ti/Pt films described in this thesis, and Fig. 2.2c,d show the final HBAR and antenna used in the measurements described in Chapter 4. The residue on the devices is thought to be from the inadvertent mixing of LOR lift-off resist and acetone.

In later devices, the AlN piezoelectric layer was replaced by a ZnO film. This was motivated by the ZnO sputtering capabilities at the CCMR that allowed us to perform the entire fabrication in-house. Although the two piezoelectrics per-

Target (Position)	Density	z-ratio	Tooling %	Power	Voltage
Ti (1-Blue)	4.5	0.628	143	100 W	$\sim$ 359 V
Pt (3-Red)	21.4	0.245	115	100 W	$\sim$ 373 V

Target	Current	Pressure	Flow	Rate
Ti	$\sim$ 0.289 A	Ar: 5 mTorr	Ar: 125 sccm	$\sim$ 1.1 Å/s
Pt	$\sim$ 0.26 A	Ar: 5 mTorr	Ar: 125 sccm	$\sim$ 2.8 Å/s

Table 2.1: Parameters for sputtering Ti/Pt films with the CCMR 3-gun sputter system. The Ti target is pre-sputtered for 15 minutes before starting the Ti deposition. The Pt target is pre-sputtered for 10 minutes.

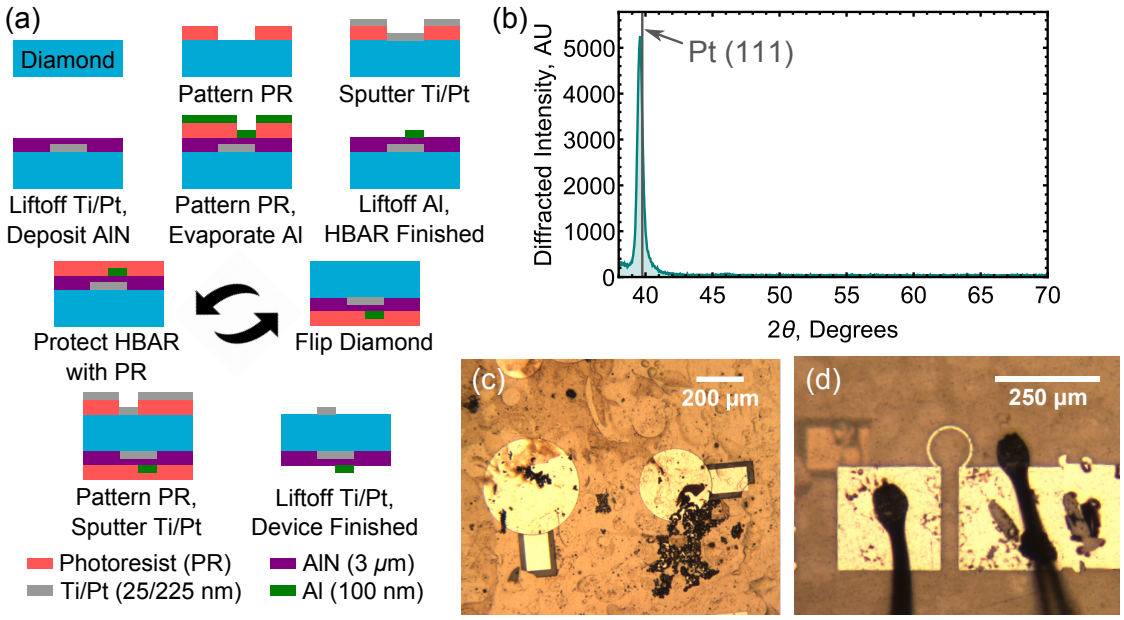

Figure 2.2: (a) Process flow to used to fabricate the first generation of diamond-mechanical resonator devices. (b) XRD measurement of the Pt ground electrode crystallographic orientation. (c,d) The (c) HBAR and (d) magnetic antenna used in the measurements described in Chapter 4.

form comparably, an entirely local fabrication process permitted faster feedback and enabled rapid device development. The devices used in Chapters 5, 6, and 7 were all created with the in-house process flow depicted in Fig. 2.3a. This fabrication once again starts with a one hour clean in a $3:2$ mixture of nitric

Target (Position)	Density	z-ratio	Tooling %	Power	Voltage
Zn (2-Yellow)	5.67	0.556	115	65 W	$\sim$ 387 V

Current	Pressure	Flow	Rate
$\sim$ 0.16 A	Ar: 4 mTorr O_2: 1 mTorr	Ar: 125 sccm O_2: 46.8 sccm	$\sim$ 1.8 Å/s

Table 2.2: Parameters for sputtering ZnO films with the CCMR 3-gun sputter system. The Zn target is pre-sputtered for 5 minutes before starting the O_2 flow. Once the O_2 flow has stabilized, ZnO is pre-sputtered for 30 minutes before starting the deposition.

acid and sulfuric acid boiled under reflux. An unpatterned Ti/Pt (25/200 nm) ground plane was then sputtered on one face of the diamond substrate. XRD measurements confirmed the $\langle 111 \rangle$ orientation of the Pt film (Fig. 2.3b), which was once again critical for proper orientation of the ZnO piezoelectric. Zn was then reactively sputtered in an oxygen background to create a micron-thick ZnO film. The sputter parameters are summarized in Table 2.2. The thicknesses of the ZnO films were confirmed by profilometry measurements taken on calibration chips simultaneously loaded into the chamber. XRD measurements confirmed the proper $\langle 002 \rangle$ orientation of the ZnO films (Fig. 2.3b). We then sputtered a 250 nm thick Al top electrode with a lift-off process to complete the HBAR fabrication (Fig. 2.3c). The sputtering parameters for this Al contact are provided in Table 2.3. We apodized the shape of this top contact by designing it to have no parallel sides. This increases the HBAR efficiency by mitigating the loss of power into lateral resonance modes. Without coating the HBAR in an extra protective layer of photoresist, we flipped over the substrate and fabricated the Ti/Pt (25/225 nm) microwave antenna seen in Fig. 2.3d on the opposite diamond face. The antenna geometry here has been designed to minimize the antenna's footprint within the active region of the HBAR.

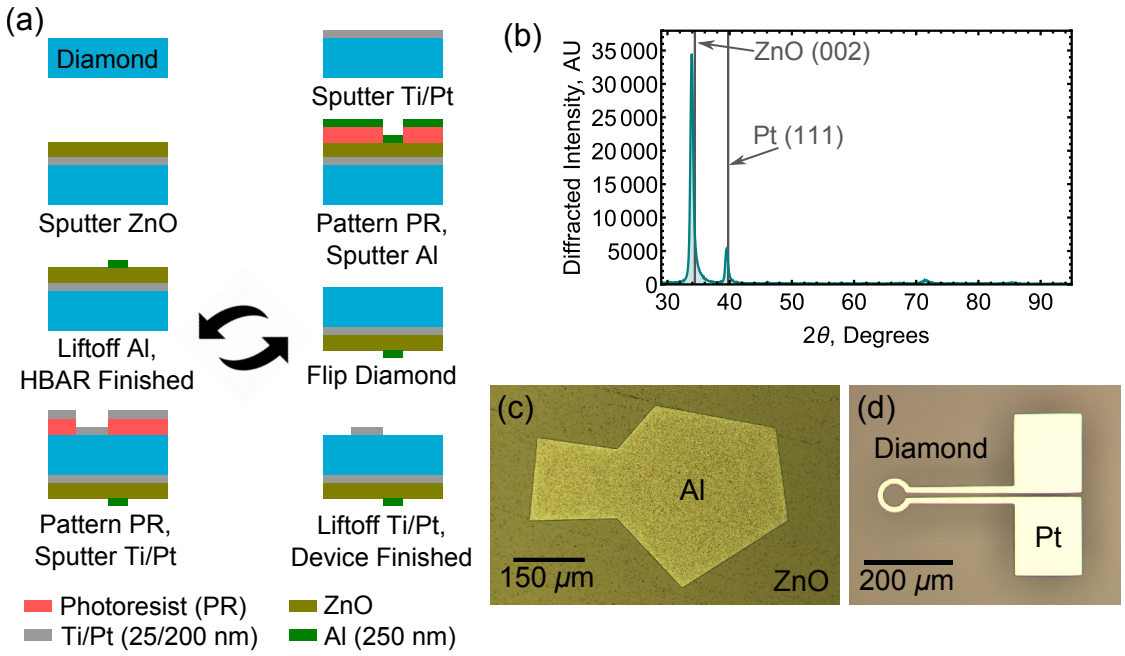

Figure 2.3: (a) Process flow to used to fabricate the second generation of diamond-mechanical resonator devices. (b) XRD measurement of the Pt ground plane and ZnO piezoelectric film crystallographic orientation. (c,d) Examples of the (c) HBAR and (d) magnetic antenna used in second generation devices.

Target (Position)	Density	z-ratio	Tooling %	Power	Voltage
Al (2-Yellow)	2.70	1.08	115	100 W	$\sim$ 392 V

Current	Pressure	Flow	Rate
$\sim$ 0.25 A	Ar: 5 mTorr	Ar: 125 sccm	$\sim$ 1.9 Å/s

Table 2.3: Parameters for sputtering Al films with the CCMR 3-gun sputter system. The Al target is pre-sputtered for 30 minutes before starting the deposition.

2.3 Mechanical Resonator Characterization

After fabrication, devices are mounted in the sample holder pictured schematically in Fig. 2.4. Wire bonds connect the HBAR and antenna to coplanar waveguides (CPWs) on opposite sides of the sample holder, and these CPWs lead to an SMA bulkhead that provides access for a microwave line.

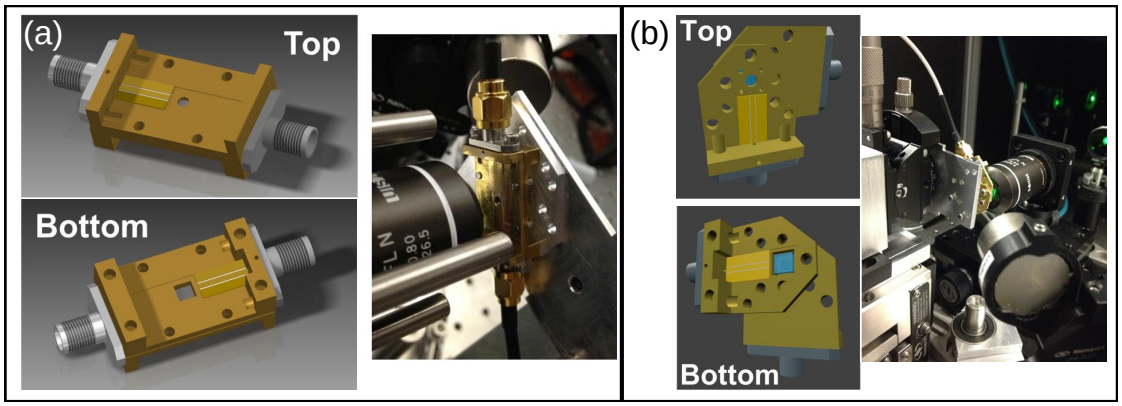

Figure 2.4: (a) First generation sample holder used with AlN-based HBARs. (b) Second generation sample holder used with ZnO-based HBARs.

Vector network analyzer (VNA) measurements of the amplitude $S_{11}^{[dB]}$ and phase $S_{11}^{[\circ]}$ of the power reflected from the HBAR as a function of frequency provide a first means of characterizing the HBAR resonances. Assuming a $Z_0 = 50\ \Omega$ line, the power admitted to the device in siemens is then given by

$$Y_{11}^{[S]} = \left| \frac{1}{Z_0} \frac{1 - S_{11}}{1 + S_{11}} \right| \tag{2.1}$$

with a phase of

$$Y_{11}^{[\circ]} = \frac{180^\circ}{\pi} \arg \left(\frac{1}{Z_0} \frac{1 - S_{11}}{1 + S_{11}} \right) \tag{2.2}$$

where $\arg(x + iy) \equiv \tan^{-1}(y/x)$ takes the argument of a complex number and

$$S_{11} = 10^{S_{11}^{[dB]}/20} \left[\cos \left(S_{11}^{[\circ]} \frac{\pi}{180} \right) + i \sin \left(S_{11}^{[\circ]} \frac{\pi}{180} \right) \right]. \tag{2.3}$$

The target $50\ \Omega$ device impedance corresponds to $Y_{11}^{[S]} = 20$ mS.

We compute the unloaded quality factor Q of the HBAR using the Q-circle method [45]. This is done by performing an S-parameter simulation of the device using Agilent's Advanced Design System (ADS) software. Using the VNA S_{11} data of a particular resonance as input, the simulation tunes the complex impedance of the line to match the device and calculates the group delay $\tau_g(\omega)$.

The Q of the resonance is then given by the expression

$$Q(\omega) = \omega\tau_g \frac{|S_{11}|}{1 - |S_{11}|^2}. \tag{2.4}$$

The works described in Chapters 4, 5, and 6 used this method to calculate the unloaded Q.

In Chapter 7, we use an ensemble of NV centers embedded within the HBAR to directly measure the resonator Q from the ring-up time of the mechanical driving field. This process is described in Sect. 7.3.2.

The amplitude of the strain generated by the HBAR—and hence the mechanical driving field—depends on both the Q and the impedance Z of the resonator mode. The ratio of the strain generated by two different resonator modes is given by

$$r_{strain} = \frac{Q_1}{Q_2} \times \frac{Z_1\sqrt{50\ \Omega + Z_2}}{Z_2\sqrt{50\ \Omega + Z_1}}. \tag{2.5}$$

We use this expression to select the resonance mode predicted to give the largest mechanical driving field.

2.4 Nanomechanical Resonators

The bulk mode resonators used in the experimental portions of this thesis are well-suited for quantum control experiments. Nevertheless, the large phonon occupation of the resonator modes ensures that the generated driving fields can always be treated semi-classically. This is equivalent to saying that although the mechanical resonator can efficiently control an NV center spin, the back-action of the a single spin on the resonator is negligibly small.

To observe quantum effects, the single spin-single phonon coupling strength λ must be much larger than what our bulk mode resonators can achieve. This can be accomplished by finding a stronger spin-phonon coupling within the NV center Hamiltonian, which is the subject of Chapter 7. Another way to increase λ is to replace our bulk mode resonators with nanomechanical resonators that confine the phonon mode to a much smaller volume. This goal of strong coupling has motivated the rapid development nanomechanical resonators fabricated from single crystal diamond [46, 47, 48, 49, 50].

The spin-phonon coupling of an NV center embedded in such a resonator can be predicted analytically using elasticity theory [41, 32]. To motivate future device fabrication, we can consider how λ scales with the physical dimensions of a mechanical resonator for the doubly-clamped beam and cantilever geometries shown in Fig. 2.5. We start with the assumption that the diamond face is $\langle 111 \rangle$ oriented. As indicated in the inset to Fig. 2.5, this ensures that for one orientation of NV centers the strain within the resonator will be entirely perpendicular to the NV center symmetry axis. We can then calculate λ for an NV center embedded within the resonator by computing the strain from the zero-point motion of the mechanical mode.

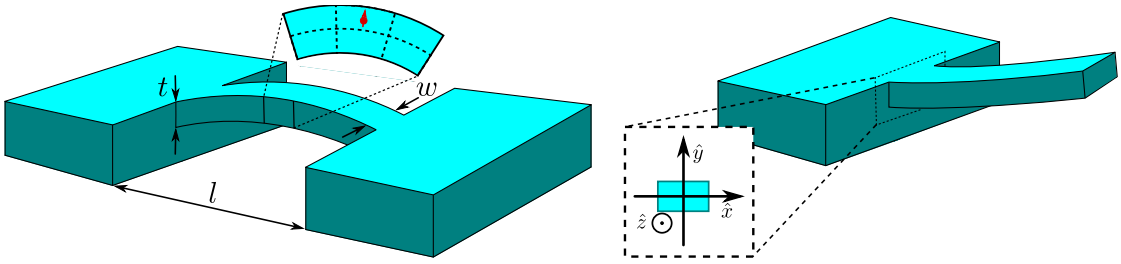

Figure 2.5: Doubly-clamped beam and cantilever geometries treated in our resonator scaling analysis.

For both beams and cantilevers of width w, thickness t, and length l, the wave equation for the mechanical mode is given by

$$\rho_d A \frac{\partial^2}{\partial t^2}\phi(t,z) = -EI\frac{\partial^4}{\partial z^4}\phi(t,z) \tag{2.6}$$

where $\phi(t,z)$ is the transverse displacement in the y-direction, $\hat{z}$ is along the beam as indicated in Fig. 2.5, $A = wt$ is the cross-sectional area of the resonator, $E = 1200$ GPa is the Young's modulus of diamond, $\rho_d = 3.515$ g/cm^3 is the mass density of diamond, and $I = wt^3/12$ is the resonator's moment of inertia. Solutions take the form $\phi(z,t) = u(z)e^{-i\omega t}$ where

$$u_n(z) = \alpha_n\left[(\cos k_n z - \cosh k_n z) - \beta_n\left(\sin k_n z - \sinh k_n z\right)\right]. \tag{2.7}$$

The allowed k-vectors satisfy $\cos(k_n z)\cosh(k_n z) = -1$ for a cantilever and $\cos(k_n z)\cosh(k_n z) = 1$ for a beam. For a cantilever, the wave vector and amplitudes of the first few modes then become $k_n^c l = \kappa_n^c$ where $\kappa_n^c = 1.875, 4.694, 7.855, ...$ and $\beta_n^c = 0.7342, 10.18, 0.9921, ...$, respectively. For a beam, we have $\kappa_n^b = 4.730, 7.853, 11.00, ...$ and $\beta_n^b = 0.9823, 1.001, 1.000$. We normalize $u_n(z)$ by equating the free energy of the resonator with the zero point energy of the mode

$$W = \frac{1}{2}EI\int_0^L \left(\frac{\partial^2 u_n}{\partial z^2}\right)^2 dz = \frac{1}{2}\hbar\omega_n \tag{2.8}$$

where $\omega_n = k_n^2\sqrt{EI/\rho_d A} \propto \kappa_n^2 t/l^2$ is the eigenfrequency of the resonate mode.

The strain from the zero-point motion of this mode is then given by $\epsilon_0(y,z) = -y\frac{\partial^2}{\partial z^2}u_n(z)$, and the spin-phonon coupling for an NV center located at (y,z) is given by $\lambda_s(y,z) = d_\perp \epsilon_0(y,z)$ where $d_\perp$ is the spin-strain coupling strength. Here, we have zeroed the $\hat{y}$-axis at the neutral axis of the resonator. For a fixed fractional location in the beam $(y/t, z/l)$, the spin-strain coupling then scales as $\lambda_s(y) \propto \kappa_n/l\sqrt{lw}$. This motivates the use of short, thin beams to achieve high

single spin-single phonon coupling. Unfortunately, such physical dimensions also bring the NV centers closer to the surface of the diamond, making them more susceptible to dephasing from surface noise [51]. Moreover, shrinking the resonator size increases the frequency of its resonant mode, and the motion of high frequency modes is typically difficult to actuate and detect without reducing the resonator Q [52].

The value of κ_n increases with the mode number, motivating the use of higher order modes to increase the spin-phonon coupling within a given resonator. This provides a means of increasing λ for single NV center coupling. For an ensemble of spins, however, the number of NV centers that contribute to the collective coupling increases with the size of the resonator. This results in λ_{eff} being determined solely by the resonator frequency as seen in Chapter 7. A higher order mechanical mode of a slow resonator thus generates the same λ_{eff} as the fundamental mode of a higher frequency resonator. For both ensembles and single spins, employing higher order mechanical modes could thus increase the required physical dimensions of the resonator, relaxing the fabrication requirements of the device and moving NV centers further from the diamond surface.

CHAPTER 3

MEASUREMENT DETAILS

3.1 Optical Setup and Data Acquisition

The measurements reported in this thesis were performed on the home-built confocal microscope pictured schematically in Fig. 3.1. An Oxxius SLIM 532 nm laser outputs 150 mW that is attenuated by a variable optical density (OD) filter wheel. This is then focused through a Gooch & Housego 15210 acousto-optic modulator that is digitally modulated by a R21210-1DM driver to operate as a high-speed shutter. This driver is in turn modulated by the Channel 1 and 2 outputs of a SRS DG645 digital delay generator (DDG). The AOM modulation signal is sent through a homemade tank circuit to increase the optical extinction ratio. After the AOM, a 532 nm bandpass filter ensures a narrow-line excitation, and an Optics in Motion 101 fast steering mirror (FSM) followed by a $4F$ lens assembly directs the beam through an Olympus LMPLFLN, 100x objective and onto the diamond sample. This objective is positioned on a motorized linear translation stage.

Photoluminescence emitted from the NV centers under interrogation then retraces this path and passes through a dichroic mirror that separates the collection path from the excitation. A 30 μm diameter pinhole provides a spatial filter for the collection, and a 630 nm longpass filter reduces the background signal. The emission is then detected by an Excelitas SPCM-AQRH-13-FC avalanche photodiode (APD).

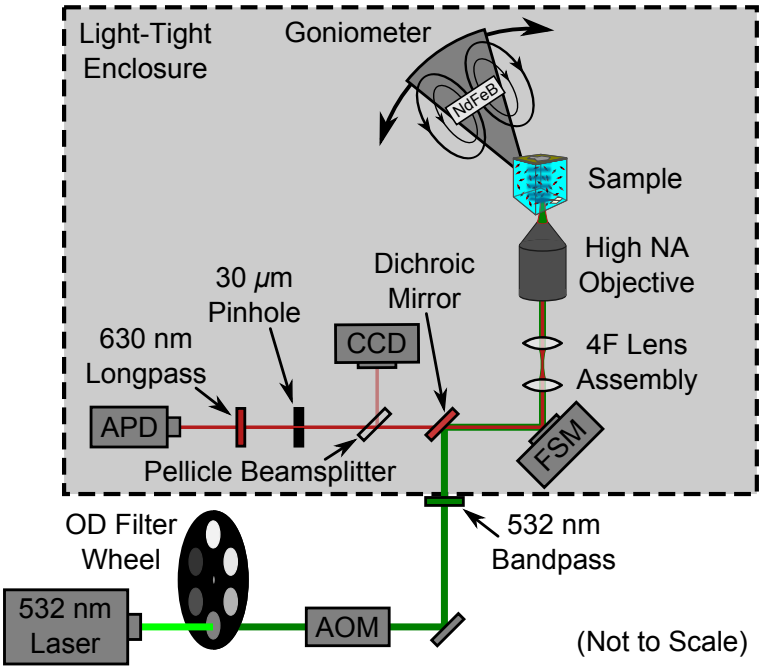

Figure 3.1: Schematic of the confocal microscope used in our measurements

The diamond sample is mounted in a custom-built sample holder (Fig. 2.4), which is in turn mounted on a two-axis goniometer that sits atop a three-axis stage. The three-axis stage allows for course sample positioning, while fine positioning is provided by the FSM and by moving the objective. The two-axis goniometer enables alignment of the sample such that one of the $\langle 111 \rangle$ diamond axes lies in the plane of the optical table. A NdFeB permanent magnet positioned on a home-built goniometer is then aligned to this axis, spectrally isolating the family of NV centers oriented along this $[111]$ axis. The permanent magnet's angular and radial motion are controlled by a pair of motorized linear actuators.

Upon the detection of a single photon, the APD outputs a 10 ns wide, ~ 2.2 V pulse. We send this pulse though the cascade of RF switches shown in Fig. 3.2 to sort the pulses before collecting them in different counters on our NI PCIe-6323 DAQ card. Channels 3 and 4 of our DDG as well as a Tektronix AFG3102

arbitrary waveform generator route the pulses through the cascade. The right branch of switches was only used in the continuous dynamical decoupling experiments described in Chapter 6.

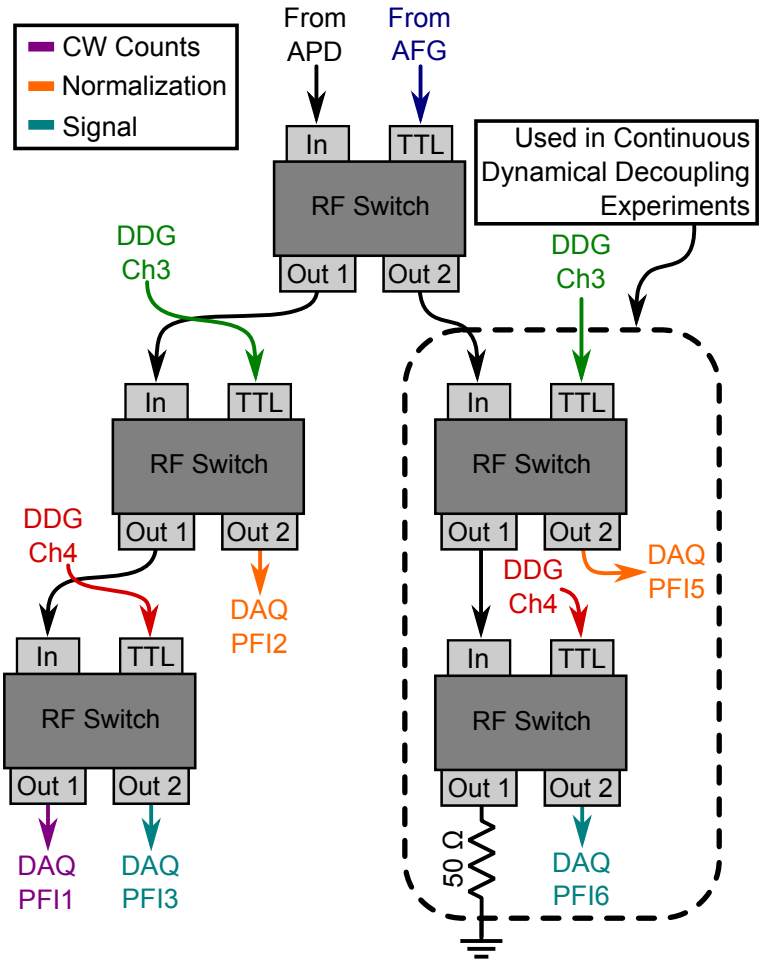

Figure 3.2: The cascade of RF switches used to sort photon counts into the different counters on our DAQ card.

3.2 Microwave Electronics

The microwave electronics used in this thesis varied amongst the experiments to match the carrier frequencies and number of microwave tones necessary for each measurement. A typical setup is depicted schematically in Fig. 3.3. In

this setup, a Tektronix AWG7122B arbitrary waveform generator (AWG) serves as the overall clock for the experiment. The AWG has the ability to output a 24 GS/s waveform directly through an interleaved output or two 12 GS/s waveforms through analog outputs. Similarly sampled digital waveforms can simultaneously be output through the marker channels.

We typically operate the AWG in "Sequence Mode" where all waveforms used in the experiment are loaded into the AWG's memory, and remote commands order jumps between different waveforms within this sequence. When operating in interleave mode, the AWG memory can store 6.48×10^7 points. If the total number of points in all of the waveforms needed for the measurement is less than this, direct output from the AWG can be used to drive the experiment. Alternatively, the AWG output can be used as the I/Q modulation input of a signal generator. In this case, the waveforms used for I/Q modulation can be sampled more sparsely and the AWG memory limits can be satisfied.

The magnetic driving fields in our experiments are generated by either the direct output of the AWG or by I/Q modulating a SRS SG384 signal generator with the analog output of the AWG. The resulting signal is then amplified by a 15 W Ophir 5161FE amplifier. The signal then passes through a directional coupler followed by a circulator and on to the magnetic antenna. The attenuated signal out-coupled at the directional coupler can be redirected to an oscilloscope to monitor the pulse sequences directly.

The mechanical driving fields are generated by I/Q modulating a SRS SG386 signal generator, which has lower phase noise than a signal directly generated by the AWG. This signal is then amplified and passed through a circulator to the HBAR signal pin. The amplifier and circulator used in the measurement are

determined by the frequency of the mechanical resonance under investigation. An RF diode attached to the third port of the circulator measures the power reflected from the HBAR. By monitoring this reflected power as a function of the microwave carrier frequency, we can perform uncalibrated, *in situ* measurements of S_{11} to find the HBAR resonance. The resonance in the admitted power Y_{11} is the optimal operating point for a given resonator mode. To find this point, we compare the separation of the Y_{11} and S_{11} resonances as measured in a separate, calibrated VNA measurement (see Sect. 2.3), and offset the drive frequency by this difference.

In-line attenuators are included in both of these pathways to reduce the overall amplitude of the signal and any reflections.

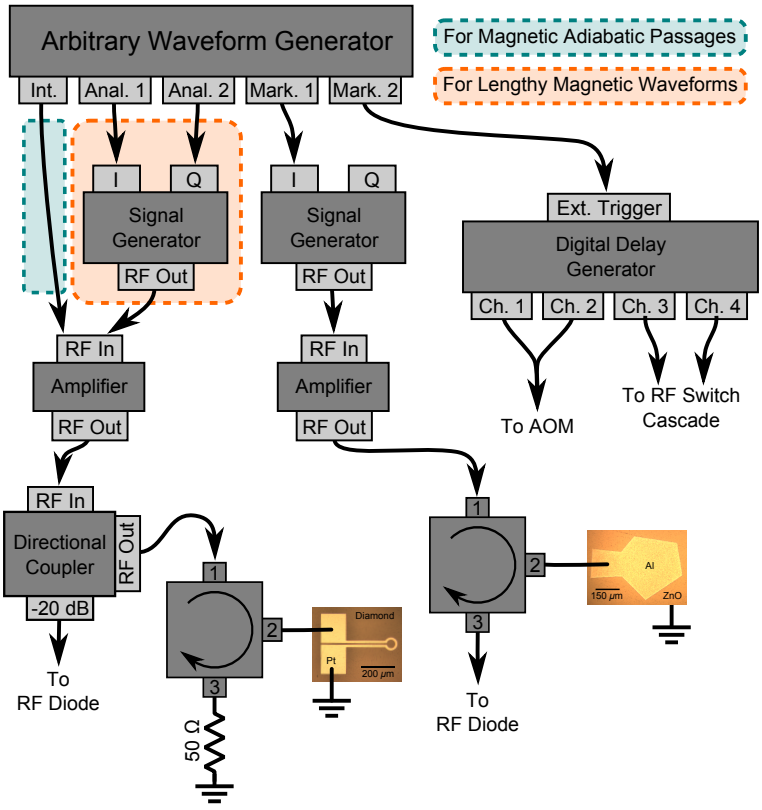

Figure 3.3: A typical setup of the microwave electronics used in our measurements.

CHAPTER 4

MECHANICAL SPIN CONTROL OF NITROGEN-VACANCY CENTERS IN DIAMOND [1]

4.1 Chapter Abstract

We demonstrate direct coupling between phonons and diamond nitrogen-vacancy (NV) center spins by driving spin transitions with mechanically-generated harmonic strain at room temperature. The amplitude of the mechanically driven spin signal varies with the spatial periodicity of the stress standing wave within the diamond substrate, verifying that we drive NV center spins mechanically. These spin-phonon interactions could offer a route to quantum spin control of magnetically forbidden transitions, which would enhance NV-based quantum metrology, grant access to direct transitions between all of the spin-1 quantum states of the NV center, and provide a platform to study spin-phonon interactions at the level of a few interacting spins.

4.2 Main Text

As spin-based quantum technology evolves, the ability to manipulate spin with non-magnetic fields could enable an interface for hybrid quantum systems and facilitate integration with conventional technology. Particularly useful examples are electric fields, optical fields, and mechanical lattice vibrations. The last of these represents direct spin-phonon coupling, which has garnered fundamental interest as a potential mediator of spin-spin interactions [41, 53].

Nitrogen-vacancy (NV) center spins in diamond are a promising solid-state platform for quantum information science [54, 55] and precision metrology. They are sensitive magnetometers [11, 56], electrometers [16], and thermometers [57, 58] with nanoscale spatial resolution due to their atomic size [59, 60]. Significant progress in integrating NV centers with microelectromechanical systems (MEMS) has paved the way for studies of spins coupled to mechanical resonators [20, 61, 37, 38, 62, 42]. In previous work, NV centers have been coupled to phonons indirectly, either by using a magnetic field gradient or by tuning the frequency of a magnetic spin transition. Here, we use a MEMS transducer to directly drive electronic spin transitions in NV centers using gigahertz-frequency mechanical (stress) waves. This work demonstrates direct spin-phonon interactions at room temperature as a means to drive magnetically forbidden spin transitions.

Driving spin transitions is the key to using NV center spins for quantum information science or sensing. Conventionally, quantum spin control in this system is accomplished with gigahertz-frequency magnetic fields [63, 64, 65] or with optical fields at cryogenic temperature [66]. Resonant lattice vibrations couple to nuclear quadrupole moments [67] and represent another avenue to manipulate NV center electronic spins. NV centers couple to a magnetic field ($B_\parallel$ and $B_\perp$) and a stress ($\sigma_\parallel$ and $\sigma_\perp$) through their ground-state spin Hamiltonian [6, 16]:

$$H_{NV} = (D_0 + \epsilon_\parallel \sigma_\parallel) S_z^2 + \gamma_{NV} B_\parallel S_z + \gamma_{NV} B_\perp S_x - \epsilon_\perp \sigma_x (S_x^2 - S_y^2) + \epsilon_\perp \sigma_y (S_x S_y + S_y S_x) \tag{4.1}$$

where $D_0 = 2.87$ GHz is the zero-field splitting, $\gamma_{NV} = 2.8$ MHz/G is the gyromagnetic ratio, $\epsilon_\perp = 0.03$ MHz/MPa [24, 41] and $\epsilon_\parallel$ are the perpendicular and axial stress coupling constants, and S_x, S_y, S_z are the x, y, and z components of

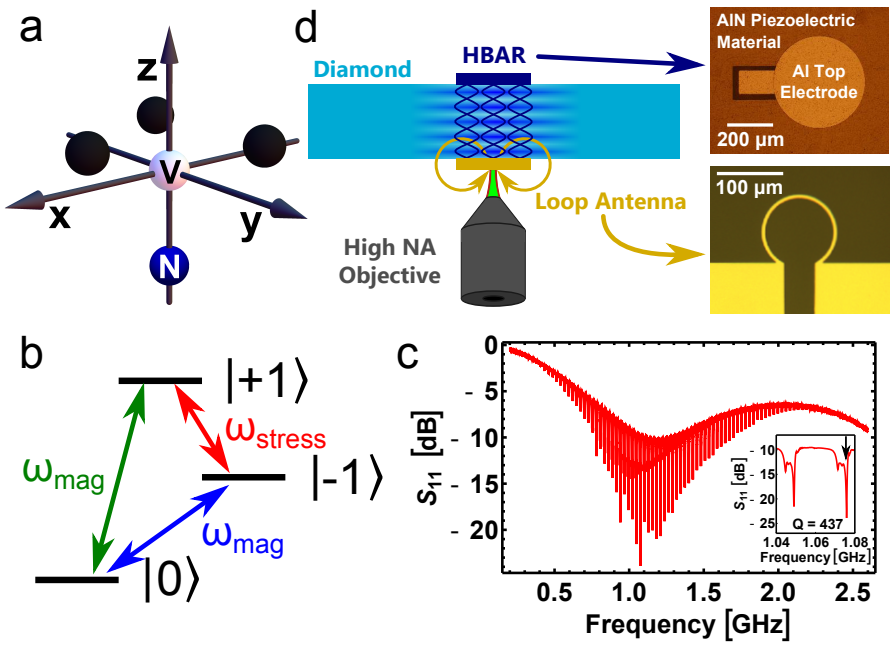

Figure 4.1: (a) Schematic of an NV center. The z-axis corresponds to the symmetry axis of the NV center; (b) Levels of an NV center ground-state spin. Magnetic driving enables $\Delta m_s = \pm 1$ transitions, whereas mechanical driving can produce $\Delta m_s = \pm 2$ transitions. (c) Reflected microwave power (S_{11}) as a function of frequency from the MEMS device measured using a network analyzer. Standing wave resonances have Qs as high as 437; (d) Device schematic. A loop antenna produces gigahertz-frequency magnetic fields for magnetic control while a high-overtone bulk acoustic resonator (HBAR) produces gigahertz-frequency stress standing waves within the diamond.

the spin-1 operator, respectively. The z-axis is defined along the NV symmetry axis as depicted in Figure 4.1a.

In the S_z basis, H_{NV} has eigenstates $\{|(m_s =)0\rangle, |+1\rangle, |-1\rangle\}$. D_0 breaks the degeneracy between the $|0\rangle$ and $|\pm 1\rangle$ spin states at zero magnetic field. Careful alignment of the static external magnetic field $B_\parallel$ along the NV symmetry axis zeros the static component of $B_\perp$ and splits the $|+1\rangle$ and $|-1\rangle$ states. For conventional magnetic spin driving, an oscillating $B_\perp$ can drive spin transitions from the $|0\rangle$ state to either the $|+1\rangle$ or the $|-1\rangle$ state. Similarly, a perpendicu-

lar stress couples the $|+1\rangle$ and $|-1\rangle$ states, allowing a direct $|+1\rangle \leftrightarrow |-1\rangle$ spin transition to be driven by a gigahertz-frequency stress wave resonant with the spin-state splitting. In the S_z eigenbasis, this transition is magnetically forbidden by the magnetic dipole selection rule, $\Delta m_s = \pm 1$. Thus, the ability to drive $|+1\rangle \leftrightarrow |-1\rangle$ with an oscillating stress wave and $|0\rangle \leftrightarrow |\pm 1\rangle$ with oscillating magnetic fields establishes direct transitions between all three spin levels, as depicted in Figure 4.1b. Additionally, an axial stress $\sigma_{\parallel}$ shifts $|+1\rangle$ and $|-1\rangle$ equivalently and therefore has no effect on mechanical spin control performed in the $|\pm 1\rangle$ spin subspace.

The stress coupling coefficient $\epsilon_{\perp}$ is small enough that a large stress is required to produce a driving field comparable to those achieved with magnetic fields. To drive a large stress resonant with gigahertz-frequency spin transitions, we fabricated high-overtone bulk acoustic resonators (HBARs) [68] on one face of a 300 μm thick, $\langle 100 \rangle$ diamond[1]. The type IIa diamond used in these measurements is dense with native NV centers ($\approx 3 \times 10^{14}$ NV/cm^3), placing ≈ 230 NVs inside the confocal volume of our microscope. These NV centers are randomly oriented along one of the four $\langle 111 \rangle$ crystal axes within the diamond. By aligning the static magnetic field $B_{\parallel}$ with one such axis, we isolate a single NV species from the four possible orientations, leaving ≈ 58 NVs that contribute to the signal in our experiments. Those NV centers that are not aligned with $B_{\parallel}$ are not resonant with our control pulses so their fluorescence contributes a constant background to our measurements that is subtracted during data processing.

The HBAR consists of a 3 μm thick aluminum nitride (AlN) piezoelectric film sandwiched between two 400 μm diameter metal electrodes. Applying a gigahertz-frequency voltage across the AlN launches a longitudinal stress wave

[1] See Section 4.3.1

into the diamond. The diamond substrate acts as an acoustic Fabry-Pérot cavity, generating stress standing wave resonances with a pitch determined by the speed of sound in the diamond and the substrate thickness. By measuring the microwave power reflected from the device (S_{11}), we observed the resonant frequency comb of an HBAR (Figure 4.1c). From this data, we used the Q-circle method [45] to find that the unloaded quality factor (Q) of each resonance, which is as high as $Q = 437$ for $\omega_{HBAR} = 2\pi \times 1.076$ GHz. Based on a one-dimensional oscillator model [69], this corresponds to a stress of $\sigma_{max} \approx 10$ MPa directed along the $[001]$ crystal axis of the diamond for 25 dBm of applied microwave power. By transforming the resulting stress tensor from the lattice coordinates to the coordinates of the NV center, we estimate the applied perpendicular stress to be $\sigma_{\perp} \approx 7$ MPa[2]. This is enough for a $\Omega_{stress} \approx 2\pi \times 210$ kHz spin driving field. On the opposite face of the diamond, we fabricated a loop antenna for magnetic spin control (Figure 4.1d).

To demonstrate mechanical spin control, we performed optically detected mechanical spin resonance (ODMSR) measurements of the $|-1\rangle \rightarrow |+1\rangle$ spin transition. The pulse sequences used for this experiment are shown in Figure 4.2a. First, the NV center ensemble is initialized into $|0\rangle$ by optical pumping with a 532 nm laser. The laser is then turned off and a magnetic adiabatic passage through the $|0\rangle \rightarrow |-1\rangle$ resonance robustly transfers the initialized spin population into the $|-1\rangle$ state[3] [70]. The stress wave is then turned on for 6 μs at a frequency ω_{HBAR} corresponding to a resonance of the HBAR. Pulsing the stress wave ensures that any axial stress generated by the HBAR has no effect on the $|0\rangle \leftrightarrow |-1\rangle$ magnetic driving. After this stress pulse, a second magnetic adiabatic passage transfers the population remaining in $|-1\rangle$ to the $|0\rangle$ state.

[2]See Section 4.3.3
[3]See Section 4.3.4

Fluorescence read out of the population in the $|0\rangle$ state is then performed, giving the signal for the experiment. Fluorescence read out is also performed after initialization into the $|0\rangle$ state to provide normalization for each iteration of the duty cycle. By repeating this sequence as a function of $B_{\|}$, we scan $\omega_{\pm 1}$, the energy splitting between $|+1\rangle$ and $|-1\rangle$. Whenever $\omega_{\pm 1} = \omega_{HBAR}$, the strain pulse transfers population from $|-1\rangle$ to $|+1\rangle$. Population transferred to $|+1\rangle$ during the stress pulse shows up as missing population in $|0\rangle$ via fluorescence measurement at the end of the duty cycle.

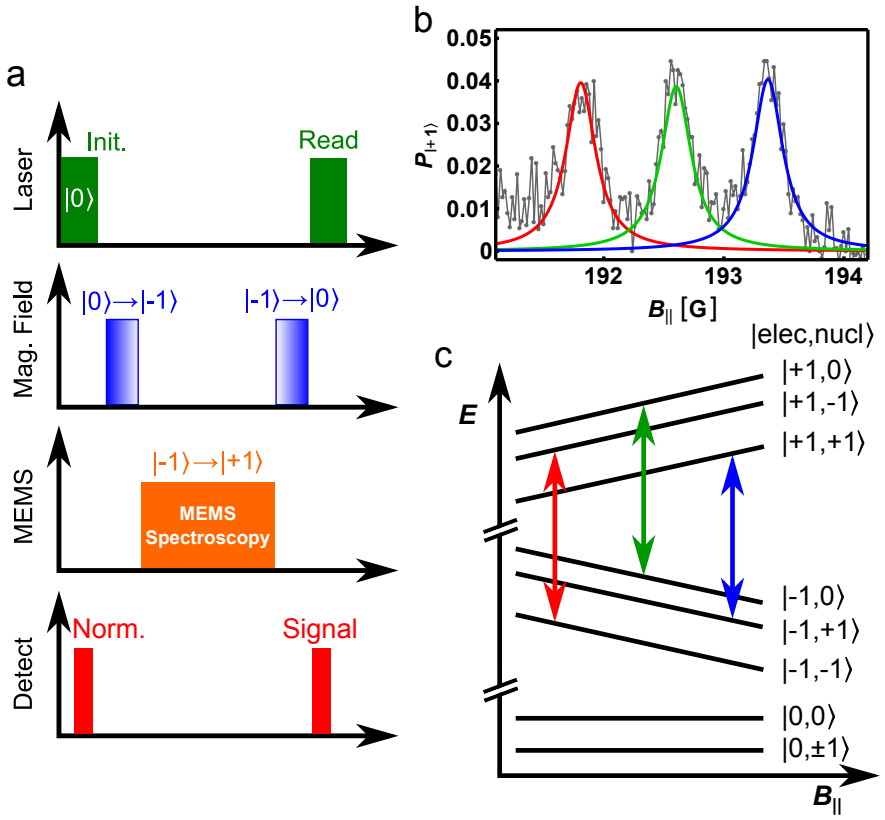

Figure 4.2: (a) Pulse sequence used for ODMSR measurements; (b) Population driven into the $|+1\rangle$ state by the mechanical driving field as a function of the axial magnetic field $B_{\|}$ for $\omega_{HBAR} = 2\pi \times 1.076$ GHz at room temperature; (c) NV hyperfine structure labeled with the experimentally observed transitions. Each arrow corresponds with the resonance condition $\omega_{\pm 1} = \omega_{HBAR}$ for each of the three nuclear spin sublevels.

Typical ODMSR results are shown in Figure 4.2b. The spectrum shows three peaks with 0.78 ± 0.02 G spacing. This corresponds to the $A/\gamma_{NV} = 0.77$ G hyperfine splitting arising from interactions between the NV spins and the unpolarized nuclear spins of the ^{14}N atoms neighboring the vacancies[4] [6]. Because the nuclear spins are not polarized, only one-third of the spins are resonant with each hyperfine sublevel, which reduces the contrast by a factor of three. The contrast is also reduced by inhomogeneous mechanical driving of the NV ensemble. To account for dephasing and inhomogeneous driving, we calibrate the spin contrast by driving with conventional magnetic spin resonance[5]. For the resonance at $\omega_{HBAR} = 2\pi \times 1.076$ GHz, we estimate the peak mechanical driving field is $\Omega_{stress} \approx 2\pi \times 230$ kHz. This is consistent with the coupling strength of 0.03 MHz/MPa, which was previously determined from measurements of static strain at low temperature [24, 41]. For scale, a single NV with a polarized nuclear spin driven at a stress antinode of this resonance would show 14% spin contrast. We also verified with measurements taken at an HBAR resonance with a different mechanical Q that the spin contrast scales with the Q, as expected[6].

Because stress and electric fields enter the NV spin Hamiltonian in the same way [6], we verified that the ODMSR signals do not result from stray electric fields. To address this possibility, we used the finite element analysis software ANSYS HFSS to simulate the electric field generated during the stress pulse, which comprises the dominant source of stray electric field in the experiment. The loop antenna on the rear face of the diamond was included. The simulated electric field within the relevant region of the diamond was no larger than $E_{sim} = 10$ V/cm. The coupling strength between a perpendicular electric field

[4] See Section 4.3.5
[5] See Section 4.3.6
[6] See Section 4.3.7

and the NV ground state spin is $d_{gs}^{\perp} = 17 \pm 3$ Hz cm/V [71, 16]. Under conservative assumptions, E_{sim} would generate a driving field roughly four orders of magnitude lower than observed in the experiment. We also considered, but ruled out, magnetic driving of the $|+1\rangle \leftrightarrow |-1\rangle$ transition via stray magnetic fields from the MEMS transducer[7].

As a critical verification that we drive spin transitions with mechanically-generated stress waves, we investigated how the ODMSR signal varies as a function of depth. Because we drive a stress standing wave, we expect that the ODMSR signal will be modulated at the periodicity of the standing wave. Taking care to account for optical aberrations introduced from refraction at the air-diamond interface [72], we repeated ODMSR measurements of the $\omega_{HBAR} = 2\pi \times 0.942$ GHz mechanical resonance at different depths within the sample. To correctly interpret the results, we note that our microscope collects fluorescence from all of the NV centers within its confocal volume. Figure 4.3a depicts schematically the variation in stress amplitude across an approximate confocal point spread function (PSF). Different regions within the confocal volume experience different stress driving fields, and we sample the range of stresses within the PSF. This reduces the spatial resolution in the focal direction and contributes to the inhomogeneous spin dephasing of the NV centers.

The ODMSR signal depends on the overlap between the oscillating stress and the PSF of the microscope, which is a maximum at an anti-node of the stress standing wave. In contrast, ODMSR measured at a node is reduced by a factor of 1.5 (Figure 4.3b). Our approximate model, which is not a fit to the data, reproduces this ratio and the structure of the measured oscillation. To calculate the model curve, we convolve the stress standing wave with an approximated PSF

[7] See Section 4.3.9

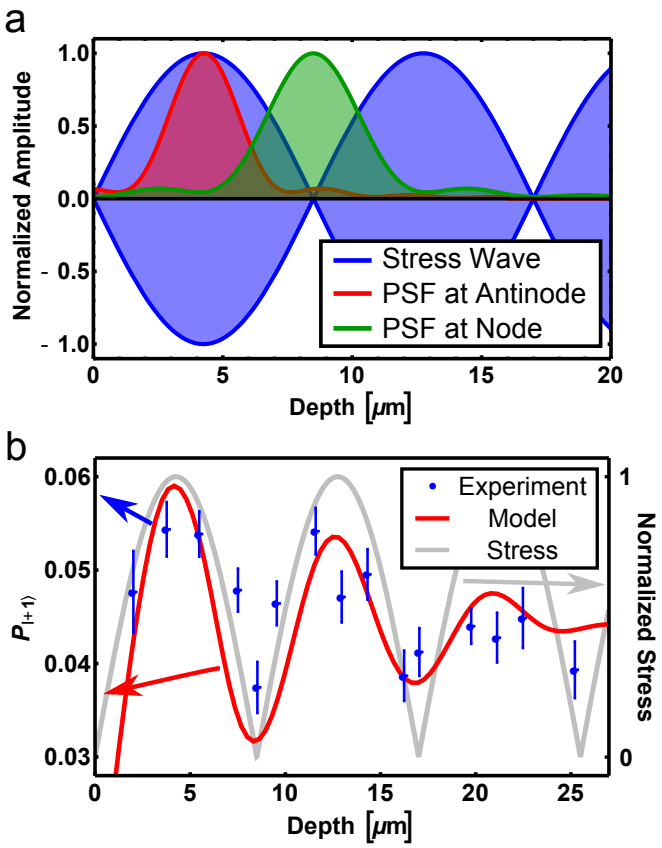

Figure 4.3: (a) Normalized point spread function (PSF) of our confocal microscope plotted at a node and an anti-node of the stress standing wave; (b) Peak ODMSR signal as a function of depth inside the diamond. The oscillations as a function of focal depth correspond to oscillations in stress along the standing wave used to drive spin transitions.

that accounts for distortions in the position and shape of the PSF as a function of focal depth inside the diamond[8]. Crucially, we find excellent agreement between the spatial periodicity of the measured signal and the 17 μm wavelength of the HBAR-generated standing wave. This wavelength was calculated from the speed of sound in diamond (16 km/s) that we determined from the HBAR resonance pitch and the sample thickness. The decay of the measured oscillation at large depths is due to refractive aberration of the optical PSF, which

[8]See Section 4.3.10

increases linearly as a function of depth. Taken together, these observations are the 'smoking gun' for mechanically driven spin transitions because the stress standing wave is the only element of the experiment with spatial periodicity.

The modest ODMSR amplitudes of these measurements are limited by the amplitude of the stress wave, the power handling capabilities, and the driving field inhomogeneities in this first generation of devices. Because of these device limitations, we observe only incoherent driving of NV center spins. Improvements in device fabrication are estimated to increase the HBAR Qs by greater than a factor of five at room temperature [73], and cooling the samples to cryogenic temperature can increase the Q by a factor of $\approx 10^3$ [74]. Driving field inhomogeneities can be dispelled by driving either a single NV or a lateral plane of NVs, either of which would select a single value of the stress wave amplitude. Upon instituting these modest engineering improvements, we expect that coherent driving of the NV spin state is possible, putting stress driving fields on equal footing with magnetic driving.

Such control has a number of practical sensing applications. Fang *et al.* demonstrated that using a $|\pm 1\rangle$ qubit for NV magnetometry enhances sensitivity and provides isolation from temperature fluctuations [56]. Because they directly couple the relevant states, mechanical driving pulses could be useful for dynamical inversion of the $|\pm 1\rangle$ qubit, providing an alternative to $|\pm 1\rangle$ inversions constructed from a series of magnetic pulses that use $|0\rangle$ as a waypoint. Additionally, the spin signal from mechanically driven NV centers could be used as a precision sensor for gigahertz frequency strains. One practical use may be to integrate NV centers with a MEMS accelerometer where acceleration shifts the intensity of AC strain. This would combine the high sensitivity of

MEMS inertial sensing with the long-term stability of a spin transition, in a similar spirit to proposals for NV-based gyroscopes [75, 76]. At low temperatures, it has been predicted that NV centers interacting with the cavity phonons of a mechanical resonator can generate a spin-squeezed state [41], and conversely, driven NV centers can be used to coherently cool or drive cavity phonons [42]. The mechanical spin driving presented here is the first step towards achieving these goals.

The development of new technology based on quantum spins in the solid-state will depend on integration with both existing technology and other qubit systems. We have demonstrated spin manipulation through a direct interaction between spins and resonantly-driven cavity phonons, thus providing a new tool for integration and a new avenue for fundamental studies of spin-phonon interactions.

4.3 Supplementary Information

4.3.1 Experimental Details

Measurements were performed using a home-built confocal microscope (Fig. 4.4a). An Oxxius SLIM-532 150 mW laser was focused through a Gooch & Housego 15210 acousto-optic modulator (AOM) that was used as a high-speed shutter. An Optics in Motion 101 fast-scanning mirror was used to control the lateral position of the confocal focus. Both excitation and NV center emission were focused through an Olympus LMPLFLN, 100x objective. The emission was detected with an Excelitas SPCM-AQRH-FC avalanche photodiode.

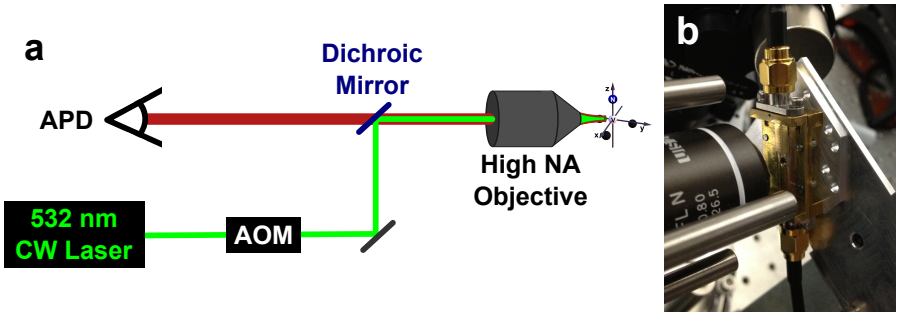

Figure 4.4: (a) Home-built confocal microscope; (b) Diamond sample mounted in the microscope with custom-built brass sample box. The front side of the diamond (facing the microscope objective) has a lithographically-patterned microwave antenna wire bonded to a coplanar waveguide within the brass sample box. The back side contains the AlN transducer, which is wire-bonded to a second coplanar waveguide built into the brass sample box. Visible behind the brass sample box is the permanent magnet, which provides the static magnetic field in the experiment.

Samples were mounted in the custom-built brass sample box pictured in Fig. 4.4b. The high-overtone bulk acoustic resonator (HBAR) device was powered by a Stanford Research Systems SG384 signal generator amplified by a Minicircuits ZRL-1150LN amplifier. The loop antenna was powered by a Tektronix 7122B Arbitrary Wave Generator (AWG) amplified by an Ophir 5161FE amplifier. A Stanford Research Systems DG645 digital delay generator triggered by the AWG was used to synchronize the various instruments and pulse the AOM. The axial magnetic field $B_{\|}$ was produced by a NdFeB permanent magnet on a motorized translation stage to enable field scanning.

The diamond substrate is an 'optical-grade,' 300μm thick, single-crystal diamond purchased from Element Six. The sample was first cleaned in a boiling nitric:sulfuric (3:2) acid solution for one hour. Ti/Pt ($25/225$ nm) electrodes were then patterned on one face to serve as the ground plane for the HBARs. AlN was sputtered to a thickness of 3 μm, and an Al layer was patterned on top to

serve as the HBAR signal electrode. The HBAR was then coated in photoresist for protection while Ti/Pt ($25/225$ nm) loop antennas were patterned on the opposite face.

4.3.2 Magnetic Spin Coherence

The transverse magnetic spin coherence times were measured to be $T_2^* = 1.7 \pm 0.2$ μs and $T_2 = 100 \pm 30$ μs in the $|0\rangle \leftrightarrow |-1\rangle$ spin subspace using a Ramsey and Hahn echo sequence, respectively. The second $\pi/2$ pulse in our Ramsey sequence was phase delayed relative to the first $\pi/2$ pulse by $\phi = \Omega_{rot}(T_{\pi/2} + \tau)$ where $T_{\pi/2}$ is the length of a $\pi/2$ pulse. This detunes our measurement from the spin's rotating frame by Ω_{rot} and allows us to observe spin precession in the form of signal beating. All pulses in the Hahn echo measurement were phase continuous.

Pulse sequences and data for these measurements are presented in Fig. 4.5. Inhomogeneities in the magnetic field reduce T_2^* in our sample—a typical signature of NV ensembles. The small discrepancies between the Ramsey data and our model are likely due to pulse errors or, more specifically, overlapping pulse tails, which create rotation and phase errors for short values of the inter-pulse delay τ. As demonstrated by Stanwix, *et al*, misalignment of our static magnetic field $B_{\|}$ may have reduced our measured T_2 from its optimum value [77].

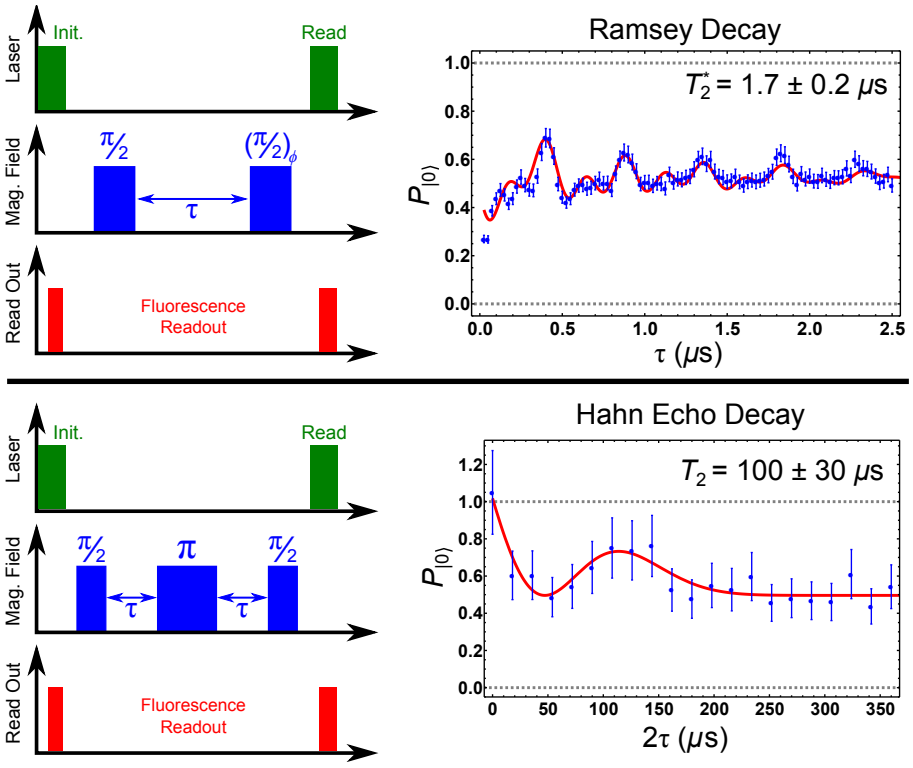

Figure 4.5: Ramsey and Hahn echo measurements used to determine the magnetic spin coherence times of our NV center ensemble. Error bars are calculated from photon shot noise.

4.3.3 Treatment of the Stress Projection

In our mechanical spin driving experiments, we apply a ≈ 10 MPa stress along the $[001]$ direction of the diamond lattice. This is described by the stress tensor in the lattice coordinate system

$$\mathbf{T} \approx \begin{pmatrix} 0 & 0 & 0 \\ 0 & 0 & 0 \\ 0 & 0 & 10 \end{pmatrix} \text{MPa} \tag{4.2}$$

We then transform $\mathbf{T}$ into the NV coordinate system defined such that the x', y', and z'-axes run along the $[\bar{1}\bar{1}2]$, $[1\bar{1}0]$, and$[111]$ lattice directions, respectively

(Fig. 4.6). This gives the stress tensor in the NV coordinates as

$$\mathbf{T}' \approx \begin{pmatrix} 7 & 0 & 5 \\ 0 & 0 & 0 \\ 5 & 0 & 3 \end{pmatrix} \text{MPa} \tag{4.3}$$

which corresponds to a ≈ 5 MPa shear stress and a ≈ 7 MPa normal stress along the x'-direction.

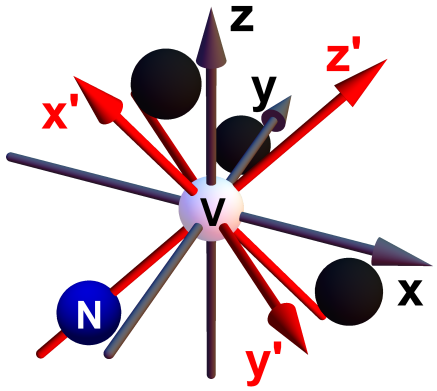

Figure 4.6: Lattice coordinates (grey) and NV coordinates (red) used in the stress tensor analysis.

Although our experiment is performed in terms of stress, the NV center spin Hamiltonian is usually formulated to address strain [6]. Using the compliance matrix for diamond [78, 79], we convert $\mathbf{T}$ into a strain tensor $\mathbf{E}$ in the lattice coordinates:

$$\mathbf{E} \approx \begin{pmatrix} -5 & 0 & 0 \\ 0 & -5 & 0 \\ 0 & 0 & 90 \end{pmatrix} \times 10^{-7} \tag{4.4}$$

Transforming $\mathbf{E}$ into the NV coordinates, we find

$$\mathbf{E}' \approx \begin{pmatrix} 60 & 0 & 40 \\ 0 & -5 & 0 \\ 40 & 0 & 30 \end{pmatrix} \times 10^{-7} \tag{4.5}$$

which contains both shear strains and normal strains. As the torsional components of strain are usually neglected in derivations of the NV spin Hamiltonian [6], we neglect them here in both our strain and stress tensors, giving us $\sigma_\perp \approx 7$ MPa for the component of the stress perpendicular to the NV symmetry axis.

4.3.4 Adiabatic Passage Parameters

We used a linearly ramped adiabatic passage with $\Delta\omega = 100$ MHz detuning throughout our experiments. Because the amplitude of our magnetic driving field decreases at larger depths inside the diamond, the sweep rate of the adiabatic passage was optimized as a function of depth within the diamond to maintain fidelity. For measurements near the diamond surface, the adiabatic passage sweep rate was typically 31 MHz/μs. At the largest depths measured here (25 μm below the surface), the passage was 11.6 MHz/μs.

4.3.5 Hyperfine Level Ordering

The energy shifts resulting from hyperfine coupling with the ^{14}N nuclear spin are given by the expression

$$H_I = PI_z^2 + A_\parallel I_z S_z \tag{4.6}$$

where we use the hyperfine parameters $A_\parallel = -2.166$ MHz and $P = -4.945$ MHz [6, 80, 81]. Applying these energy shifts to the S_z eigenstates, we obtain the energy levels depicted in Fig. 4.7, which match the ordering shown in Fig. 4.2c of Sect. 4.2.

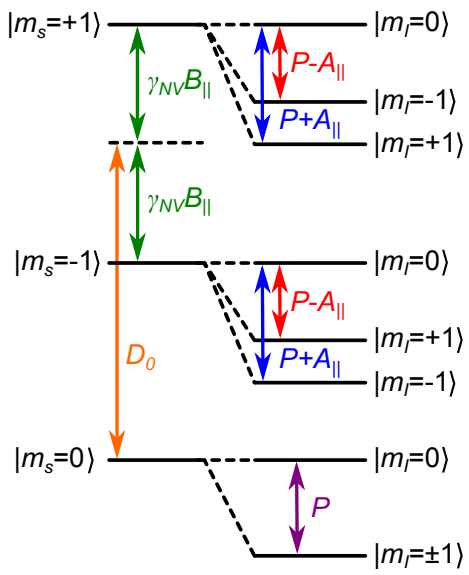

Figure 4.7: Shifts to the electronic spin structure due to hyperfine coupling with the ^{14}N nuclear spin.

4.3.6 Driving Field Calibration

We used conventional pulsed magnetic resonance signals to estimate the stress driving fields associated with the ODMSR signal. For calibration we modified the pulse sequence shown in Fig. 4.2a of Sect. 4.2 by replacing the stress pulse with a magnetic field pulse resonant with the $|-1\rangle \rightarrow |0\rangle$ spin transition. The population that was driven into the $|0\rangle$ state by this pulse was returned to the $|-1\rangle$ state during the second adiabatic passage, allowing us to observe magnetic spin driving as an absence of population in the $|0\rangle$ state.

We tuned the strength of the magnetic field pulse until the amplitude of the magnetic resonance signal matched that of our ODMSR signals. At this point, the driving fields generated by the stress pulse and the magnetic field pulse are equal, giving us a point of comparison. Because the magnetic driving field scales as $\sqrt{P}$ where P is the microwave power coupled into the loop antenna,

we measured the magnetic driving field directly at a higher value of P by observing Rabi oscillations, and extrapolated downward to find the driving field generated by the weaker magnetic pulse.

To estimate the total driving amplitude of the ODMSR signals, we first subtract a constant background from the ODMSR signal that we attribute to pulse errors. By convolving the microscope PSF and the stress standing wave, we estimate that inhomogeneities in the stress driving field reduce the measured stress value to $0.84\sigma_{max}$ for the $\omega_{HBAR} = 2\pi \times 1.076$ GHz resonance at the anti-node closest to the diamond surface. Dividing the sum of the hyperfine peak amplitudes displayed in Fig. 4.2b of Sect. 4.2 by this 0.84 correction factor gives the ideal peak ODMSR signal that we compare with our magnetic resonance data to determine a peak stress driving field of $\approx 2\pi \times 230$ kHz.

Using the approximate model described below, we determine the inhomogeneous mechanical driving of the NV ensemble reduces the observed ODMSR contrast by a factor of 1.2. Accounting for these effects, we estimate a 14% spin contrast for a single NV center with a polarized nuclear spin driven by an antinode of the $\omega_{HBAR} = 2\pi \times 1.076$ GHz resonance.

4.3.7 Measurements at Different Q Values

Measurements were taken at two different stress resonances ($\omega_1 = 2\pi \times 1.076$ GHz and $\omega_2 = 2\pi \times 1.103$ GHz) which had Q's of 437 and 350 respectively. Since we are not driving the $|-1\rangle \rightarrow |+1\rangle$ spin transition to saturation, the stress driving field is expected to depend linearly on the Q of the resonance. To compare the driving field generated at different HBAR resonances, we take

into account both the Q and the impedance of the HBAR for each resonance. The ratio of driving fields should match the ratio of stress, which may be calculated as

$$r_{stress} = \frac{Q_1}{Q_2} \times \frac{V_1}{V_2} = \frac{Q_1}{Q_2} \times \frac{Z_1\sqrt{50\ \Omega + Z_2}}{Z_2\sqrt{50\ \Omega + Z_1}} \tag{4.7}$$

where $Z_1 = 29.9\ \Omega$ is the microwave impedance of the HBAR at resonance 1 and $Z_2 = 33.5\ \Omega$ is the microwave impedance of the HBAR at resonance 2. Using the two resonances mentioned above, we measure the ratio of driving fields to be 1.10 ± 0.05, which is close to the expected value of $r_{stress} = 1.14$, which we calculate from equation S4.7 and network analyzer measurements.

4.3.8 Rabi Driving with Strain

In order to determine the optimal pulse length for the stress wave in our measurements, we performed a Rabi-style ODMSR measurement where the length of the stress pulse τ was varied from 0 to a maximum value T. The pulse sequence for this experiment is depicted in Fig. 4.8a. To mitigate thermal effects, the total power to the sample was kept constant by applying a buffer stress pulse of length $(T - \tau)$ after the second magnetic adiabatic passage (AP) has driven the $|-1\rangle$ population back into the $|0\rangle$ spin state. Because there is no magnetic pulse following this second stress pulse, population driven between $|+1\rangle$ to $|-1\rangle$ during the second pulse has no effect on fluorescence measurement, which is sensitive only to the population of $|0\rangle$.

The experimental signal, shown in Fig. 4.8b, decays exponentially in τ. The characteristic decay time is $T_{Rabi} = 1.03 \pm 0.12\ \mu$s, which we attribute to dephasing of the spin ensemble by inhomogeneous stress within the collection volume.

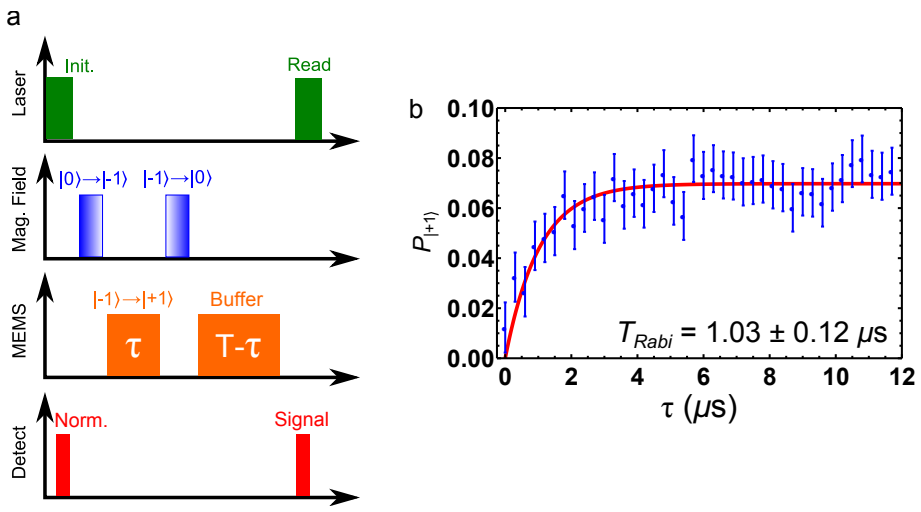

Figure 4.8: (a) Pulse sequence for Rabi-style ODMSR measurement. The first MEMS pulse is for state transition, whereas the second pulse keeps the total MEMS power fixed throughout the duty cycle. The second pulse does not disturb the population of $|0\rangle$, which is proportional to the fluorescence contrast in spin measurement. (b) Results from Rabi-style ODMSR measurement. No coherent oscillations are observed because we measure fluorescence from inhomogeneous stresses within the confocal volume of our microscope.

From this measurement, we selected the 6 μs pulse length that was used for all of the ODMSR measurements reported in the main text.

4.3.9 The Effect of Stray Magnetic Fields from the HBAR

We examined the effect of stray *magnetic* fields produced by the HBAR and resonant with the $|-1\rangle \leftrightarrow |+1\rangle$ transition, as a potential spurious contribution to the ODMSR signal. To understand this effect, we consider the Hamiltonian for an NV center in a static magnetic field that is aligned with the NV symmetry axis

$$H_0 = D_0 S_z^2 + \gamma_{NV} B_{\parallel} S_z, \tag{4.8}$$

with the perturbation

$$\Delta H = \gamma_{NV} B_{x0} S_x, \tag{4.9}$$

which represents a small ($B_{x0} \ll B_{\|}$) perpendicular component to the static magnetic field, aligned along the x-axis for simplicity.

To first order, ΔH mixes the eigenstates of H_0 without shifting their energy. Rewriting S_x in the basis defined by the first-order perturbed eigenstates, we find

$$S_x' = \begin{pmatrix} \frac{\gamma_{NV} B_{x0}}{\omega_{+1}} & \frac{1}{\sqrt{2}} & \frac{\gamma_{NV} B_{x0}}{2}\left(\frac{1}{\omega_{+1}} + \frac{1}{\omega_{-1}}\right) \\ \frac{1}{\sqrt{2}} & -\gamma_{NV} B_{x0}\left(\frac{1}{\omega_{+1}} + \frac{1}{\omega_{-1}}\right) & \frac{1}{\sqrt{2}} \\ \frac{\gamma_{NV} B_{x0}}{2}\left(\frac{1}{\omega_{+1}} + \frac{1}{\omega_{-1}}\right) & \frac{1}{\sqrt{2}} & \frac{\gamma_{NV} B_{x0}}{\omega_{-1}} \end{pmatrix}, \tag{4.10}$$

where we use ω_{+1} for the unperturbed $|0\rangle \rightarrow |+1\rangle$ transition energy and ω_{-1} for the unperturbed $|0\rangle \rightarrow |-1\rangle$ transition energy. This can be re-written as

$$S_x' = S_x + \frac{\gamma_{NV} B_{x0}}{2}\left(\frac{1}{\omega_{+1}} + \frac{1}{\omega_{-1}}\right)(S_x^2 - S_y^2) + \text{diagonal terms}. \tag{4.11}$$

The second term in S4.11 introduces transverse anisotropy with the same form as perpendicular stress. Therefore, application of a resonant oscillating field, $B_{x1}(t) = B_{x1}\cos[(\omega_{+1} - \omega_{-1})t]$ weakly drives spin transitions in a misaligned static magnetic field. Under the rotating wave approximation, the $|-1\rangle \leftrightarrow |+1\rangle$ driving field will be

$$\Omega_{|-1\rangle \rightarrow |+1\rangle} = \frac{\gamma_{NV}^2 B_{x1} B_{x0}}{4}\left(\frac{1}{\omega_{+1}} + \frac{1}{\omega_{-1}}\right) = \frac{\gamma_{NV}^2 B_{x1} B_{x0} D_0}{2(D_0^2 - \gamma_{NV}^2 B_{\|}^2)}. \tag{4.12}$$

Comparing this with the conventional expression for magnetically driving the $|0\rangle \rightarrow |\pm 1\rangle$ transition on resonance ($\Omega_{|0\rangle \rightarrow |\pm 1\rangle} = \gamma_{NV} B_{x1}/\sqrt{2}$), we find the following expression for the ratio of driving fields:

$$\frac{\Omega_{|-1\rangle \rightarrow |+1\rangle}}{\Omega_{|0\rangle \rightarrow |\pm 1\rangle}} = \frac{\sqrt{2}\gamma_{NV} B_{x0} D_0}{D_0^2 - \gamma_{NV}^2 B_{\|}^2}. \tag{4.13}$$

At $B_{\|} = 192$ G, this results in a driving field of $\Omega_{|-1\rangle\rightarrow|+1\rangle} \cong 0.0014 \times B_{x0} \times \Omega_{|0\rangle\rightarrow|\pm1\rangle}$, where B_{x0} has units of G.

As an experimental test of this effect, we replaced the stress wave pulse in our ODMSR experiments with a magnetic field pulse through the microwave antenna, resonant with the $|-1\rangle \rightarrow |+1\rangle$ transition, and with a power equivalent to $\Omega_{|0\rangle\rightarrow|\pm1\rangle} = 2\pi \times 820$kHz for conventional magnetic driving. Because we measured in a slightly misaligned magnetic field ($B_{x0} \neq 0$), we observed weak magnetic driving of the $|-1\rangle \rightarrow |+1\rangle$ transition. (Fig. 4.9b).

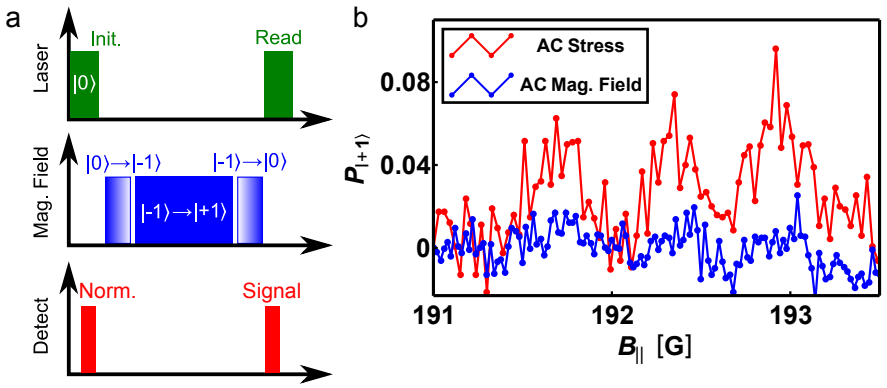

Figure 4.9: (a) Pulse sequence for measuring B_{x1} field driving the $|-1\rangle \rightarrow |+1\rangle$ transition; (b) Magnetic driving of the $|-1\rangle \rightarrow |+1\rangle$ transition using $\Omega_{|0\rangle\rightarrow|\pm1\rangle} \approx 2\pi \times 820$kHz (blue) plotted next to stress driving (red). Both are measured on the $\omega_{HBAR} = 2\pi \times 1.076$ GHz acoustic resonance.

Using the electromagnetic simulation mentioned in the main text, we calculate that the stray magnetic field produced by the HBAR is $B_{1,HBAR} = 0.17$ G at the depth of optical measurements, and directed perpendicular to the plane. Under the most conservative estimate, we assume that $B_{x0} = 10$ G. Using equation S4.13, we estimate the stray magnetic field produces $\Omega_{|-1\rangle\rightarrow|+1\rangle} \cong 2\pi \times 2.7$ kHz, about $100\times$ smaller than the stress-wave induced driving field. Moreover, this magnetic field is about $4\times$ smaller than the field we applied

in our experimental test, where we intentionally introduced a magnetic driving field through the microwave antenna. Interestingly, although we have just shown it is possible to drive the $|-1\rangle \leftrightarrow |+1\rangle$ spin transition magnetically, in most cases it is not practical. It requires very large values of B_{x1} unless B_{x0} is sizable. Unfortunately, as B_{x0} grows, the eigenstates of the S_z basis mix more strongly, reducing both NV read-out contrast and spin coherence [77].

Magnetic driving of the $|-1\rangle \leftrightarrow |+1\rangle$ spin transition is fundamentally limited by weak coupling in the S_z basis, but mechanical driving is not, where the primary limitation is the stress wave amplitude. Mechanical driving affects neither spin coherence nor read-out contrast. With room temperature HBAR Q's expected to improve by more than a factor of five in the next generation of devices, mechanical driving is the more practical for route quantum control using the $|-1\rangle \leftrightarrow |+1\rangle$ spin transition.

4.3.10 Corrections to the PSF

To accurately interpret our measurement of the stress standing wave (Fig. 4.3b of Sect. 4.2), it is critical to know the shape and location of our microscope's point spread function (PSF) inside the diamond. This problem is nontrivial because refraction at the air-diamond interface introduces aberrations that shift the focus deeper into the diamond and distort the PSF wavefront (Fig. 4.10). Geometric optics relates the depth of the PSF inside the diamond d_{dia} to the nominal depth d_{air} as

$$d_{dia} = \frac{n_{dia} \cos\theta_{dia}}{n_{air} \cos\theta_{air}} d_{air} \tag{4.14}$$

where n is the index of refraction.

Assuming isotropic NV emission with intensity I_0, the power $P(\theta_{dia})$ that leaves the back of the objective is given by

$$P = \pi I_0 d_{dia}^2 \tan^2 \theta_{dia} T(\theta_{dia}) \tag{4.15}$$

where $T(\theta_{dia})$ is the Fresnel transmission coefficient for unpolarized emission:

$$T(\theta_{dia}) = \frac{2n_{dia}n_{air}\cos\theta_{air}\cos\theta_{dia}}{(n_{dia}\cos\theta_{air} + n_{air}\cos\theta_{dia})^2} + \frac{2n_{dia}n_{air}\cos\theta_{air}\cos\theta_{dia}}{(n_{air}\cos\theta_{air} + n_{dia}\cos\theta_{dia})^2}. \tag{4.16}$$

We use Eq. 4.14 and Snell's Law to express d_{dia} and θ_{air} as functions of θ_{dia}. Differentiating $P(\theta_{dia})$, we arrive at an expression for the differential power $\mathrm{d}P/\mathrm{d}\theta_{dia}$ that we use as a weight to determine the average value of d_{dia} as a function of d_{air}:

$$\langle d_{dia} \rangle = d_{air} \frac{\int_0^{\theta_{dia}^{max}} \frac{n_{dia}\cos\theta_{dia}}{n_{air}\cos\theta_{air}} \frac{\mathrm{d}P}{\mathrm{d}\theta_{dia}} \mathrm{d}\theta_{dia}}{\int_0^{\theta_{dia}^{max}} \frac{\mathrm{d}P}{\mathrm{d}\theta_{dia}} \mathrm{d}\theta_{dia}} \approx 3.2 d_{air} \tag{4.17}$$

where θ_{dia}^{max} is defined by the expression $\sin\theta_{dia}^{max} = \frac{\mathrm{NA}}{n_{dia}}$ and $\mathrm{NA} = 0.8$.

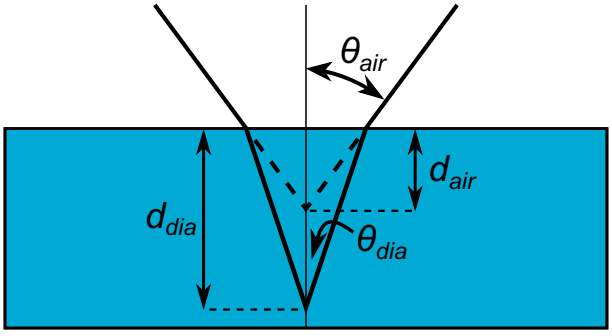

Figure 4.10: (a) Geometry used to estimate the aberration introduced by refraction at the air-diamond interface.

This correction factor of 3.2 describes how the focal position shifts inside the diamond and serves as a lower bound to the true correction since we do not account for other aberrations in our microscope. For the wavelength of our measured standing wave to match the expected value of 17 μm, the correction

factor needs to be 3.4 ± 0.1. We attribute the small mismatch in the wavelength to other aberrations, not accounted for in this calculation. The calculated 3.2 correction factor was used at all times in the main text.

In order to account for distortions to the shape of the PSF, we approximate the change in the PSF FWHM by the expression

$$FWHM_{dia} = \frac{1}{2}\left(\frac{n_{dia}\cos\theta_{dia}^{max}}{n_{air}\cos\theta_{air}^{max}} - \frac{n_{dia}\cos\theta_{dia}^{min}}{n_{air}\cos\theta_{air}^{min}}\right) d_{air} + FWHM_0 \tag{4.18}$$

where θ^{max} is set by the microscope NA and $\theta^{min} = 0$.

Measurements of single NV centers at shallow depths place $FWHM_0 \approx 2\ \mu$m near the diamond surface. Using this as a starting point, we calculate the PSF near the surface using Fermat's principle which remains valid for high NA objectives [72]. We then propagate the PSF into the diamond using the approximate linear corrections to the PSF peak position and FWHM described above. By normalizing the resulting PSF, convolving it with a standing wave, and normalizing the result to the integrated area of the PSF, we produce the theoretical curve shown in Fig. 4.3b of Sect. 4.2. It is important to note that this is an approximation because it is not calculated using full diffraction theory and does not include non-refractive aberrations. Therefore, some differences between the model and the experiment are expected.

4.4 Acknowledgments

Research support for Chapter 4 was supported by the Cornell Center for Materials Research with funding from the NSF MRSEC program (DMR-1120296) and the Department of Energy Office of Science Graduate Fellowship Program

(DOE SCGF), made possible in part by the American Recovery and Reinvestment Act of 2009, administered by ORISE-ORAU under contract no. DE-AC05-06OR23100. Device fabrication was performed in part at the Cornell NanoScale Science and Technology Facility, a member of the National Nanotechnology Infrastructure Network, which is supported by the National Science Foundation (Grant ECCS-0335765).

CHAPTER 5

COHERENT CONTROL OF A NITROGEN-VACANCY CENTER SPIN ENSEMBLE WITH A DIAMOND MECHANICAL RESONATOR [2]

5.1 Chapter Abstract

Coherent control of the nitrogen-vacancy (NV) center in diamond's triplet spin state has traditionally been accomplished with resonant ac magnetic fields. Here, we show that high-frequency stress resonant with the spin state splitting can also coherently control NV center spins. Because this mechanical drive is parity non-conserving, controlling spins with stress enables direct access to the magnetically forbidden $|-1\rangle \leftrightarrow |+1\rangle$ spin transition. Using a bulk-mode mechanical microresonator fabricated from single-crystal diamond, we apply intense ac stress to the diamond substrate and observe mechanically driven Rabi oscillations between the $|-1\rangle$ and $|+1\rangle$ states of an NV center spin ensemble. Additionally, we measure the inhomogeneous spin dephasing time (T_2^*) of the spin ensemble within this $\{-1, +1\}$ subspace using a mechanical Ramsey sequence and compare it to the dephasing times measured with a magnetic Ramsey sequence for each of the three spin qubit combinations available within the NV center ground state. These results demonstrate coherent control of a spin with a mechanical resonator and could lead to the creation of a phase-sensitive Δ-system inside the NV center ground state with potential applications in quantum optomechanics and metrology.

5.2 Main Text

5.2.1 Introduction

Spin-based quantum systems typically rely on resonant magnetic fields to drive coherent transitions between different spin states. Although such magnetic driving has been effective, developing alternative modes of control opens new routes for coupling disparate quantum states to form a hybrid quantum system [82]. New techniques for manipulating a spin state also naturally extend to new sensing capabilities and an enhanced understanding of how spin systems interact with their environment.

The spin triplet ground state of the nitrogen-vacancy (NV) center in diamond represents a coherently addressable paramagnetic defect confined within a largely non-magnetic carbon lattice. This creates an excellent laboratory for studying how spin-based quantum systems interact with their environment [83] and for exploring new methods of quantum control [63]. Studies have shown that NV center spins can be controlled magnetically [64], optically [84, 28], electrically [16], and mechanically [1, 31, 32]. The direct spin-phonon coupling that enables mechanical spin control mediated by lattice strain has prompted the experimental development of single-crystal diamond mechanical resonators [85, 1, 31, 32] and motivated theoretical calculations showing that this interaction could enable spin squeezing [41] and mechanical resonator cooling [42]. Nonetheless, coherent Rabi driving of NV center spins with a mechanical resonator has not been previously demonstrated. Furthermore, understanding the dynamics of mechanical driving in spin ensembles could have applications in NV center-based sensing and quantum optomechan-

ics where spin-phonon interactions can be enhanced by using a large number of spins.

Here we use a mechanical microresonator to apply a large amplitude ac stress to a single crystal diamond. Building on recent spectroscopy experiments[1] [1], we tune the frequency of this stress wave into resonance with the $|(m_s =) - 1\rangle \leftrightarrow |+1\rangle$ spin transition to mechanically drive Rabi oscillations of an NV center spin ensemble. Using this capability, we measure the inhomogeneous dephasing time for an ensemble of mechanically controlled NV center spin qubits to be $T_2^* = 0.45 \pm 0.05$ μs and compare this result to T_2^* for magnetically driven qubits constructed from the same NV center ensemble. We find that the mechanically driven $\{-1, +1\}$ qubit coherence is similar to that of a magnetically driven $\{-1, +1\}$ qubit, and these $\{-1, +1\}$ qubits dephase twice as quickly as magnetically driven $\{0, -1\}$ or $\{+1, 0\}$ qubits.

NV centers couple to mechanical stress ($\sigma_\perp$ and $\sigma_\parallel$) and magnetic fields ($B_\perp$ and $B_\parallel$) through their ground-state spin Hamiltonian (shown schematically in Fig. 5.1a)

$$\begin{aligned} H_{NV} = (D_0 + \epsilon_\parallel \sigma_\parallel) S_z^2 + P I_z^2 + A_\parallel I_z S_z + \gamma_{NV} B_\parallel S_z \\ + \gamma_{NV} B_\perp S_x - \epsilon_\perp \sigma_x (S_x^2 - S_y^2) + \epsilon_\perp \sigma_y (S_x S_y + S_y S_x) \end{aligned} \tag{5.1}$$

where $D_0/2\pi = 2.87$ GHz is the zero-field splitting, $\gamma_{NV}/2\pi = 2.8$ MHz/G is the gyromagnetic ratio, $\epsilon_\perp/2\pi = 0.015$ MHz/MPa and $\epsilon_\parallel/2\pi = 0.012$ MHz/MPa are the perpendicular and axial stress coupling constants [32], $P/2\pi = -4.945$ MHz and $A_\parallel/2\pi = -2.166$ MHz are the hyperfine parameters [6, 80, 81], and S_x, S_y, S_z (I_x, I_y, I_z) are the x, y, and z components of the electronic (nuclear) spin-1 operator. By aligning $B_\parallel$ along one of the four possible NV center symme-

[1] See Section 5.3.1

try axis orientations, we define the z-axis of our coordinate system as depicted in Fig. 5.1b. In Sect. 5.3.2, we use the stiffness matrix for diamond to calculate $\epsilon_\perp$ and $\epsilon_\parallel$ from the strain coupling constants $d_\perp/2\pi = 21.5$ GHz/strain and $d_\parallel/2\pi = 13.3$ GHz/strain measured by Ovartchaiyapong, *et al* [32]. Non-axial stress $\sigma_\perp$ couples the $|-1\rangle$ and $|+1\rangle$ spin states, enabling coherent control of the magnetically-forbidden $\Delta m_s = \pm 2$ spin transition and providing direct access to the $\{-1, +1\}$ spin qubit. This qubit combination has recently become a topic of interest because it is isolated from thermal fluctuations [56] and can make a more sensitive magnetometer than either the $\{0, -1\}$ or $\{+1, 0\}$ qubit [56, 86].

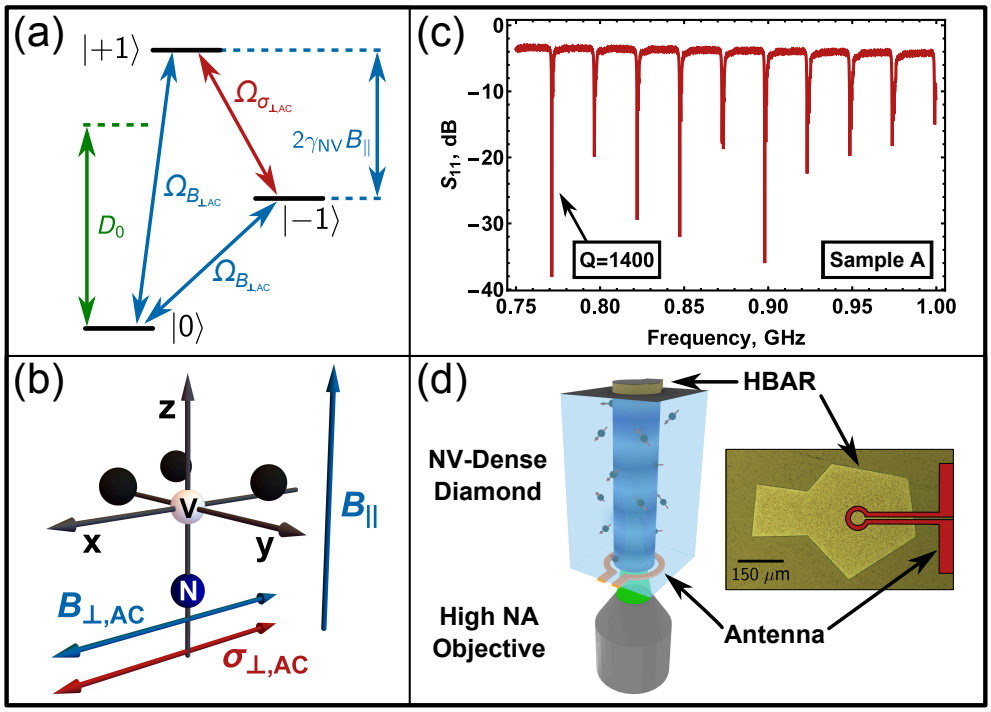

Figure 5.1: (a) Energy levels of the NV center ground state with corresponding energy separations and driving fields. (b) Schematic of the NV center with applied magnetic ($B_\perp$ and $B_\parallel$) and mechanical ($\sigma_\perp$) fields. (c) Reflected microwave power (S_{11}) as a function of frequency for the Sample A HBAR as measured with a network analyzer. The resonance at $\omega_{mech}/2\pi = 0.771$ GHz has a Q of 1400. (d) Device schematic (not to scale) and an optical micrograph of an HBAR with the shadow of the loop antenna on the reverse diamond face indicated in red. Apodizing the shape of the HBAR limits the formation of lateral mechanical modes.

5.2.2 Results

Devices

In this work, we use two devices, both fabricated from type IIa, $\langle 100 \rangle$ "optical grade" diamonds purchased from Element Six. These samples are specified to contain fewer than 1 ppm nitrogen impurities, and each contained a native NV ensemble as received. The first sample, Sample A, has an NV center density of ~ 110 NVs/μm^3, while Sample B has a density of ~ 120 NVs/μm^3.

To generate the large amplitude, high-frequency stress waves needed for coherent mechanical control, we fabricate high-overtone bulk acoustic resonators (HBARs) that use these single crystal diamonds as resonant cavities. The HBARs used for these measurements consist of either a 1.8 μm (Sample A) or a 2.5 μm (Sample B) zinc oxide (ZnO) piezoelectric film sandwiched between a patterned Al electrode and a Ti/Pt ground plane, all sputtered on one face of the diamond substrate. By driving an HBAR with a high-frequency voltage, we transduce stress waves inside the diamond. The diamond then acts as an acoustic Fabry-Pérot cavity to create standing wave resonances. Fig. 5.1c shows a network analyzer measurement of the microwave power reflected (S_{11}) from the Sample A HBAR with the $\omega_{mech}/2\pi = 771$ MHz mode ($Q = 1400$) used in these experiments indicated. Measurements on Sample B used a $\omega_{mech}/2\pi = 529$ MHz resonance with a Q of 4000. On the reverse side of each diamond, we fabricate a loop antenna that produces gigahertz-frequency magnetic fields for conventional magnetic spin control. Fig. 5.1d depicts a schematic version of the resulting device.

Rabi Driving with a Low Q Mechanical Mode

To perform mechanically driven spin coherence measurements, we first tune the axial magnetic field $B_{\|}$ to bring the spins into resonance with a high-frequency stress wave as described in Ref. [1]. At this resonant $B_{\|}$, we mechanically drive Rabi oscillations of the $\{-1, +1\}$ qubit. Fig. 5.2a shows the pulse sequence used to drive Rabi oscillations in the relatively low Q modes of Sample A. To initialize the NV center spins, we first optically polarize into $|0\rangle$ and then transfer the spin population from $|0\rangle$ to $|-1\rangle$ with a magnetic π-pulse. Next, we apply a mechanical Rabi pulse of length τ that is resonant with the $|-1\rangle \leftrightarrow |+1\rangle$ spin transition. To read out the spin signal, a second magnetic π-pulse shuttles the population in $|-1\rangle$ to $|0\rangle$. Fluorescence measurement of the $|0\rangle$ state population reveals how much spin population was transferred to $|+1\rangle$ according to the relation $P_{|+1\rangle} = 1 - P_{|0\rangle}$[2]. In order to maintain a constant average power to the device, we apply a second mechanical pulse at each data point of length $L - \tau$ where L is the length of the longest Rabi pulse. This pulse comes before fluorescence read out but does not affect our measurement since the spin population we detect has left the $\{-1, +1\}$ subspace. Fig. 5.2b shows mechanically driven Rabi oscillations as measured on Sample A for 33 dBm of input power to the HBAR.

The damping observed in Fig. 5.2b arises from a combination of spin dephasing from magnetic bath noise and dephasing derived from spatial variations in the amplitude of the stress standing wave within the spin ensemble. NV centers near an anti-node of the stress wave feel a larger Rabi frequency than NV centers near a node. The finite collection volume of our confocal microscope ne-

[2] In Section 5.3.3, we also repeat this measurement reading out the population from the $|+1\rangle$ state and observe similar behavior.

cessitates measuring a distribution of coupling strengths, which causes the measured spin signal to dephase. To account for both of these dephasing sources, we model the data in Fig. 5.2b with the spatially-weighted average

$$P_{|+1\rangle} = \frac{1}{3}\frac{1}{\int_0^\infty g(z,z_0)\,\mathrm{d}z} \times \int_0^\infty g(z,z_0)\frac{\Omega(z)^2}{\Omega(z)^2+\delta^2}\sin^2\left[\frac{1}{2}\sqrt{\Omega(z)^2+\delta^2}t\right]\,\mathrm{d}z \tag{5.2}$$

where the factor of $1/3$ arises because we drive only one of the unpolarized nuclear spin sublevels, $\Omega(z) = \Omega_{mech}|\sin\frac{2\pi z}{\lambda_A}|$ is the mechanical driving field, λ_A is the wavelength of the stress standing wave, and $g(z, z_0)$ represents a Gaussian approximation to the microscope point spread function (PSF) with a FWHM that grows linearly with the depth of focus inside the diamond z_0 as described in Ref. [1]. We assume resonant driving and include quasi-static spin bath noise as a random detuning δ drawn from a Gaussian distribution with a standard deviation $\sigma = \sqrt{2}/T_2^*$ [87]. The mechanical Ramsey measurement presented in Section 5.2.2 sets $T_2^* = 0.45 \pm 0.05$ μs in the $\{-1, +1\}$ subspace. With the parameters $\Omega_{mech}/2\pi = 1.0$ MHz, $\lambda_A = 19.9$ μm, and $z_0 = 18$ μm as inputs, we average 200 iterations of the simulation to produce the model curve in Fig. 5.2b, which is not a fit to the experimental data.

Rabi Driving with a High Q Mechanical Mode

For devices with Q-factors substantially larger than Sample A, we find a standard Rabi pulse sequence is not effective. In these devices, the large bandwidth of short microwave pulses reduces their spectral precision, which in turn distorts the coupling between the mechanical resonator and its microwave drive. This becomes important in the higher Q resonance of Sample B. To control this effect, we pulse the stress wave for the fixed duration $L = 3$ μs at each data

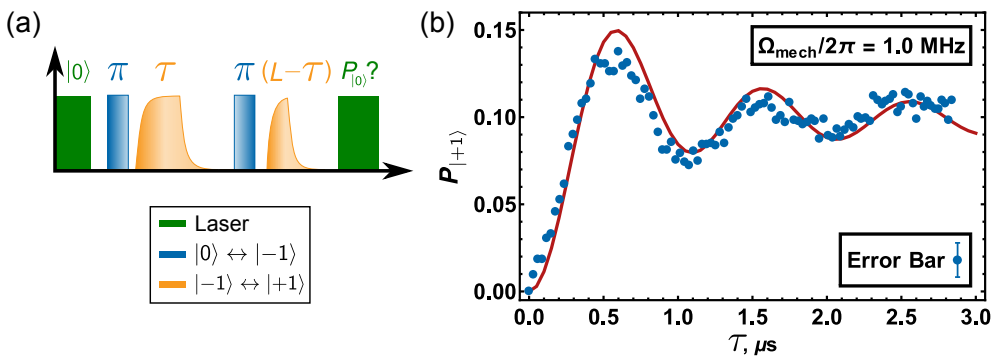

Figure 5.2: (a) Pulse sequence for mechanical Rabi driving on low Q devices. (b) Mechanically driven Rabi oscillations between the $|-1\rangle$ and $|+1\rangle$ spin states for the $\omega_m/2\pi = 771$ MHz mechanical mode of Sample A ($Q = 1400$). An input power of 33 dBm produces a Rabi frequency of $\Omega_{mech}/2\pi = 1.0$ MHz.

point. Because the stress wave only affects spins in the $\{-1, +1\}$ subspace, a pair of short (~ 30 ns) magnetic π-pulses separated by a fixed interval τ_{mag} controls the length of time the mechanical driving field is active. By sweeping this magnetic pulse pair through the mechanical pulse as shown in Fig. 5.3a, we measure mechanically driven Rabi oscillations in the $\{-1, +1\}$ subspace. For 33 dBm of input power, the mechanical driving field is $\Omega_{mech}/2\pi = 3.8$ MHz, which substantially exceeds the dephasing rate[3].

Fig. 5.3b shows a Rabi measurement using this protocol with the notable transition points in the sweep labeled and described in the figure caption. The model curve in Fig. 5.3b is the average solution of the Schrödinger equation for the spin population in $|+1\rangle$ after being driven by a segment of the mechanical pulse. We model the mechanical pulse with the functions $1 - e^{-\frac{t}{\tau_r}}$ for ring-up and $e^{-\frac{t-t_0}{\tau_r}}$ for ring-down where $\tau_r = 2Q/\omega_m$ is the time constant for the ringing [88] and $t_0 = L + \tau_r \log(1 - e^{-\frac{t}{\tau_r}})$ is a constant. As before, the model – which is not a fit to the data – accounts for driving field inhomogeneities by applying a spatially-weighted average over an approximated optical PSF and includes

[3]See Section 5.3.3

quasi-static magnetic bath noise through a randomized detuning. Section 5.3.3 provides additional details on the model.

For the measurement shown, the time between the two magnetic π-pulses is $\tau_{mag} = L + \tau_r = 5.41$ μs and $L = 3$ μs. As such, the critical delay $\tau_c = 6.03$ μs corresponds to the largest mechanical pulse area enclosed between the two magnetic π-pulses. To either side of this time step, the pulse area decreases at roughly the same rate. The asymmetry in the data about this point arises because for delays $\tau < \tau_c$ the mechanical pulse amplitude and thus the instantaneous driving field are higher than when $\tau > \tau_c$. This larger instantaneous driving field offers the spins better protection from magnetic bath noise as evinced by the larger amplitude Rabi oscillations. Our model correctly reproduces this asymmetry, demonstrating the possibility of using a mechanical driving field to achieve continuous dynamical decoupling of an NV center spin from a spin bath [89].

By modeling the resonator ringing as described above, we can convert the mechanical pulse area between the two magnetic pulses into the "square-pulse" units typically used in magnetic Rabi measurements. Fig. 5.3c shows mechanical Rabi oscillations plotted as a function of this normalized Rabi interval for measurements taken at several depths inside the diamond substrate. As expected, the oscillations dephase faster near a node in the stress wave due to driving field inhomogeneities within the ensemble. Near the antinode, however, the relative uniformity of the stress wave mitigates this depth-dependence and, thus, the dephasing from driving field inhomogeneities. As described in Sect. 5.3.3, our numerical model reproduces these depth dependent trends.

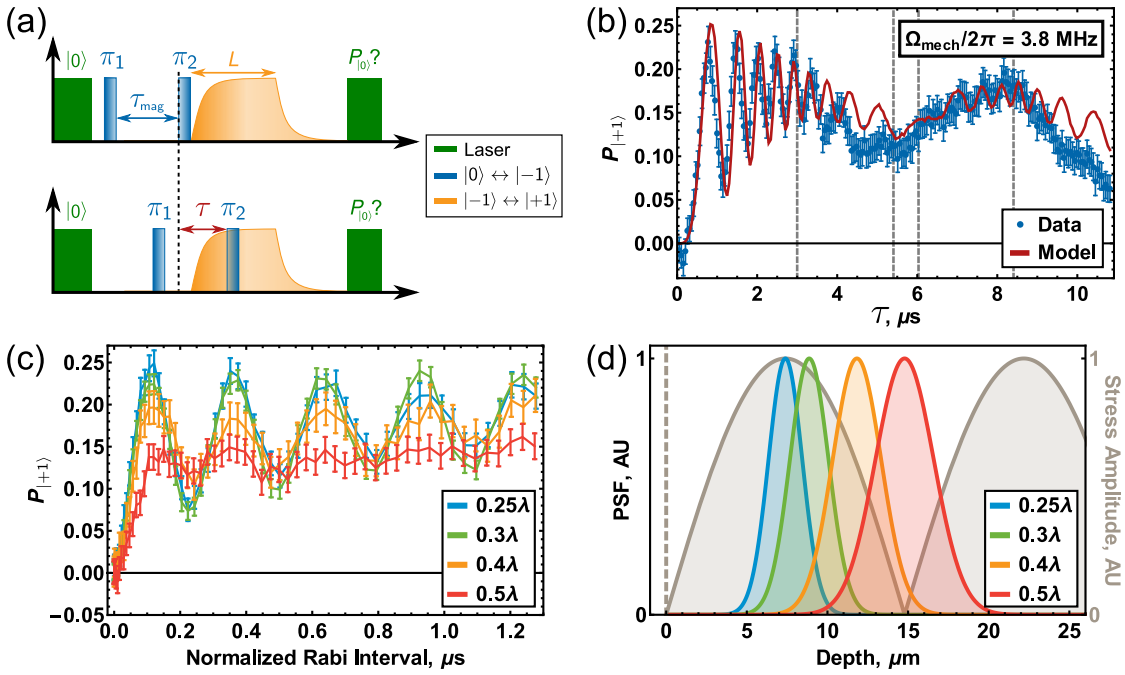

Figure 5.3: (a) Pulse sequence for mechanical Rabi driving on high-Q devices. (b) Mechanically driven Rabi oscillations for the $\omega_m/2\pi = 529$ MHz mechanical mode of Sample B ($Q = 4000$). The model curve is not a fit to the data. From left to right, the dashed lines correspond to π_2 entering the ring down portion of the mechanical pulse, π_1 entering the ring up, the maximum mechanical pulse area at τ_c, and π_1 entering the ring down. (c) Mechanically driven Rabi oscillations at different depths inside the diamond substrate plotted as a function of the normalized Rabi interval. An input power of 33 dBm produces a Rabi frequency of $\Omega_{mech}/2\pi = 3.8$ MHz. (d) A Gaussian approximation to the microscope point spread function (PSF) plotted at different focal depths inside the diamond. Inhomogeneities in the stress wave amplitude within the PSF increase the dephasing of the mechanically driven Rabi signal.

Ramsey Measurement of Spin Dephasing

The more traditional Rabi pulse protocol used for Sample A provides a direct means to implement conventional pulse sequences. From the data in Fig. 5.2b, we extract the $\pi/2$-pulse time and proceed to measure T_2^* of Sample A with a mechanical Ramsey pulse sequence. Fig. 5.4 shows the result of this measurement along with Ramsey measurements of T_2^* for magnetically driven $\{-1, +1\}$; $\{0, -1\}$; and $\{+1, 0\}$ qubits. Details on the pulse sequences used for each of

these measurements are provided in Sect. 5.3.4. Although selection rules forbid direct magnetic control of the $|-1\rangle \leftrightarrow |+1\rangle$ transition, magnetic control of the $\{-1, +1\}$ qubit can be accomplished indirectly by using either double-quantum pulses [86] or multi-pulse sequences [90]. Both of these alternatives use the $|0\rangle$ state as a waypoint in the $|-1\rangle \leftrightarrow |+1\rangle$ transition. To control the $\{-1, +1\}$ qubit magnetically, we employ the multipulse sequence described in Sect. 5.3.4.

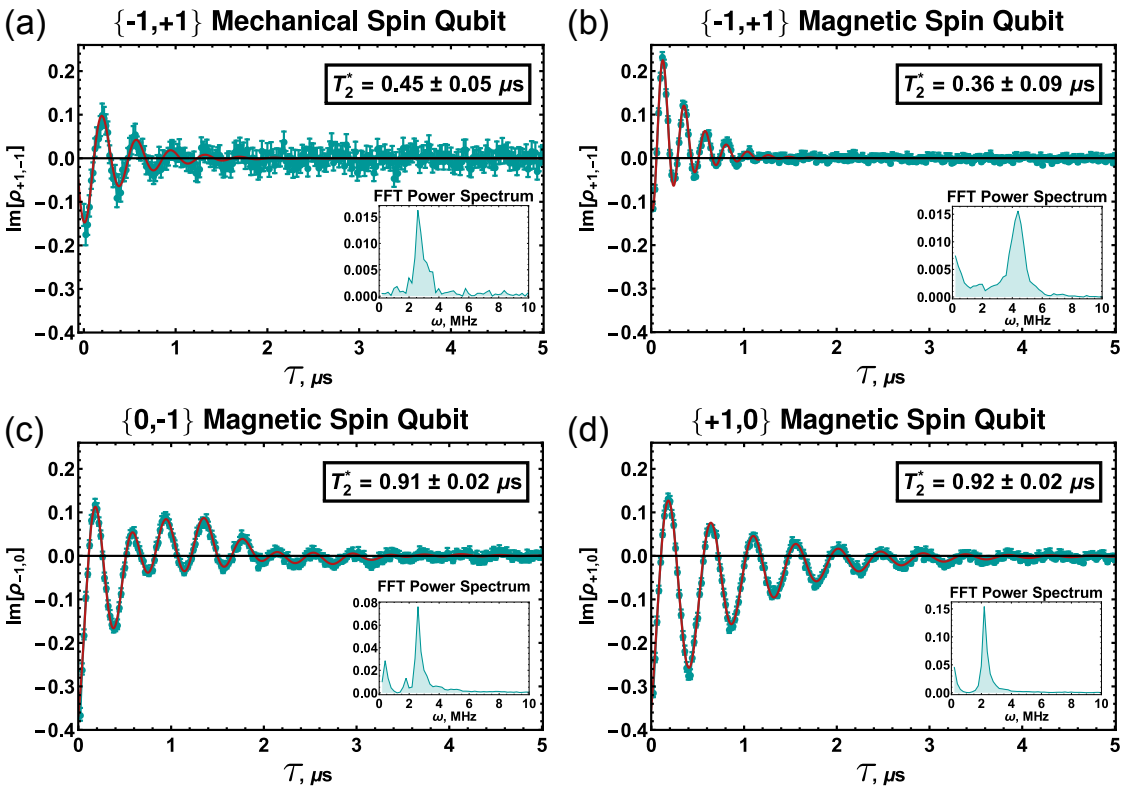

Figure 5.4: Ramsey data taken on Sample A for (a) a mechanically driven $\{-1, +1\}$ qubit ($\delta/2\pi$ =830 $\pm$ 40 kHz), (b) a magnetically driven $\{-1, +1\}$ qubit ($\delta/2\pi$ =140 $\pm$ 50 kHz), (c) a magnetically driven $\{0, -1\}$ qubit ($\delta/2\pi$ =350 $\pm$ 6 kHz), and (d) a magnetically driven $\{+1, 0\}$ qubit ($\delta/2\pi$ =17 $\pm$ 3 kHz).

We fit the three magnetically driven Ramsey measurements to the function

$$\begin{aligned} \mathrm{Im}[\rho_{ij}] = e^{-t/T_2^*}\{&C_1 \cos[(\delta + A_\parallel)t + \phi_1] \\ &+ C_2 \cos[\delta t + \phi_2] + C_3 \cos[(\delta - A_\parallel)t + \phi_3]\} \end{aligned} \tag{5.3}$$

where δ represents a detuning in the driving field, the amplitudes (C_1, C_2, C_3) allow for partial polarization of the nuclear sublevels, the constant phases (ϕ_1, ϕ_2, ϕ_3) account for pulse phasing errors, and $A_\parallel \rightarrow 2A_\parallel$ for the magnetically driven $\{-1, +1\}$ qubit. Since the mechanical driving field ($\Omega_{mech}/2\pi = 1.0$ MHz) does not overcome the hyperfine spacing ($2A_\parallel = 4.332$ MHz in the $\{-1, +1\}$ subspace), it drives only one of the nitrogen nuclear spin sublevels. Therefore, we fit our mechanical Ramsey data to the function

$$\mathrm{Im}[\rho_{+1,-1}] = e^{-t/T_2^*} C_1 \cos[(\delta + \omega_{rot})t + \phi_1] \tag{5.4}$$

where $\omega_{rot}/2\pi = 3.5$ MHz describes an experimentally introduced phase that accumulates at $\omega_{rot}t$ to visualize the decay envelope[4]. Our fitting procedure varies δ, T_2^*, C_i, and ϕ_i as free parameters. Since we measure the coherence of a spin ensemble, we extract T_2^* from an exponentially decaying envelope rather than from the Gaussian decay expected for a single NV center [91]. Fig. 5.4 displays the values of T_2^* extracted from these fits, and the figure caption lists the measured detunings δ.

The inset within each plot depicts a Fourier power spectrum of the corresponding data. For the magnetic qubits, the Fourier spectra show one peak at $\omega = \delta$ corresponding to the $|(m_I =)0\rangle_I$ nuclear spin state. The magnetic $\{0, -1\}$ ($\{+1, 0\}$) qubit also shows a second peak with roughly twice the amplitude at $\omega_\pm = A_\parallel \mp \delta$ ($\omega_\pm = A_\parallel \pm \delta$) that represents nearly superposed peaks from the $|+1\rangle_I$ and $|-1\rangle_I$ nuclear states. For the magnetic $\{-1, +1\}$ qubit, this $|\pm 1\rangle_I$ peak appears at $\omega_\pm = 2A_\parallel \pm \delta$. The Fourier spectrum of the mechanical $\{-1, +1\}$ qubit shows only one peak at $\omega = \omega_{rot} + \delta$ because the mechanical driving field drives only one nuclear sublevel.

[4] See Section 5.3.4

For the $\{-1, +1\}$ qubit, we find that T_2^* measured mechanically (0.45 ± 0.05 μs) agrees well with T_2^* measured magnetically (0.36 ± 0.09 μs) where the uncertainties equal the square root of the variance in the fitting parameter. The $\{0, -1\}$ and $\{+1, 0\}$ qubits have dephasing times $T_2^* = 0.91 \pm 0.02$ μs and $T_2^* = 0.92 \pm 0.02$ μs, respectively—approximately twice as long as that of the $\{-1, +1\}$ qubit. This agrees with previous measurements performed on a single NV center in low magnetic field [90, 56]. This reduced coherence time does not diminish the $\{-1, +1\}$ qubit's metrological utility because this qubit accumulates phase twice as fast as the longer-lived $\{+1, 0\}$ and $\{0, -1\}$ qubits, thus reducing the integration time necessary to detect an identical signal [56, 86]. Additionally, pulsed dynamical decoupling sequences could be implemented in improved devices that take advantage of an anomalous decoherence effect unique to the $\{-1, +1\}$ qubit. This effect can make the spin coherence of the $\{-1, +1\}$ qubit longer than the spin coherence of either the $\{0, -1\}$ or the $\{+1, 0\}$ qubit decoupled under an equivalent protocol [90].

5.2.3 Discussion

A number of engineering improvements can advance the performance of our devices. First, we expect additional refinements in device fabrication to increase the Q of our devices, which could provide at least a factor of 5 enhancement in the mechanical driving field [73]. Also, working in higher electronic purity diamond will dramatically reduce spin bath induced dephasing, and working with either a single spin or a plane of NV centers would remove dephasing from driving field inhomogeneities. Taken together, these advances can unlock high fidelity quantum control of a mechanically driven qubit.

Our results demonstrate coherent control of all three ground state spin transitions. By simultaneously driving the $|0\rangle \leftrightarrow |-1\rangle$ and $|+1\rangle \leftrightarrow |0\rangle$ transitions magnetically and the $|-1\rangle \leftrightarrow |+1\rangle$ transition mechanically, a Δ-system in which all three states are coupled by a closed-loop interaction contour can be created within the NV center ground state. Such a system requires at least one parity non-conserving driving field, making Δ-systems an uncommon extension of the more typical Λ-system, which has been well explored in NV centers [23, 92, 93, 84, 94, 28]. In a Λ-system, driving field amplitudes and detunings balance to enable phenomena such as coherent population trapping [92, 93] and electromagnetically induced transparency [23, 94]. In a Δ-system, similar phenomena occur but with an additional sensitivity to the relative phases of the driving fields [95, 96, 97]. Implementing an NV center Δ-system could, for instance, create a phase induced transparency where the phase of a magnetic driving field tunes the absorption of the mechanical driving field. Such a system could have value in NV center optomechanics experiments as a phase-controlled switch to rapidly gate spin-phonon interactions. Another application could be measuring the relative phase of a resonating mechanical proof mass in an inertial sensor.

5.2.4 Conclusions

In summary, we use a high-frequency mechanical resonator to drive coherent Rabi oscillations of an NV center spin ensemble with driving fields up to $\Omega_{mech}/2\pi = 3.8$ MHz. This enabled a comparison of the inhomogeneous dephasing time T_2^* of a mechanically driven $\{-1, +1\}$ qubit with that of magnetically driven $\{-1, +1\}$; $\{0, -1\}$; and $\{+1, 0\}$ qubits. We found that, for both

mechanical and magnetic driving, the $\{-1, +1\}$ qubit dephases twice as fast as the $\{0, -1\}$ and $\{+1, 0\}$ qubits. These results establish the possibility of creating a phase-sensitive Δ-system within the NV center ground state, which could have applications in metrology, optomechanics, and quantum control.

5.3 Supplementary Information

5.3.1 Device Improvements

A number of refinements in device fabrication have improved the performance of the HBAR devices presented in this work over the device discussed in Ref. [1], enabling coherent spin control driven with a mechanical resonator. Our most important advance was to develop in-house growth of piezoelectric ZnO for use with the HBAR transducer to replace the foundry grown piezoelectric AlN used in Ref. [1]. Although the two films perform comparably, the faster fabrication time of a fully local process enabled rapid device development. We were able to engineer a better impedance match between the HBAR and the microwave driving circuit. Additionally, as pictured in Fig. 5.5, we apodized the shape of the HBAR top contact to inhibit lateral modes. These modes drain power from the device without contributing to the stress wave of interest. Thus, by apodizing the top contact, we increased the efficiency of the HBAR. Additionally, we changed the geometry of the back-side microwave antenna, minimizing its contact with the shadow of the HBAR active region. Combined, these small optimizations and cleaner fabrication generated higher quality devices with better power coupling to the microwave circuit.

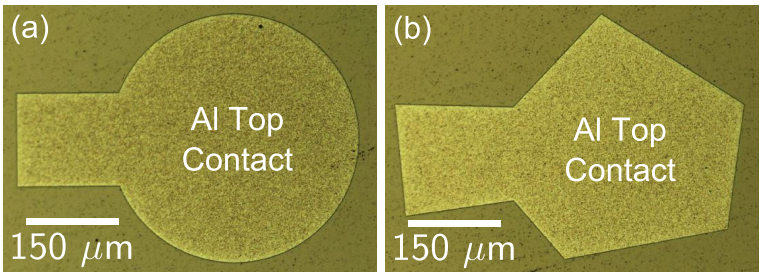

Figure 5.5: (a) A circular HBAR as was used in [1]. (b) An apodized HBAR design as used in the current work.

C_{11}	C_{12}	C_{44}
1076.4 GPa	125.2 GPa	577.4 GPa

Table 5.1: Stiffness constants for diamond [5].

5.3.2 NV Center Stress Coupling

$$\begin{pmatrix} \sigma_{xx} \\ \sigma_{yy} \\ \sigma_{zz} \\ \sigma_{yz} \\ \sigma_{zx} \\ \sigma_{xy} \end{pmatrix} = \begin{pmatrix} C_{11} & C_{12} & C_{12} & 0 & 0 & 0 \\ C_{12} & C_{11} & C_{12} & 0 & 0 & 0 \\ C_{12} & C_{12} & C_{11} & 0 & 0 & 0 \\ 0 & 0 & 0 & C_{44} & 0 & 0 \\ 0 & 0 & 0 & 0 & C_{44} & 0 \\ 0 & 0 & 0 & 0 & 0 & C_{44} \end{pmatrix} \begin{pmatrix} \epsilon_{xx} \\ \epsilon_{yy} \\ \epsilon_{zz} \\ \epsilon_{yz} \\ \epsilon_{zx} \\ \epsilon_{xy} \end{pmatrix} \tag{5.5}$$

to convert strain/GHz into GPa/GHz (stress/GHz). The elastic constants C_{ij} are given in Table 5.1. Finally, we rotate back into the coordinates of the NV center to find the stress coupling constants $\epsilon_\perp/2\pi = 0.015$ MHz/MPa and $\epsilon_\parallel/2\pi = 0.012$ MHz/MPa used in Sect. 5.2.

5.3.3 Mechanical Rabi Measurements

Readout Through $|+1\rangle$

As a control, we performed a second type of Rabi measurement. In this alternative pulse sequence, after optically pumping the NV center into $|0\rangle$ we once again apply a magnetic π-pulse to resonantly move the population from $|0\rangle$ to $|-1\rangle$. We then pulse the resonant mechanical driving field for a length τ to drive the $|-1\rangle \leftrightarrow |+1\rangle$ transition. Finally, we use a magnetic adiabatic passage to robustly transfer the population that was driven into $|+1\rangle$ to $|0\rangle$ where we read out the spin state optically. This differs from the Rabi measurement presented in Sect. 5.2 in that we extract population from $|+1\rangle$, not $|-1\rangle$, for optical readout.

Fig. 5.6 shows the results of this measurement plotted alongside a mechanically driven Rabi measurement that uses a magnetic adiabatic passage to transfer population from $|-1\rangle$ to $|0\rangle$ after the mechanical Rabi pulse. Both of these measurements were done on Sample A. As expected, the results are nearly identical. The difference in amplitudes comes from fidelity differences between the $|+1\rangle \leftrightarrow |0\rangle$ and $|0\rangle \leftrightarrow |-1\rangle$ magnetic pulses.

Mechanical Rabi Sequence for Sample B

Fig. 5.7a shows the mechanical Rabi oscillations plotted in Fig. 5.3b of Sect. 5.2. This measurement was taken by sweeping a pair of magnetic π-pulses through a fixed-length mechanical pulse. To further elucidate this pulse sequence, Fig. 5.7b provides a snapshot of the pulse sequence at each of the notable points indicated by dashed lines in Fig. 5.7a and described in the figure caption.

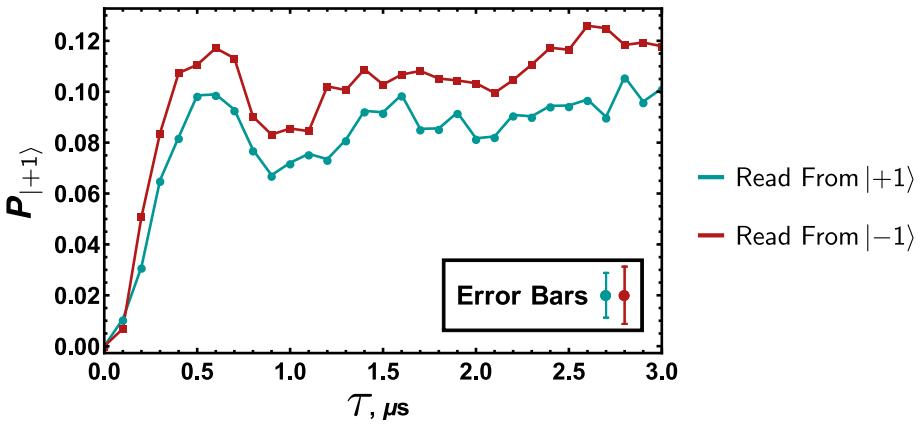

Figure 5.6: Mechanically driven Rabi oscillations as read out from the $|+1\rangle$ (blue) and $|-1\rangle$ (red) spin states. These measurements were performed on Sample A.

We model the ringing of a normalized mechanical driving field with the functions $1-e^{-\frac{t}{\tau_r}}$ for ring-up and $e^{-\frac{t-t_0}{\tau_r}}$ for ring-down where $t_0 = L+\tau_r \log(1-e^{-\frac{t}{\tau_r}})$ and $\tau_r = 2Q/\omega_m$ [88]. These functions allow us to compute the mechanical pulse area enclosed between the two magnetic π-pulses for each value of τ. Fig. 5.7b plots this normalized Rabi interval as a function of τ.

Mechanical Rabi Model for Sample B

To fit the mechanical Rabi data shown in Fig. 5.3b of Sect. 5.2, we solve the Schrödinger equation to find the population in $|+1\rangle$ after applying the relevant portion of an $L = 3$ μs mechanical pulse. We use the Hamiltonian

$$H_{up} = \begin{pmatrix} \delta & 0 & \frac{1}{2}\Omega(z)(1-e^{-\frac{t}{\tau_r}}) \\ 0 & 0 & 0 \\ \frac{1}{2}\Omega(z)(1-e^{-\frac{t}{\tau_r}}) & 0 & -\delta \end{pmatrix} \tag{5.6}$$

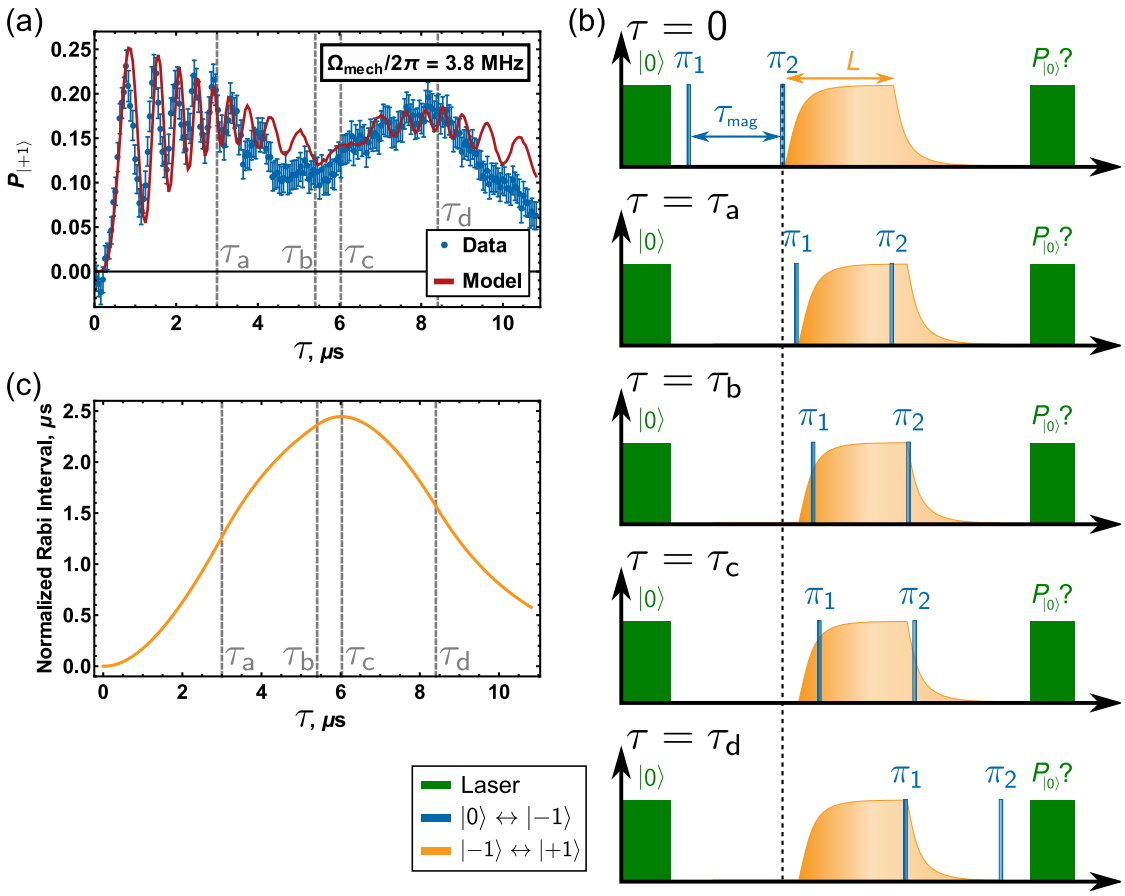

Figure 5.7: (a) Rabi oscillations driven mechanically with a high Q mechanical resonator. From left to right, the dashed lines correspond to π_2 entering the ring down portion of the mechanical pulse, π_1 entering the ring up, the maximum mechanical pulse area τ_c, and π_1 entering the ring down. (b) Pulse sequence at each of the notable times labeled in (a) and (c). (c) Mechanical pulse area enclosed between the two magnetic π-pulses as a function of τ. For a mechanical pulse normalized to its amplitude after ring up, this pulse area corresponds to the normalized Rabi interval.

when the resonator is ringing up and the Hamiltonian

$$H_{down} = \begin{pmatrix} \delta & 0 & \frac{1}{2}\Omega(z)e^{-\frac{t-t_0}{\tau_r}} \\ 0 & 0 & 0 \\ \frac{1}{2}\Omega(z)e^{-\frac{t-t_0}{\tau_r}} & 0 & -\delta \end{pmatrix} \tag{5.7}$$

when the resonator is ringing down. Quasi-static magnetic bath noise takes the form of a randomized detuning δ drawn from a Gaussian distribution with a

standard deviation $\sigma = \sqrt{2}/T_2^*$ [87]. The magnetic Ramsey measurement shown in Fig. 5.8 sets $T_2^* = 0.68\ \mu$s.

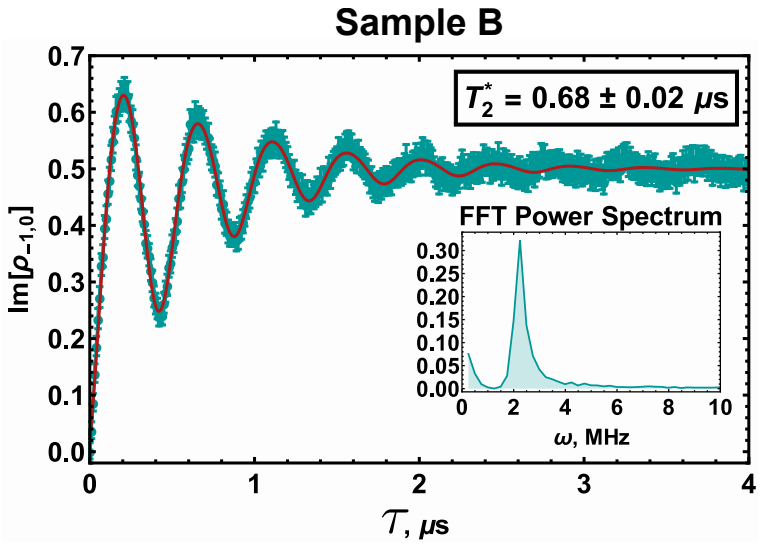

Figure 5.8: Magnetic Ramsey measurement of T_2^* for Sample B in the $\{0, -1\}$ subspace.

Defining the result of this computation as the function $f(\tau, \Omega(z))$, we then perform a spatially-weighted average over the point spread function (PSF) of our confocal microscope to account for spatial inhomogeneities in our mechanical driving field. The resulting signal takes the form

$$P_{|+1\rangle} = \frac{C}{\int_0^\infty g(z, z_0)\,\mathrm{d}z} \int_0^\infty g(z, z_0) f(\tau, \Omega(z))\,\mathrm{d}z \tag{5.8}$$

where C accounts for partial polarization of the nuclear spin sublevel, $\Omega(z) = \Omega_{mech}|\sin\frac{2\pi z}{\lambda_B}|$ is the mechanical driving field, λ_B is the wavelength of the stress wave, and $g(z, z_0)$ describes a Gaussian approximation to a PSF centered at the focal depth z_0 with a depth dependent FWHM as described in Ref. [1]. To produce the model curve in Fig. 5.3b of Sect. 5.2, we used the parameters $\Omega_{mech}/2\pi = 3.8$ MHz, $z_0 = 5.9\ \mu$m, $C = 0.414$ (measured with mechanically driven spin resonance), and $\lambda_B = 29.6\ \mu$m. The simulation was repeated 200 times, and these results were averaged to produce the final curve.

Depth Dependent Mechanical Rabi Simulations

In Fig. 5.9, we use the model developed in subsection 5.3.3 to simulate mechanical Rabi measurements taken at various depths inside the diamond substrate. The simulations, which are not fits to any data, correctly reproduce the experimentally observed decrease in the visibility of the Rabi oscillations for measurements taken as the focal depth approaches a node of the stress wave. Because the inhomogeneities in the mechanical driving field are largest near a stress wave node, the spins within our collection volume dephase more quickly near a node, reducing the visibility of the Rabi oscillations.

The simulation also reproduces the limited sensitivity in the frequency of the Rabi oscillations to the measurement depth. This limited sensitivity arises in part because, within the finite collection volume of our microscope, the NV centers that experience the largest Rabi field will be the best protected against dephasing. The visibility of these faster Rabi oscillations can thus be larger than the slower Rabi oscillations also present in the signal, even if the spins driven at slower Rabi frequencies are more optimally positioned within our collection volume. This apparent insensitivity of Rabi frequency to position also arises in part from purely geometric considerations, which we confirmed by separately performing simulations that do not account for decoherence.

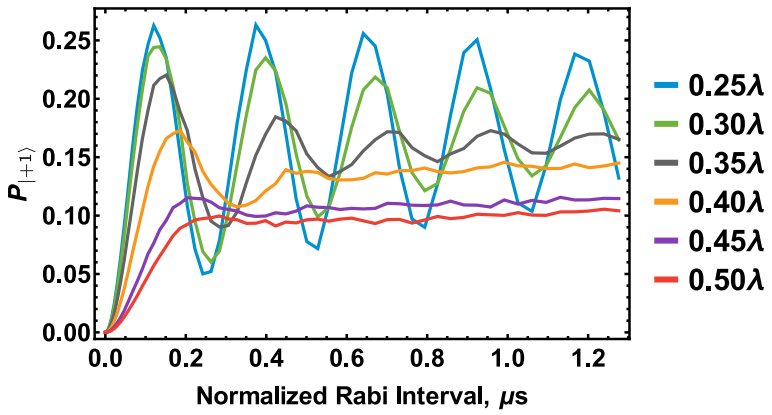

Figure 5.9: Mechanical Rabi measurements simulated with the numerical model detailed in subsection 5.3.3 above for several different measurement depths. The depth is measured relative to the wavelength λ of the stress wave.

5.3.4 Ramsey Measurements

Ramsey Pulse Sequences

Fig. 5.10 shows the pulse sequences used for the Ramsey measurements presented in Sect. 5.2. To eliminate experimental artifacts, we modified the typical Ramsey measurement to include a second measurement for each data point. We first execute the typical $\pi/2$—τ—$\pi/2$ Ramsey sequence. Immediately afterward, we perform a $\pi/2$—τ—$(-\pi/2)$ sequence. The difference of these two measurements equals twice the imaginary portion of the qubit's coherence $\mathrm{Im}[\rho_{i,j}]$ ($i, j \in \{(m_s =) + 1, 0, -1\}$, $i \neq j$). We further modify the Ramsey sequence for the mechanically driven qubit by advancing the phase of the second $\pi/2$-pulse by $\omega_{rot}(\tau + \tau_{\pi/2})$. This extra phase shift introduces a known periodicity to the measurement that aids visualization of the decay envelope.

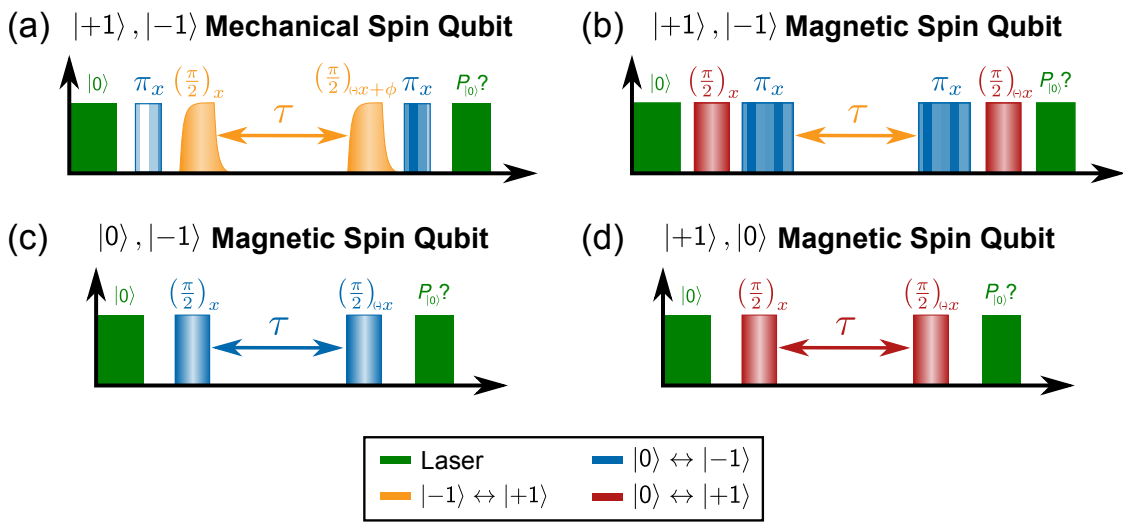

Figure 5.10: Pulse sequences used for the Ramsey measurements presented in Sect. 5.2.

Ramsey Measurement Normalization

Two measurements were used to normalize the spin contrast for the magnetic Ramsey measurements in the $\{+1, 0\}$ and $\{0, -1\}$ subspaces. The maximum spin signal y_{NP} is measured by optically pumping the NV center into $|0\rangle$, shuttering the laser for the fixed dark time in which no pulses were applied, and then reading out the NV center fluorescence. Applying a single magnetic π-pulse to the relevant qubit during that dark time gives the minimum spin signal y_π. Defining the $\pi/2$—τ—$\pi/2$ measurement results as y_+ and the $\pi/2$—τ—$(-\pi/2)$ measurement results as y_-, the expression

$$\mathrm{Im}[\rho_{ij}] = \frac{1}{2}\frac{y_+ - y_-}{y_{NP} - y_\pi} \tag{5.9}$$

gives the normalized coherence of the $|i\rangle, |j\rangle$ qubit.

For the magnetic $\{-1, +1\}$ qubit Ramsey measurement, the same "no pulse" measurement gives the maximum spin signal y_{NP}. We define the minimum spin

signal y_π as the average of the signal from a single magnetic π-pulse on the $\{+1, 0\}$ qubit and the signal from a single magnetic π-pulse on the $\{0, -1\}$ qubit.

For the mechanically driven $\{-1, +1\}$ qubit, the "no pulse" measurement once again sets the maximum spin signal for the mechanically driven $\{-1, +1\}$ qubit. The minimum spin signal is set by a π_{mag}—π_{mech}—π_{mag} pulse sequence. Here, π_{mag} corresponds to a magnetic π-pulse on the $\{0, -1\}$ qubit, and π_{mech} describes a mechanical π-pulse on the $\{-1, +1\}$ qubit.

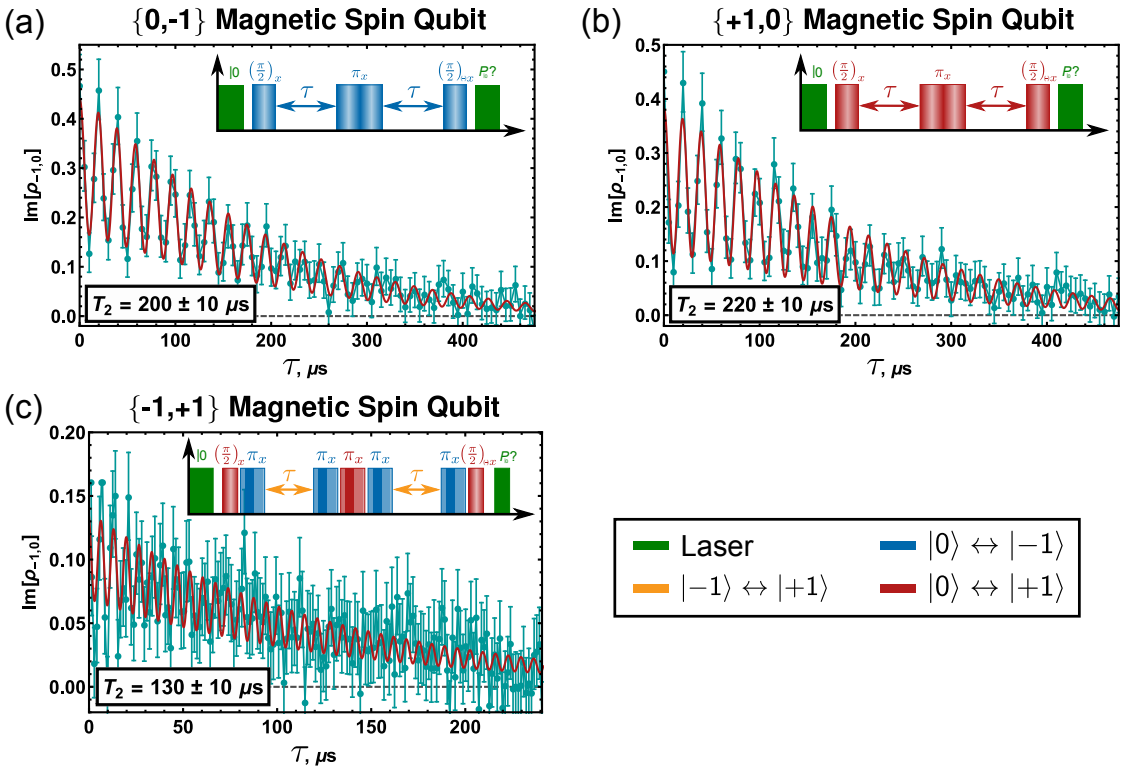

Figure 5.11: Hahn echo data for (a) a magnetically driven $\{0, -1\}$ qubit, (b) a magnetically driven $\{+1, 0\}$ qubit, and (c) a magnetically driven $\{-1, +1\}$ qubit. The pulse sequence for each measurement is inset within each plot.

5.3.5 Hahn Echo Measurements

We performed magnetic Hahn echo measurements of the homogeneous dephasing time T_2 in Sample A. We were unable to perform a mechanical Hahn echo experiment as intrinsic spin dephasing in our device limited the spin contrast after a mechanically driven 2π nutation to the prohibitive value of $\approx 1\%$. Fig. 5.11 shows the Hahn echo data for each magnetically driven qubit examined in Sect. 5.2. Once again, we measure roughly twice the coherence for the $\{+1, 0\}$ and $\{0, -1\}$ qubits when compared to the $\{-1, +1\}$ qubit.

5.4 Acknowledgments

Research support for Chapter 5 was provided by the Office of Naval Research (ONR). ERM received support from the Department of Energy Office of Science Graduate Fellowship Program (DOE SCGF), made possible in part by the American Recovery and Reinvestment Act of 2009, administered by ORISE-ORAU under contract no. DE-AC05-06OR23100. We also acknowledge partial support from a seed project through the Cornell Center for Materials Research, an NSF MRSEC (DMR-1120296). Device fabrication was performed in part at the Cornell NanoScale Science and Technology Facility, a member of the National Nanotechnology Infrastructure Network, which is supported by the National Science Foundation (Grant ECCS-0335765), and at the Cornell Center for Materials Research.

CHAPTER 6

CONTINUOUS DYNAMICAL DECOUPLING OF A SINGLE DIAMOND NITROGEN-VACANCY CENTER SPIN WITH A MECHANICAL RESONATOR [3]

6.1 Chapter Abstract

Inhomogeneous dephasing from uncontrolled environmental noise can limit the coherence of a quantum sensor or qubit. For solid state spin qubits such as the nitrogen-vacancy (NV) center in diamond, a dominant source of environmental noise is magnetic field fluctuations due to nearby paramagnetic impurities and instabilities in a magnetic bias field. In this work, we use ac stress generated by a diamond mechanical resonator to engineer a dressed spin basis in which a single NV center qubit is less sensitive to its magnetic environment. For a qubit in the thermally isolated subspace of this protected basis, we prolong the dephasing time T_2^* from 2.7 ± 0.1 μs to 15 ± 1 μs by dressing with a $\Omega/2\pi = 581 \pm 2$ kHz mechanical Rabi field. Furthermore, we develop a model that quantitatively predicts the relationship between Ω and T_2^* in the dressed basis. Our model suggests that a combination of magnetic field fluctuations and hyperfine coupling to nearby nuclear spins limits the protected coherence time over the range of Ω accessed here. We show that amplitude noise in Ω will dominate the dephasing for larger driving fields.

6.2 Main Text

6.2.1 Introduction

The triplet spin of the nitrogen-vacancy (NV) center in diamond has become a foundational component in both quantum metrology and future quantum information technologies [63, 98]. For sensing, the inhomogeneous dephasing time T_2^* of an NV center spin qubit can limit sensitivity to quasi-static fields. For quantum information applications, T_2^* can limit the number and the duration of gate operations that a qubit can undergo. Pulsed dynamical decoupling (PDD) techniques based on the principle of spin echoes refocus inhomogeneous dephasing and can extend T_2^* to the homogeneous spin dephasing time T_2 or longer [99, 100, 101, 102, 103, 104]. These periodic pulse sequences enable precision sensing and long-lived quantum states, but they come with drawbacks. They usually limit sensing to a narrow bandwidth and erase signal built up from quasi-static fields. Moreover, commuting echo pulses with gate operations makes decoupling during multi-qubit gates a nontrivial task [105].

Continuous dynamical decoupling (CDD) offers an alternative method for prolonging T_2^* that can be used when the limitations of PDD become too restrictive. NV center CDD protocols forego the standard Zeeman spin state basis $\{(m_s =) + 1, 0, -1\}$ in favor of an engineered basis in which the "dressed" eigenstates are less sensitive to environmental noise than the bare spin states [35, 16, 106, 107, 108, 109, 110, 111, 112, 113]. For an NV center spin qubit, magnetic field fluctuations from nearby paramagnetic impurities and instabilities in a magnetic bias field typically dominate dephasing. A qubit composed of dressed states designed to be more robust to these fluctuations could have a pro-

longed T_2^* and could be used for precision sensing of quasi-static, non-magnetic fields such as temperature [57] or strain. For quantum information processing, CDD allows decoupling to continue during gate operations, thus protecting both qubit and gate from dephasing [106, 108].

NV center CDD has typically been performed by magnetically driving the $|0\rangle \leftrightarrow |+1\rangle$ and $|0\rangle \leftrightarrow |-1\rangle$ spin transitions. Advances in diamond mechanical resonator fabrication [62, 85, 1, 31, 32, 50] have enabled the use of ac lattice strain to coherently drive the magnetically forbidden $|+1\rangle \leftrightarrow |-1\rangle$ spin transition as shown in Fig. 6.1a [2]. This has in turn enabled mechanical CDD [33] in which continuous driving of the $|+1\rangle \leftrightarrow |-1\rangle$ transition creates a dressed basis that cannot be accessed with conventional magnetic spin control. The mechanically dressed basis has eigenstates $\{0, m, p\}$ where $|m\rangle$ and $|p\rangle$ are mixtures of only $|+1\rangle$ and $|-1\rangle$. The $|+1\rangle$ and $|-1\rangle$ states respond diametrically to magnetic fields, making $|m\rangle$ and $|p\rangle$ less sensitive to magnetic field fluctuations than their undressed constituents.

In this work, we perform mechanical CDD to prolong T_2^* of single NV centers and quantify how T_2^* scales with the mechanical dressing field. We determine that, within a thermally isolated subspace of the mechanically dressed basis, a combination of magnetic field fluctuations and coupling to unpolarized nuclear spins limits mechanical CDD over the range of cw dressing fields accessible to our device. Using experiments and theory, we show that for larger driving fields amplitude noise in the mechanical dressing field will become the dominant source of dephasing.

Compared to magnetic CDD protocols, mechanically dressing the NV center spin has the key benefit that the $|0\rangle$ state is left unperturbed. This elimi-

nates the need to adiabatically dress and undress the NV center before and after each measurement—a process that can take as long as 50 μs each way [108]. Moreover, the Rabi fields generated by a mechanical resonator are noise filtered above a cutoff frequency ω_c determined by the quality factor Q and the frequency of the resonance mode ω_{mech}. This is a valuable feature since driving field noise has previously limited magnetic CDD efforts [107, 108, 114, 87, 115, 110].

6.2.2 Mechanically Dressed States

Our derivation of the mechanically dressed energy levels begins in the conventional $\{+1, 0, -1\}$ Zeeman basis. As depicted in Fig. 6.1b, we consider a static magnetic field b aligned along the NV center symmetry axis that is subject to fluctuations δb and a mechanical driving field Ω that is subject to amplitude fluctuations $\delta\Omega$. We work within the $m_I = +1$ sublevel of the ^{14}N hyperfine manifold. In diamonds with a natural distribution of carbon isotopes, nearby ^{13}C nuclear spins typically couple to the NV center spin. Weak coupling to a single ^{13}C spin is described by the hyperfine perturbation $H_C = A_\parallel S_z I_z$ where S_z and I_z are the spin-1 and spin-$\frac{1}{2}$ Pauli matrices, respectively, and $A_\parallel$ is the coupling strength [70]. Applying the rotating wave approximation, we transform into the reference frame rotating at $\frac{1}{2}\omega_{\text{mech}} = \frac{1}{2}(2\gamma b + \Delta)$ where Δ gives the detuning of ω_{mech} from the $|+1\rangle \leftrightarrow |-1\rangle$ spin state splitting. Diagonalizing the resulting Hamiltonian gives eigenstates $\{0, m, p\}$ with energies $\{-D, -\frac{1}{2}\sqrt{(\Omega + \delta\Omega)^2 + \xi_\pm^2}, \frac{1}{2}\sqrt{(\Omega + \delta\Omega)^2 + \xi_\pm^2}\}$ where $\xi_\pm \equiv \Delta + 2\gamma\delta b \pm A_\parallel$ for the $m_I = \pm\frac{1}{2}$ sublevel of the ^{13}C manifold. Here, $\gamma/2\pi = 2.8$ MHz/G is the NV center gyromagnetic ratio and $D \simeq D_0 + \frac{dD}{dT}\Delta T$ is the zero-field splitting

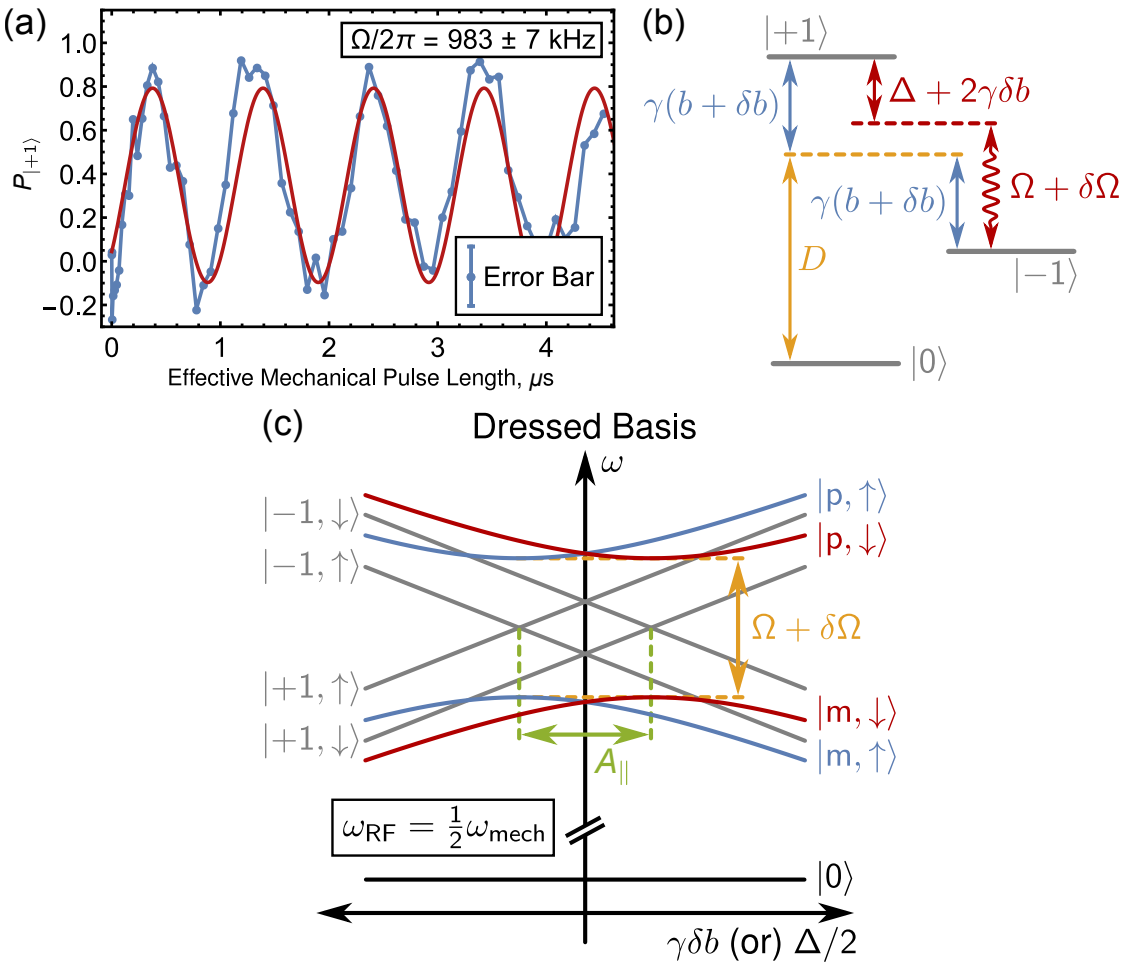

Figure 6.1: (a) Mechanically driven Rabi oscillations between the $|-1\rangle$ and $|+1\rangle$ states of a single NV center within the $m_I = +1$ sublevel of the ^{14}N hyperfine manifold (measurement details in Sect. 6.3.1). (b) NV center Zeeman states subject to a static magnetic field $b + \delta b$ and a mechanical driving field $\Omega + \delta\Omega$. (c) Energies of the undressed and dressed eigenstates plotted as a function of both $\gamma\delta b$ and $\Delta/2$ in a reference frame rotating at $\omega_{RF} = \frac{1}{2}\omega_{\text{mech}}$. We include hyperfine sublevels from a nearby ^{13}C nuclear spin coupled with a strength $A_\parallel$.

where $D_0/2\pi = 2.87$ GHz and $\frac{dD}{dT} = -74 \times 2\pi$ kHz/°C is the temperature dependence of D [6, 13, 57, 116]. Sect. 6.3.2 provides a more detailed derivation of the mechanically dressed Hamiltonian.

Fig. 6.1c plots the energy levels of the dressed and undressed eigenstates as a function of both $\gamma\delta b$ and $\Delta/2$. The Larmor frequency $\omega_{i,j}$ at which a qubit

accumulates phase is given by the energy splitting between the $|i\rangle$ and $|j\rangle$ qubit states. Variations in δb will cause $\omega_{i,j}$ to fluctuate in time, dephasing the qubit. Mechanically dressing the NV center opens an avoided crossing between the $|m\rangle$ and $|p\rangle$ states at $\gamma\delta b = \frac{1}{2}(\Delta \pm A_{\parallel})$, which reduces the sensitivity of $\omega_{i,j}$ to variations in δb and protects the qubit from dephasing.

6.2.3 Device Details

We use a high-overtone bulk acoustic resonator (HBAR) to generate the large amplitude ac lattice strain needed to coherently drive NV center spin transitions. Our mechanical resonator is fabricated from a type IIa, $\langle 100 \rangle$-oriented diamond specified to contain fewer than 5 ppb nitrogen impurities. A uniform distribution of individually addressable NV centers was introduced via irradiation with 2 MeV electrons at a fluence of $\sim 1.2 \times 10^{14}$ cm^{-2} followed by annealing at 850°C for 2 hours. The NV centers studied in this work are located at a depth of ~ 47 μm.

In contrast to our previous studies of spectroscopic [1] and coherent [2] interactions between an NV center ensemble and a mechanical resonator, here we study the coherence of a single NV center under a continuous mechanical drive. By measuring a single NV center, we eliminate the inhomogeneity in Ω that arises when the depth-dependent amplitude of the stress standing wave addresses a spatially distributed NV center ensemble. Although NV center ensembles provide advantages in fluorescence level and could be protected using mechanical CDD, we choose to study single NV centers because they provide

the cleanest possible system in which to study the underlying physics of mechanical CDD.

The HBAR used in these measurements consists of a 3 μm thick $\langle 002 \rangle$-oriented ZnO film sandwiched between a Ti/Pt (25 nm/200 nm) ground plane and an Al (250 nm) top contact. The piezo-electric ZnO film transduces stress waves into the diamond. The diamond then acts as an acoustic Fabry-Pérot cavity to create stress standing wave resonances. Fig. 6.2a shows a network analyzer measurement of the HBAR admittance (Y_{11}) plotted as a function of frequency. From this frequency comb, we selected the $\omega_{\text{mech}}/2\pi = 586$ MHz resonance mode, which has the combination of quality factor ($Q = 2700$ as calculated by the Q-circle method [45]) and on-resonance impedance ($18\ \Omega$) expected to produce the largest mechanical driving fields. This resonance suppresses driving field amplitude noise that is faster than $\omega_c = \frac{\omega_{\text{mech}}}{2Q} = 110 \times 2\pi$ kHz.

A microwave antenna patterned from Ti/Pt (25 nm/225 nm) on the diamond face opposite the ZnO transducer provides gigahertz frequency magnetic fields for conventional magnetic spin control. Fig. 6.2b shows a schematic depiction of the final device, and additional device details are provided in Sect. 6.3.3.

6.2.4 Dressed State Spectroscopy

We spectroscopically observe the emergence of the dressed states by first tuning the $m_I = +1$ ^{14}N sublevel of the $|+1\rangle \leftrightarrow |-1\rangle$ splitting into resonance with the $\omega_{\text{mech}}/2\pi = 586$ MHz mechanical mode [1]. We then perform dressed state spectroscopy using the concatenated pulse sequence in Fig. 6.2c. In a single instance of this sequence, the NV center is optically initialized into the $|0\rangle$ spin state at

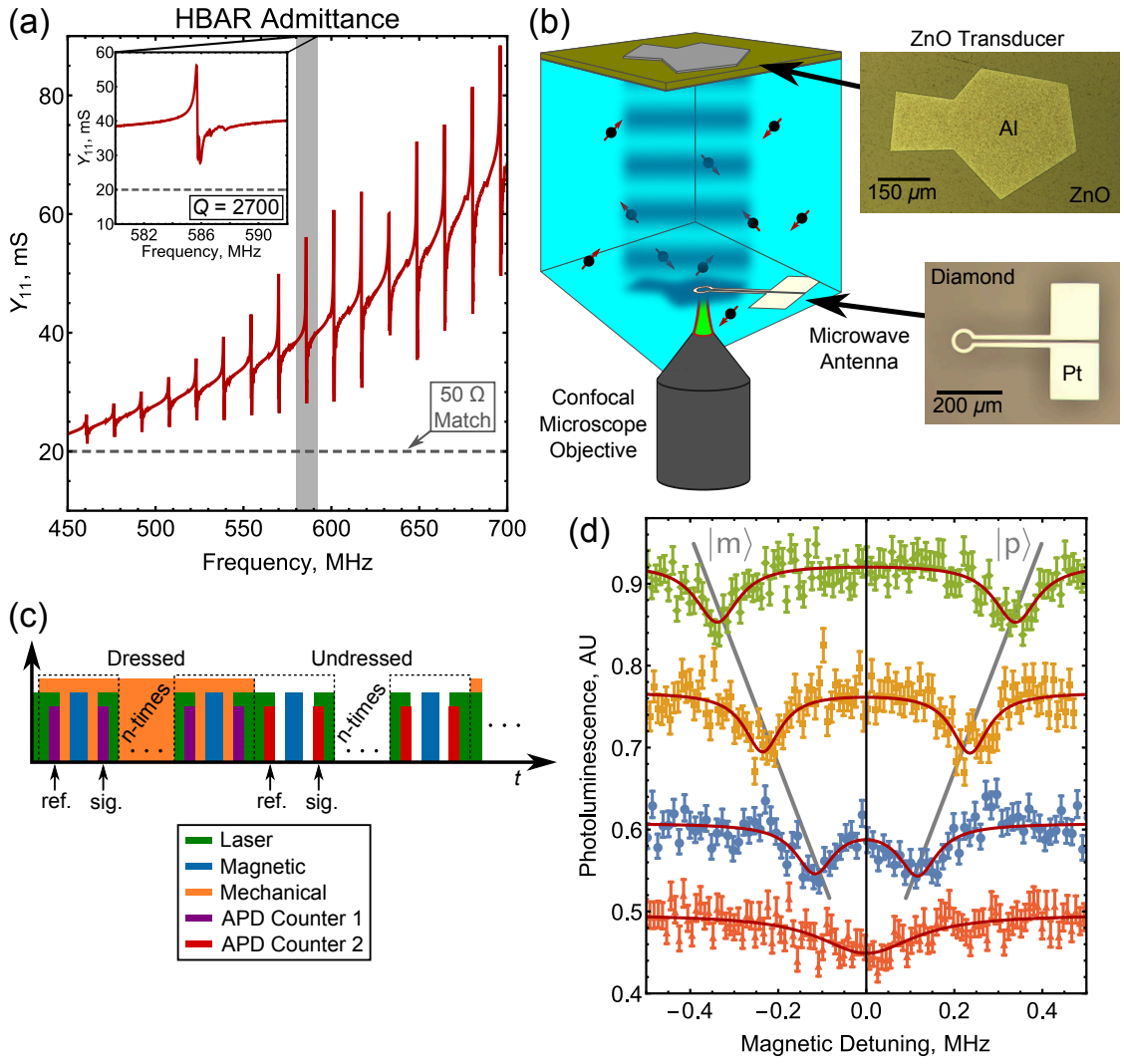

Figure 6.2: (a) Network analyzer measurement of the power admitted to the HBAR. The inset highlights the $\omega_{\text{mech}}/2\pi = 586$ MHz mode used in the measurements. (b) Device schematic. (c) Pulse sequence used for dressed state spectroscopy measurements. (d) Spectra of the $|0\rangle \leftrightarrow |m\rangle$ and $|0\rangle \leftrightarrow |p\rangle$ spin transitions within the dressed state basis. From bottom to top, the mechanical driving fields are $\Omega/2\pi = 0$ kHz, $\Omega/2\pi = 230 \pm 10$ kHz, $\Omega/2\pi = 470 \pm 8$ kHz, and $\Omega/2\pi = 670 \pm 10$ kHz.

which point a reference fluorescence measurement is made of the full-scale NV center photoluminescence. A magnetic π-pulse of strength $\Omega_{\text{mag}}/2\pi \sim 80$ kHz is then applied to drive a conditional spin rotation. Finally, fluorescence readout provides a quantitative measure of the spin population remaining in $|0\rangle$. We

interleave n instances of this pulse sequence executed in the dressed basis with n instances of this pulse sequence executed in the undressed basis. In a typical experiment $n \sim 10$, giving a total duty cycle time of ~ 280 μs and mechanical pulse length of ~ 140 μs. This pulse duration is much longer than the 1.5 μs ring time of our resonator, ensuring a fully rung up resonator. We differentiate between the dressed and undressed signal by routing the photon counts from our avalanche photodiode (APD) to separate data acquisition counters. This sequence is then repeated as a function of the magnetic detuning Δ_{mag} from the $|0\rangle \leftrightarrow |-1\rangle$ state splitting. The resulting spectra are shown in Fig. 6.2d for several values of Ω. The data have been fit using the procedure described in Sect. 6.3.4.

By simultaneously measuring $\omega_{0,-1}$; $\omega_{0,m}$; and $\omega_{0,p}$, we can feedback on b to precisely zero Δ using the relation $\frac{1}{2}(\omega_{0,m} + \omega_{0,p}) - \omega_{0,-1} = \frac{1}{2}\Delta$ (see Sect. 6.3.5 for a derivation). Operating at $\Delta = 0$ where $\frac{\partial \omega_{i,j}}{\partial \delta b}\Big|_{\Delta=0} \neq 0$ detunes Ω equally from each ^{13}C sublevel. This dresses both sublevels equivalently, preserving the full spin contrast of our measurements and maintaining the ^{13}C manifold as a degree of freedom. Alternatively, we could maximally protect one nuclear sublevel at the expense of the other by operating at $\Delta = \pm A_{\parallel}$ where $\frac{\partial \omega_{i,j}}{\partial \delta b}\Big|_{\Delta=\pm A_{\parallel}} = 0$ for one of the two sublevels. For an unpolarized ^{13}C spin, however, such a strategy would halve the measured spin contrast, limiting the utility of mechanical CDD.

6.2.5 Coherence of the $\{0, p\}$ Qubit

Next, we perform Ramsey measurements within the dressed basis to quantify the decoherence protection offered by mechanical CDD. We begin by examining the qubit derived from the $\{0, p\}$ subspace, which is minimally perturbed from the more familiar $\{0, -1\}$ qubit.

The pulse sequence used for these measurements is shown in Fig. 6.3a. After optically initializing the spin into $|0\rangle$, we apply a magnetic $\pi/2$-pulse of strength $\Omega_{\text{mag}}/2\pi = 700$ kHz to populate the $\{0, p\}$ subspace. Because $\Omega_{\text{mag}} > \omega_{m,p}$, the $\{0, m\}$ subspace is also populated. After a free evolution time τ, we apply a second magnetic $\pi/2$-pulse of the same strength to return the spin population to $|0\rangle$ where the signal is read out optically. To help visualize the decay, we advance the phase of the second $\pi/2$-pulse by $\omega_{\text{rot}}\tau$. Undressed Ramsey measurements are interleaved with the dressed measurements to reduce the average power load and provide a simultaneous measurement of the undressed dephasing time $T^*_{2,\{0,-1\}}$. We then repeat this sequence as a function of τ to generate a single CDD Ramsey curve.

Fig. 6.3b shows that a $\Omega/2\pi = 348 \pm 4$ kHz dressing field extends T_2^* from 5.9 ± 0.4 μs to 15.0 ± 0.9 μs. As described in Sect. 6.3.4, we approximate the decay of our CDD Ramsey signal with a Gaussian envelope. This is not strictly correct because $\omega_{0,p}$ varies non-linearly with δb. Nevertheless, when $\frac{\partial \omega_{i,j}}{\partial \delta b} \neq 0$ Gaussian decay reasonably approximates the dephasing over the range of Ω employed in this work and facilitates comparison with the undressed qubit coherence. Fig. 6.3c,d provide the Fourier spectrum of each measurement in Fig. 6.3b. Beating in the undressed Ramsey signal reveals a $|A_{\|}|/2\pi = 145 \pm 6$ kHz coupling to a nearby ^{13}C spin.

If the $\{0,p\}$ qubit coherence is limited by δb, then $T^*_{2,\{0,p\}}$ should scale linearly with Ω. However, as Fig. 6.3e shows, plotting $T^*_{2,\{0,p\}}$ as a function of Ω reveals an erratic distribution with a clustering around $T^*_{2,\{0,p\}} \sim 12$ μs. By monitoring the temperature of our sample over the course of several measurements as described in Sect. 6.3.6, we identified that this effect arises from ~ 0.25°C long-term temperature instabilities. Temperature enters the dressed NV center Hamiltonian through the zero-field splitting D, which varies at a rate of $\frac{dD}{dT} = -74 \times 2\pi$ kHz/°C [13, 57, 116] and contributes to $\omega_{0,p}$ and $\omega_{0,m}$. Gaussian thermal drift with a standard deviation of $\sigma_T = 0.25$°C will dephase the $\{0,p\}$ qubit in $T^*_{2,\{0,p\}} = \frac{\sqrt{2}}{\sigma_T dD/dT} = 12$ μs. Coherence times measured during periods of minimal thermal drift exceed this limit, indicating that mechanical CDD isolates the $\{0,p\}$ qubit from magnetic noise more successfully than Fig. 6.3e implies. Thermal instabilities take over as the dominant dephasing channel, however, which suggests mechanical CDD could offer an alternative thermometry protocol to thermal CPMG [57].

6.2.6 Coherence of the $\{m,p\}$ Qubit

With the $\{0,p\}$ qubit subdued by thermal fluctuations, we turn to the $\{m,p\}$ qubit to fully explore the efficacy of mechanical CDD at enhancing T_2^*. The Larmor frequency $\omega_{m,p}$ is independent of D, making the $\{m,p\}$ qubit insensitive to changes in temperature and thus capable of exceeding the ~ 12 μs thermally-limited coherence.

Fig. 6.4a shows the pulse sequence used to measure $T^*_{2,\{m,p\}}$. Here, magnetic double quantum (DQ) π-pulses of frequency $\omega_{DQ} = \frac{1}{2}(\omega_{0,m} + \omega_{0,p})$ and

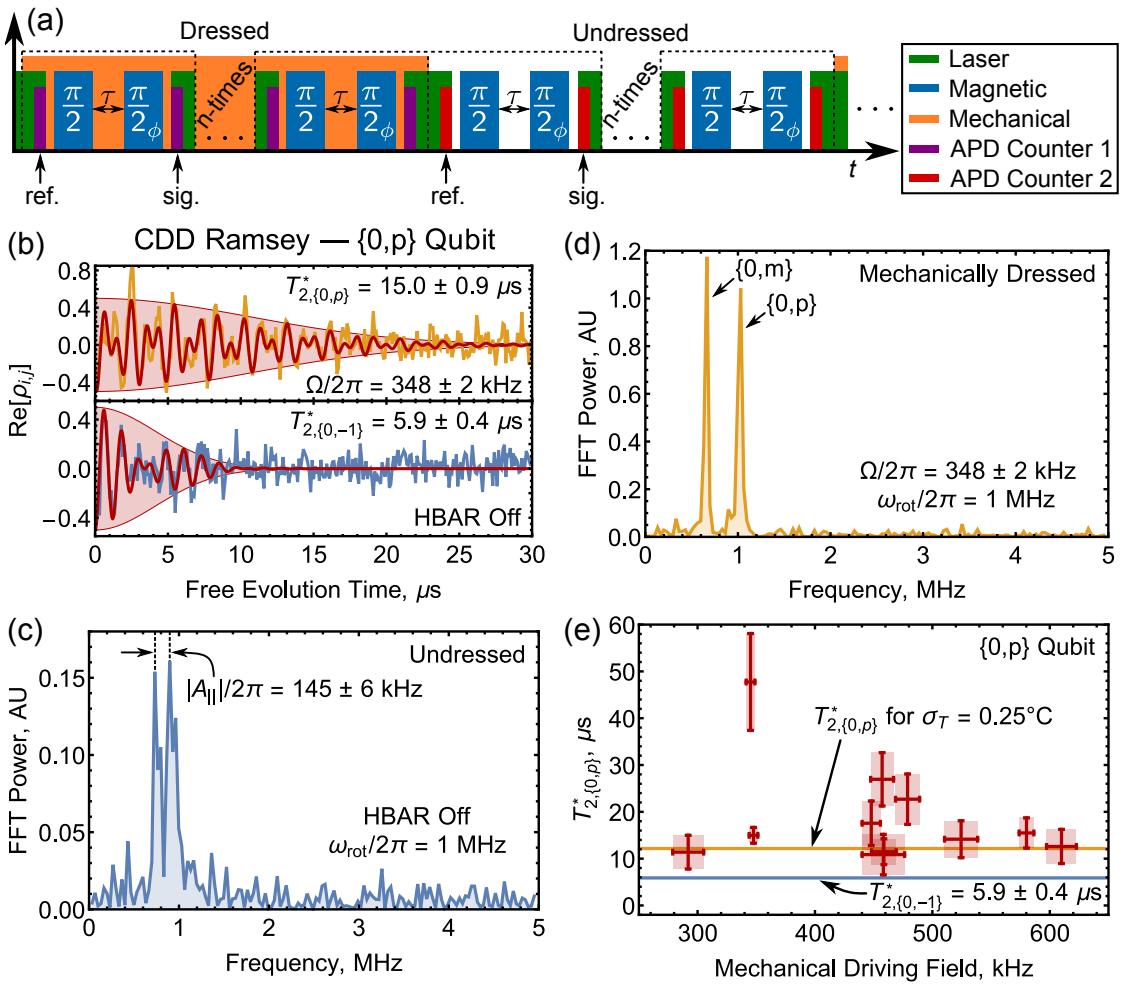

Figure 6.3: (a) Pulse sequence used for CDD Ramsey measurements of the $\{0, p\}$ qubit. (b) Ramsey measurements of the $\{0, p\}$ qubit protected by a $\Omega/2\pi = 348 \pm 2$ kHz mechanical dressing field and the $\{0, -1\}$ qubit. (c,d) Fourier spectra of the Ramsey data in (b). (e) Coherence time of the $\{0, p\}$ qubit plotted as a function of Ω. Error bars in (e) indicate 95% confidence intervals.

strength $\Omega_{\text{mag}}/2\pi = 1.51$ MHz address the $\{m, p\}$ subspace [86]. We interleave the dressed $\{m, p\}$ Ramsey measurements with undressed measurements that execute the same sequence of magnetic pulses. Because this pulse sequence amounts to a 2π rotation of the undressed $\{0, -1\}$ qubit, the average of this undressed trace $\langle P_{0,U} \rangle$ quantifies the NV center spin contrast.

During each measurement of $T^*_{2,\{m,p\}}$, we periodically measure Δ spectroscopically and feedback on b to maintain $\Delta \sim 0$. Interpolating linear drift between these measurements, we post-select to include only those data sets for which $\sigma_\Delta/2\pi < 60$ kHz and $|\langle\Delta\rangle|/2\pi < 35$ kHz. For these measurements, we studied a second NV center located nearby the NV center that was used in the $\{0,p\}$ qubit measurements. Both NV centers are quantitatively similar and have comparable $T^*_{2,\{0,-1\}}$ and $A_\parallel$.

Fig. 6.4b shows a typical CDD Ramsey measurement for the $\{m,p\}$ qubit that has been fit using the procedure described in Sect. 6.3.4. The undressed analog of the $\{m,p\}$ qubit is the $\{+1,-1\}$ qubit, and its $T^*_{2,\{+1,-1\}} = 2.7 \pm 0.1$ μs coherence time (measurement details in Sect. 6.3.7) is indicated by the shaded region in Fig. 6.4b. A $\Omega/2\pi = 581 \pm 2$ kHz dressing field extends the $\{m,p\}$ qubit coherence to $T^*_{2,\{m,p\}} = 15 \pm 1$ μs.

6.2.7 Decoherence Model

In order to quantitatively study how the measured spin protection scales with Ω, we examine quasi-static deviations in $\omega_{i,j}$ [117]. Because we work in a reference frame rotating at $\frac{1}{2}\omega_{\text{mech}}$, low frequency electric and strain field noise are averaged away, and—as noted above—the $\{m,p\}$ qubit is isolated from thermal noise. We thus examine dephasing from only two independent sources: δb and $\delta\Omega$.

Generically, first order deviations in the Larmor frequency $\omega_{i,j}$ take the form $\delta\omega_{i,j} = \alpha\delta x$ where α is a constant. If the fluctuation δx follows a Gaussian distribution with standard deviation σ_x, an expression for the associated dephasing

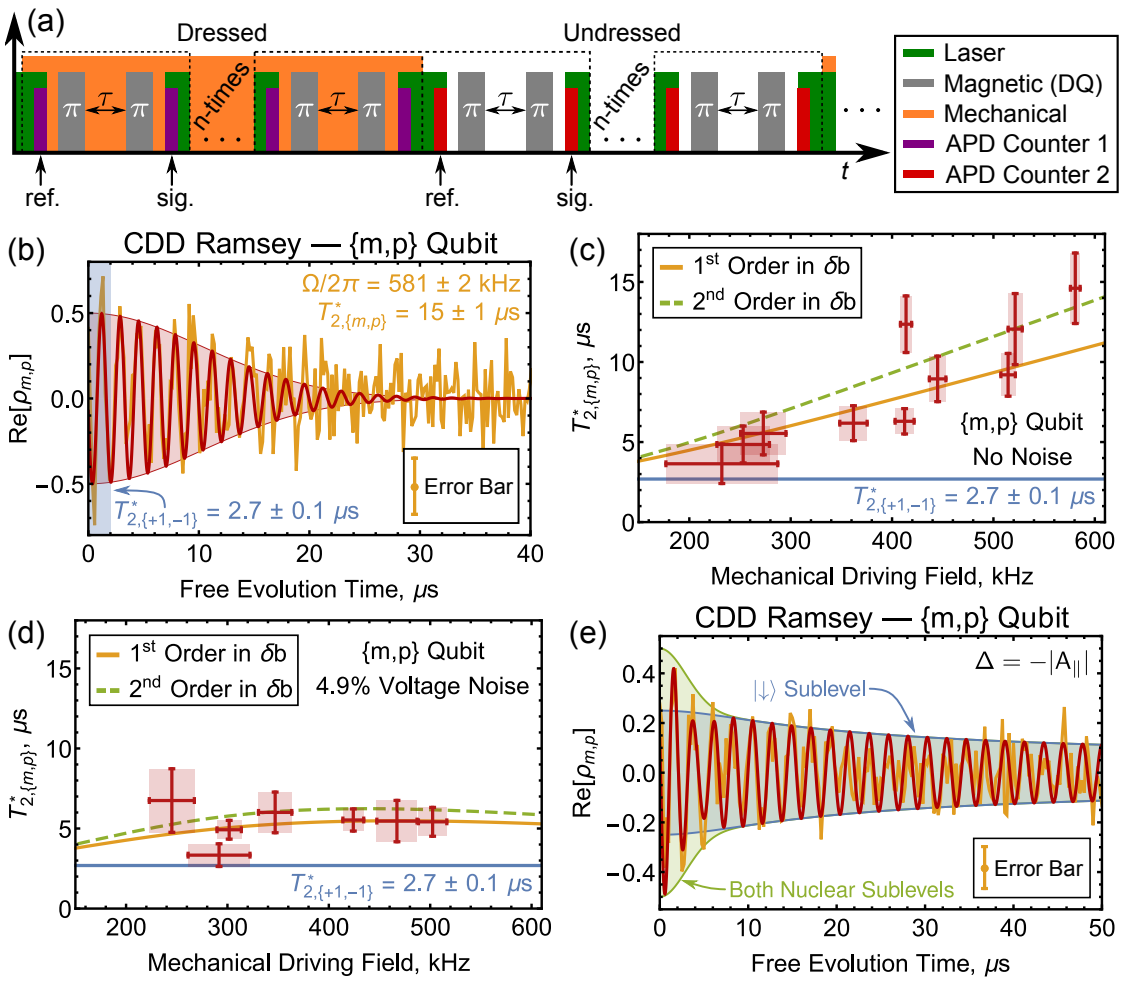

Figure 6.4: (a) Pulse sequence used for CDD Ramsey measurements of the $\{m, p\}$ qubit. (b) Ramsey measurements of the $\{m, p\}$ qubit protected by a $\Omega/2\pi = 581 \pm 2$ kHz mechanical dressing field. (c,d) Coherence time of the $\{m, p\}$ qubit plotted as a function of Ω for measurements where Ω was (c) actively stabilized and (d) given a Gaussian noise profile. Error bars in (c,d) indicate 95% confidence intervals. (e) Ramsey measurement of the $\{|m, \downarrow\rangle, |p, \downarrow\rangle\}$ qubit protected by a $\Omega/2\pi = 455.7 \pm 0.5$ kHz mechanical dressing field under the condition $\Delta = -|A_{\parallel}|$.

rate can be found by calculating the weighted average of a distribution of detuned, un-damped Ramsey signals:

$$\begin{aligned} \mathrm{Re}[\rho_{i,j}] &= \frac{1}{\sqrt{2\pi}\sigma_x} \int e^{-\frac{\delta x^2}{2\sigma_x^2}} \cos\left[(\omega_{i,j} + \alpha\delta x)\tau\right] \mathrm{d}\delta x \\ &= e^{-\frac{1}{2}(\alpha\sigma_x\tau)^2} \cos\left(\omega_{i,j}\tau\right). \end{aligned} \tag{6.1}$$

Comparing Eq. 6.1 with an ideal Ramsey signal given by $\mathrm{Re}[\rho_{i,j}] = e^{-\frac{\tau^2}{T_2^{*2}}}\cos(\omega_{i,j}\tau)$, we see that $T_2^* = \frac{\sqrt{2}}{\alpha\sigma_x}$ and therefore $\Gamma_x = \frac{2\pi}{T_2^*} = \sqrt{2}\pi\alpha\sigma_x$. The dephasing time from a collection of uncorrelated noise sources is given by $\frac{1}{T_2^*} = \frac{1}{2\pi}\sum\Gamma_i$.

For the high electronic purity CVD diamond studied in this work, the NV center undressed T_2^* is limited by dipolar coupling to nearby ^{13}C nuclear spins [118]. This coupling can be approximately modeled by a random time-varying magnetic field that follows a Gaussian distribution [87]. For magnetic field fluctuations experienced by the $\{0,-1\}$ qubit, we can then set $\alpha\delta x \to \gamma\delta b$ and arrive at the size of the ^{13}C spin bath $\gamma\sigma_b/2\pi = (\sqrt{2}\pi T_{2,\{0,-1\}}^*)^{-1} = 42\pm2$ kHz where $T_{2,\{0,-1\}}^* = 5.4\pm0.3$ μs for this NV center.

In the dressed basis, expanding $\omega_{m,p}$ to first order in δb gives

$$\delta\omega_{m,p;b} = \frac{2|A_\parallel|\gamma\delta b}{\sqrt{A_\parallel^2+\Omega^2}}, \tag{6.2}$$

from which we find $\Gamma_b = 2\sqrt{2}\kappa|A_\parallel|/T_{2,\{0,-1\}}^*$ where $\frac{1}{\kappa} = \frac{1}{\sqrt{2}\pi}\sqrt{A_\parallel^2+\Omega^2}$. Similarly, expanding $\omega_{m,p}$ to first order in $\delta\Omega$ gives

$$\delta\omega_{m,p;\Omega} = \frac{\Omega\delta\Omega}{\sqrt{A_\parallel^2+\Omega^2}}, \tag{6.3}$$

from which we find $\Gamma_\Omega = \kappa\Omega\sigma_\Omega$.

Our measurements of $T_{2,\{m,p\}}^*$ employ a feedback protocol to level the power supplied to the HBAR and reduce $\delta\Omega$ to $\sim 0.03\%$ of Ω. For the range of Ω accessed here, this level of stability makes $\Gamma_\Omega \ll \Gamma_b$, and we can ignore the effects of $\delta\Omega$. To first order in δb, the dephasing time of the $\{m,p\}$ qubit is then given by $T_{2,\{m,p\}}^* = \frac{2\pi}{\Gamma_b}$.

Fig. 6.4c plots $T^*_{2,\{m,p\}}$ as a function of Ω. The measurements used to obtain each data point are presented in Sect. 6.3.8, and we attribute scatter in the data mainly to deviations from the $\Delta = 0$ condition. For $\Omega \lesssim 10\gamma\sigma_b = (420 \pm 20) \times 2\pi$ kHz, the first order expansion in δb correctly predicts $T^*_{2,\{m,p\}}$. However, as Ω increases and $\frac{\partial \omega_{m,p}}{\partial \delta b}\Big|_{\Delta=0}$ diminishes, the measured coherence times begin to surpass the predictions of the first order model. To account for this, we extend our model to second order in δb as detailed in Sect. 6.3.9 and numerically solve the resulting non-Gaussian decoherence envelope for the $\frac{1}{e}$ decay time [117]. As seen in Fig. 6.4c, the model correct to second order in δb more accurately predicts $T^*_{2,\{m,p\}}$ for $\Omega \gtrsim 10\gamma\sigma_b$. This suggests that for these higher dressing fields, the $\{m, p\}$ qubit coherence remains limited by δb. The cw power handling capabilities of our device prohibited measurements at larger Ω, but these results indicate that $T^*_{2,\{m,p\}}$ would continue to increase with Ω.

To test the predictive capabilities of our model, we intentionally increase $\delta\Omega$ to the point where Γ_Ω becomes the dominant dephasing channel. To do this quantitatively, we monitor the voltage reflected from the HBAR V_R, which scales linearly with Ω. We then periodically randomize the power supplied to the HBAR to give V_R a Gaussian distribution with standard deviation $\sigma_V = \eta\langle V_R\rangle$ where η is a constant. This yields a Gaussian distribution of Ω with a standard deviation $\sigma_\Omega = (\langle\Omega\rangle + \alpha)\eta$ where $\alpha/2\pi = -133 \pm 7$ kHz is a constant related to our measurement of V_R as described in Sect. 6.3.10. The dephasing time is then given by $T^*_{2,\{m,p\}} = \frac{2\pi}{\Gamma_b+\Gamma_\Omega}$.

Fig. 6.4d shows the measured and predicted $T^*_{2,\{m,p\}}$ for $\eta = 4.9 \pm 0.2\%$. Once again, the measurements used to obtain each data point are presented in Sect. 6.3.8. Decoherence in these measurements is dominated by $\delta\Omega$. Therefore,

the model accurately predicts $T^*_{2,\{m,p\}}$ whether Γ_b is correct to first or second order in δb. Power leveling can effectively zero $\delta\Omega$ over the range of Ω measured here, but these results suggest that in a more efficient device where a larger Ω is attainable, amplitude noise would eventually limit the protection that mechanical CDD offers, even in the power-leveled case.

6.2.8 Protecting a Single ^{13}C Sublevel

We conclude by maximally protecting the $|\downarrow\rangle$ ^{13}C sublevel of the $\{m,p\}$ qubit at the expense of the $|\uparrow\rangle$ sublevel. By setting $\Delta = -|A_\parallel|$ where $|A_\parallel|/2\pi = 150 \pm 4$ kHz for this NV center, we establish the condition $\frac{\partial\omega_{m,p}}{\partial\delta b}\Big|_{\Delta=-|A_\parallel|} = 0$ for the $|\downarrow\rangle$ sublevel. As described in Sect. 6.3.9, to second order in δb the coherence of this sublevel is then described by [117]

$$\mathrm{Re}[\rho_{m,p;\downarrow}] = \frac{\langle P_{0,U}\rangle}{4}\sqrt{\frac{\Omega}{\sqrt{\Omega^2 + (2\gamma\sigma_b)^4\tau^2}}}\cos\left[\Omega\tau + \phi\right]. \tag{6.4}$$

The result of this measurement for a $\Omega/2\pi = 455.7 \pm 0.5$ kHz dressing field is shown in Fig. 6.4e. As detailed in Sect. 6.3.9, the data have been fit to a sum of Eq. 6.4, Gaussian decay of the $|\uparrow\rangle$ coherence, and a constant background c. Only the parameters Ω, ϕ, c, and $T^*_{2,\uparrow}$ were allowed to vary as free parameters in our fitting procedure.

As the shaded regions of Fig. 6.4e highlight, the $|\uparrow\rangle$ sublevel rapidly dephases in $T^*_{2,\uparrow} = 4.1 \pm 0.7$ μs, while the coherence of the $|\downarrow\rangle$ sublevel is strongly protected, persisting beyond the 50 μs time frame of the measurement. This marks a $\gtrsim 19$-fold increase in $T^*_{2,\{m,p\}}$ over the bare $T^*_{2,\{+1,-1\}}$. We note that infidelities in our DQ pulses reduce the spin contrast within this subspace, limiting

the utility of protecting only one sublevel in an unpolarized hyperfine manifold. Higher fidelity pulsing protocols or more efficient photon collection [119] could increase the signal-to-noise ratio, which would make the lengthy coherence of the $\{|m,\downarrow\rangle, |p,\downarrow\rangle\}$ qubit a valuable asset.

6.2.9 Conclusions

In summary, we have experimentally demonstrated and theoretically analyzed the performance of mechanical CDD for decoupling an NV center spin qubit. We have shown that ac lattice strain can dress the spin states of an NV center and that the eigenstates of this dressed basis have robust coherence even in the presence of magnetic field fluctuations. We prolong T_2^* of a thermally isolated qubit from 2.7 ± 0.1 μs to 15 ± 1 μs with a $\Omega/2\pi = 581 \pm 2$ kHz mechanical dressing field and show that T_2^* can be extended even further by either engineering more efficient devices or choosing to protect only a single ^{13}C hyperfine sublevel. Mechanical CDD preserves the $|0\rangle$ state and therefore does not require the NV center to be adiabatically dressed and undressed before and after each measurement. Moreover, the thermally sensitive $\{0, p\}$ and $\{0, m\}$ qubits maintain the gigahertz-scale Larmor frequency of their undressed analogs, providing rapid signal accumulation for a dressed state thermometer. Mechanically dressed qubits thus offer a promising option in the continuing development of NV center technology.

6.3 Supplementary Information

6.3.1 Mechanical Rabi Driving

The mechanically driven Rabi oscillations depicted in Fig. 6.1a were measured using the pulse sequence shown in Fig. 6.5. As described in detail in Ref. [2], the relatively high Q of our mechanical resonance makes it difficult to perform a traditional pulsed Rabi measurement. Instead, a pair of magnetic π-pulses resonant with the $|0\rangle \leftrightarrow |-1\rangle$ transition and separated by a fixed time τ_{mag} is swept through a fixed-length mechanical pulse. The mechanical pulse drives the $|+1\rangle \leftrightarrow |-1\rangle$ spin transition, and the duration of this interaction is set by the area of the mechanical pulse enclosed between the two π-pulses. By knowing the shape of the mechanical pulse and tracking the delay τ_0 of the magnetic pulse pair, we convert this enclosed area to effective square-pulse units or an "effective mechanical pulse length." Because the mechanical resonator is pulsed in this experiment, we are able to achieve a larger driving field than in the continuous dynamical decoupling (CDD) Ramsey measurements where the mechanical resonator operates in cw mode.

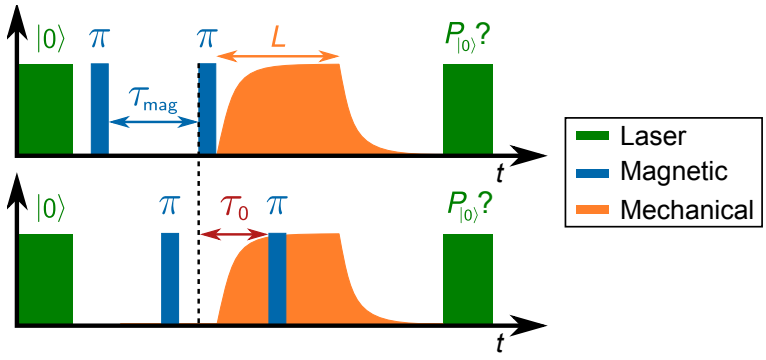

Figure 6.5: Pulse sequence used to measure mechanically driven Rabi oscillations.

6.3.2 Mechanically Dressed Hamiltonian

As mentioned in Sect. 6.2.2, we work within the $m_I = +1$ sublevel of the ^{14}N hyperfine manifold. We consider both a static magnetic field b that is aligned along the NV center symmetry axis and subject to fluctuations δb and a mechanical driving field Ω that is subject to amplitude fluctuations $\delta\Omega$. In the $\{+1, 0, -1\} \otimes \{(m_I =) + \frac{1}{2}, -\frac{1}{2}\}$ Zeeman basis, a nearby ^{13}C nuclear spin weakly couples to an NV center electronic spin through the hyperfine perturbation $H_C = A_\parallel S_z I_z$ where S_z and I_z are the spin-1 and spin-$\frac{1}{2}$ Pauli matrices, respectively, and $A_\parallel$ is the coupling strength [70]. An NV center electronic spin then obeys the Hamiltonian

$$H_{LF} = \begin{pmatrix} \gamma b_\Sigma + \frac{1}{2}A_\parallel & 0 & 0 & 0 & \Omega_\Sigma \cos(\omega_{\text{mech}} t) & 0 \\ 0 & \gamma b_\Sigma - \frac{1}{2}A_\parallel & 0 & 0 & 0 & \Omega_\Sigma \cos(\omega_{\text{mech}} t) \\ 0 & 0 & -D & 0 & 0 & 0 \\ 0 & 0 & 0 & -D & 0 & 0 \\ \Omega_\Sigma \cos(\omega_{\text{mech}} t) & 0 & 0 & 0 & -\gamma b_\Sigma - \frac{1}{2}A_\parallel & 0 \\ 0 & \Omega_\Sigma \cos(\omega_{\text{mech}} t) & 0 & 0 & 0 & -\gamma b_\Sigma + \frac{1}{2}A_\parallel \end{pmatrix} \tag{6.5}$$

where $b_\Sigma = b + \delta b$, $\Omega_\Sigma = \Omega + \delta\Omega$, other parameters are as previously defined, and we have not included a magnetic driving field. Applying the rotating wave approximation and transforming into the reference frame rotating at $\frac{1}{2}\omega_{\text{mech}} =$

$\frac{1}{2}(2\gamma b + \Delta)$ gives the Hamiltonian in the rotating frame

$$H_{RF} = \begin{pmatrix} \gamma b_\Sigma + \frac{1}{2}(\Delta + A_\parallel) & 0 & 0 & 0 & \frac{1}{2}\Omega_\Sigma & 0 \\ 0 & \gamma b_\Sigma + \frac{1}{2}(\Delta + A_\parallel) & 0 & 0 & 0 & \frac{1}{2}\Omega_\Sigma \\ 0 & 0 & -D & 0 & 0 & 0 \\ 0 & 0 & 0 & -D & 0 & 0 \\ \frac{1}{2}\Omega_\Sigma & 0 & 0 & 0 & -\gamma b_\Sigma - \frac{1}{2}(\Delta + A_\parallel) & 0 \\ 0 & \frac{1}{2}\Omega_\Sigma & 0 & 0 & 0 & -\gamma b_\Sigma - \frac{1}{2}(\Delta - A_\parallel) \end{pmatrix}. \tag{6.6}$$

Diagonalizing H_{RF} gives the mechanically dressed Hamiltonian whose energies are quoted in Sect. 6.2.2:

$$H_D = \begin{pmatrix} -D & 0 & 0 & 0 & 0 & 0 \\ 0 & -D & 0 & 0 & 0 & 0 \\ 0 & 0 & -\frac{1}{2}\sqrt{\Omega_\Sigma^2 + \xi_-^2} & 0 & 0 & 0 \\ 0 & 0 & 0 & \frac{1}{2}\sqrt{\Omega_\Sigma^2 + \xi_-^2} & 0 & 0 \\ 0 & 0 & 0 & 0 & -\frac{1}{2}\sqrt{\Omega_\Sigma^2 + \xi_+^2} & 0 \\ 0 & 0 & 0 & 0 & 0 & \frac{1}{2}\sqrt{\Omega_\Sigma^2 + \xi_+^2} \end{pmatrix} \tag{6.7}$$

where $\xi_\pm = \Delta + 2\gamma\delta b \pm A_\parallel$. In the limit $\Omega_\Sigma = 0$, H_D reduces to the undressed Zeeman Hamiltonian in the rotating frame.

6.3.3 Additional Device Details

Our device was fabricated with an in-house procedure designed to create high Q resonances with good impedance matches to a $50\,\Omega$ line. For a fixed input power to the device, a resonance with a higher Q and a better impedance match will

produce a larger amplitude stress standing wave and thus a larger mechanical driving field. This scaling can be approximated by the expression [1]

$$\frac{\Omega_1}{\Omega_2} = \frac{Q_1}{Q_2} \times \frac{Z_1\sqrt{50\ \Omega + Z_2}}{Z_2\sqrt{50\ \Omega + Z_1}} \tag{6.8}$$

where Ω_i is the mechanical driving field, Z_i is the impedance, and Q_i is the quality factor of the i^{th} resonance. Using this expression, we selected the $\omega_{\text{mech}}/2\pi = 586$ MHz resonance mode, which was expected to give the largest mechanical driving fields.

6.3.4 Fitting Functions

Dressed State Spectroscopy

The dressed state spectra displayed in Fig. 6.2d are fit to the sum of two Lorentzians

$$\begin{aligned} P_D = c_D &- \frac{a_{D,p}}{\left(\omega - \frac{1}{2}\sqrt{\Delta^2 + \Omega^2} - \frac{1}{2}\Delta - \omega_{0,-1}\right)^2 + \left(\frac{1}{2}\Gamma_D\right)^2} \\ &- \frac{a_{D,m}}{\left(\omega + \frac{1}{2}\sqrt{\Delta^2 + \Omega^2} - \frac{1}{2}\Delta - \omega_{0,-1}\right)^2 + \left(\frac{1}{2}\Gamma_D\right)^2} \end{aligned} \tag{6.9}$$

where P_D is the measured photoluminescence, c_D is a constant background, $\omega_{0,-1}$ is the undressed $|0\rangle \leftrightarrow |-1\rangle$ spin state splitting, Δ is the mechanical detuning, Ω is the mechanical driving field, $a_{D,i}$ accounts for the depth of the i^{th} spectral peak, and Γ_D measures the full width at half maximum of the dressed spectral peaks. The undressed signal accumulated from the interleaved measurements is simultaneously fit to the Lorentzian

$$P_U = c_U - \frac{a_U}{(\omega - \omega_{0,-1})^2 + \left(\frac{1}{2}\Gamma_U\right)^2}. \tag{6.10}$$

We then subtract $\omega_{0,-1}$ from the x-axis to plot photoluminescence as a function of Δ_{mag}.

Undressed Ramsey Measurements

We fit the undressed Ramsey data in Fig. 6.3b and Fig. 6.6a to the expression

$$\begin{aligned} P_{\{0,-1\}} = c - \frac{a}{4} e^{-\frac{\tau^2}{T_2^{*2}}} \Bigg\{ & \cos\left[\left(\omega_{\text{rot}} + \Delta_{\text{mag}} + \frac{1}{2}A_{\parallel}\right)\tau\right] \\ & + \cos\left[\left(\omega_{\text{rot}} + \Delta_{\text{mag}} - \frac{1}{2}A_{\parallel}\right)\tau\right] \Bigg\} \end{aligned} \tag{6.11}$$

where $P_{\{0,-1\}}$ is the measured photoluminescence, c is a constant background, a is an overall amplitude that accounts for deviations from perfect spin contrast, Δ_{mag} is the magnetic detuning, and $A_{\parallel}$ quantifies coupling to an unpolarized ^{13}C nuclear spin. Of these values, c, a, T_2^*, Δ_{mag}, and $A_{\parallel}$ are free parameters in our fit. We use the values of a and c returned from the fits to rescale the y-axes in terms of the qubit coherence Re$[\rho_{0,-1}]$.

CDD Ramsey Measurements: $\{0, p\}$ Qubit

To fit the CDD Ramsey data for the $\{0, p\}$ qubit, we zero the magnetic detuning midway between the ^{13}C sublevels. Assuming $\Delta = 0$, our $\{0, p\}$ CDD Ramsey signal is then described by the expression

$$\begin{aligned} P_{\{0,p\}} = c + \frac{1}{4} e^{-\frac{\tau^2}{T_2^{*2}}} \Bigg\{ & a_p \cos\left[\left(\Delta_{\text{mag}} + \omega_{\text{rot}}\right)\tau + \phi\right] \\ & + a_m \cos\left[\left(\Delta_{\text{mag}} + \omega_{\text{rot}} + \sqrt{\Omega^2 + A_{\parallel}^2}\right)\tau + \phi\right] \Bigg\} \end{aligned} \tag{6.12}$$

where a_p is the spin contrast for the $\{0, p\}$ qubit, a_m is the spin contrast for the $\{0, m\}$ qubit, ϕ is a constant phase offset, and the other parameters are as defined

above. The undressed Ramsey data fixes the value of $A_\parallel$, and we vary c, a_i, ϕ, Ω, and Δ_{mag} as free parameters in our fitting procedure. We use the values of a_m, a_p, and c returned from the fit to rescale the y-axis of Fig. 6.3b in terms of Re$[\rho_{0,p}]$.

CDD Ramsey Measurements: $\{m, p\}$ Qubit

Fixing $\Delta = 0$, we fit the $\{m, p\}$ qubit data shown in Fig. 6.4b, Fig. 6.7, and Fig. 6.8 to the expression

$$P_{\{m,p\}} = c + \frac{\langle P_{0,U}\rangle}{2} e^{-\frac{\tau^2}{T_2^{*2}}} \cos\left[\tau\sqrt{A_\parallel^2 + \Omega^2} + \phi\right] \tag{6.13}$$

where the parameters are as defined above. We allow c, T_2^*, Ω, and ϕ to vary as free parameters in our fitting procedure, and we use $\langle P_{0,U}\rangle$ and the value of c returned from the fits to rescale the y-axes of our plots in terms of Re$[\rho_{m,p}]$.

6.3.5 Expression for the Mechanical Detuning

In our spectroscopy measurements, we use the relation $\frac{1}{2}(\omega_{0,m} + \omega_{0,p}) - \omega_{0,-1} = \frac{1}{2}\Delta$ as a means of zeroing the mechanical detuning. To derive this expression, we begin in the $\{+1, 0, -1\}$ basis with the Hamiltonian for an NV center subject to both a mechanical driving field and a magnetic driving field resonant with the $|0\rangle \leftrightarrow |-1\rangle$ transition. In the doubly rotating reference frame, this can be written

$$H_{RF} = \begin{pmatrix} \frac{1}{2}\Delta & 0 & \frac{1}{2}\Omega \\ 0 & -D - \Delta_{\text{mag}} & \frac{1}{2}\Omega_{\text{mag}} \\ \frac{1}{2}\Omega & \frac{1}{2}\Omega_{\text{mag}} & -\frac{1}{2}\Delta \end{pmatrix} \tag{6.14}$$

where $\Delta_{\text{mag}} = -\frac{1}{2}\Delta$ for resonant magnetic driving, and Ω_{mag} is far enough detuned from the $|+1\rangle \leftrightarrow |0\rangle$ transition that we can ignore the $\langle +1| H_{RF} |0\rangle$ matrix element.

For the undressed case ($\Omega = 0$, $\Delta = 0$), the energy of the $|0\rangle \leftrightarrow |-1\rangle$ splitting in this reference frame is $\omega_{0,-1} = D$ where we define $\hbar = 1$. With $\Omega \neq 0$, calculating the eigenvalues of Eq. 6.14 to first order in $\frac{\Omega_{\text{mag}}}{\Omega}$ gives energies $\omega_{0,p} = D + \frac{1}{2}(\Delta + \sqrt{\Delta^2 + \Omega^2})$ and $\omega_{0,m} = D + \frac{1}{2}(\Delta - \sqrt{\Delta^2 + \Omega^2})$. From this we arrive at the desired expression $\frac{1}{2}(\omega_{0,m} + \omega_{0,p}) - \omega_{0,-1} = \frac{1}{2}\Delta$. The same expression is obtained when the ^{13}C coupling is included.

6.3.6 Thermal Stability

As mentioned in Sect. 6.2.6, we intersperse spectral measurements within CDD Ramsey measurements of the $\{m, p\}$ qubit. This allows us to feedback on b and maintain a relatively constant Δ, but these measurements also quantify the thermal drift over the course of the measurement. A histogram of Δ extracted from fitting these spectra to Eq. 6.9 quantifies drift in the magnetic bias field as $\sigma_\Delta = 2\gamma\sigma_{\text{bias}}$ where σ_Δ and σ_{bias} are the standard deviations of the Δ histogram and of the magnetic bias field, respectively. A histogram of $\omega_{0,-1}$, however, provides information about both the magnetic bias field drift and the thermal drift according to

$$\sigma_{0,-1} = \sqrt{(\gamma\sigma_{\text{bias}})^2 + \left(\frac{dD}{dT}\sigma_T\right)^2} \tag{6.15}$$

where σ_T is the standard deviation of normally distributed thermal drift, $\frac{dD}{dT} = -74 \times 2\pi$ kHz/°C is the temperature dependence of D [13, 57, 116], and $\sigma_{0,-1}$ is the standard deviation of the $\omega_{0,-1}$ histogram. The average of σ_T for the power-

leveled data that satisfy our post-selection criteria is 0.25 ± 0.03°C. Thermal drift on a similar scale can be expected for the $\{0, p\}$ qubit measurements.

Applying the findings of Sect. 6.2.7 to thermal dephasing of the $\{0, p\}$ qubit, we find that for Gaussian thermal fluctuations, $\alpha \delta x \rightarrow \frac{\mathrm{d}D}{\mathrm{d}T} \delta T$. Fluctuations on the scale of σ_T would thus limit the $\{0, p\}$ qubit coherence time to $T^*_{2,\{0,p\}} = \frac{\sqrt{2}}{\sigma_T dD/dT} = 12 \pm 1$ μs as quoted in Sect. 6.2.5.

6.3.7 Coherence of the $\{+1, -1\}$ Qubit

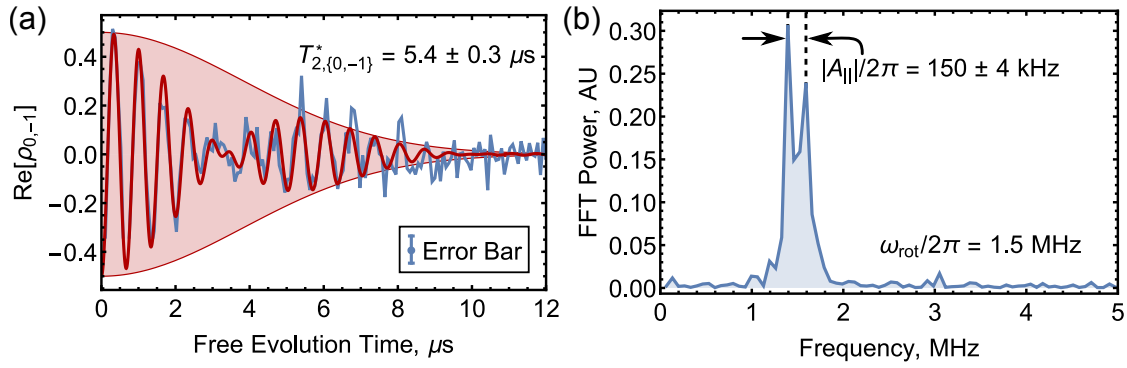

Figure 6.6: (a) Ramsey measurement of the undressed $\{0, -1\}$ qubit for the NV center used in the $\{m, p\}$ qubit measurements. (b) Fourier spectrum of (a).

We compare the coherence of the $\{m, p\}$ qubit to that of the undressed $\{+1, -1\}$ qubit because in each of these qubits both component states are sensitive to magnetic field fluctuations. Directly measuring the dephasing time of the $\{+1, -1\}$ qubit at nonzero field with high precision is a non-trivial task because the measurement becomes sensitive to double quantum pulse infidelities. Instead, we measure T^*_2 of the undressed $\{0, -1\}$ qubit (Fig. 6.6) and rely on the fact that for Gaussian magnetic field fluctuations $T^*_{2,\{+1,-1\}} = \frac{1}{2} T^*_{2,\{0,-1\}}$. This gives $T^*_{2,\{+1,-1\}} = 2.7 \pm 0.1$ μs as quoted in Sect. 6.2.6. This same undressed Ram-

sey measurement also quantifies $|A_{\|}|/2\pi = 150 \pm 4$ kHz and $\sigma_b = 2.4 \pm 0.1$ mG for this NV center.

6.3.8 $\{m, p\}$ Qubit CDD Ramsey Data

The data and fits from the measurements of $T^*_{2,\{m,p\}}$ shown in Fig. 6.4c,d are displayed in Fig. 6.7 and Fig. 6.8, respectively.

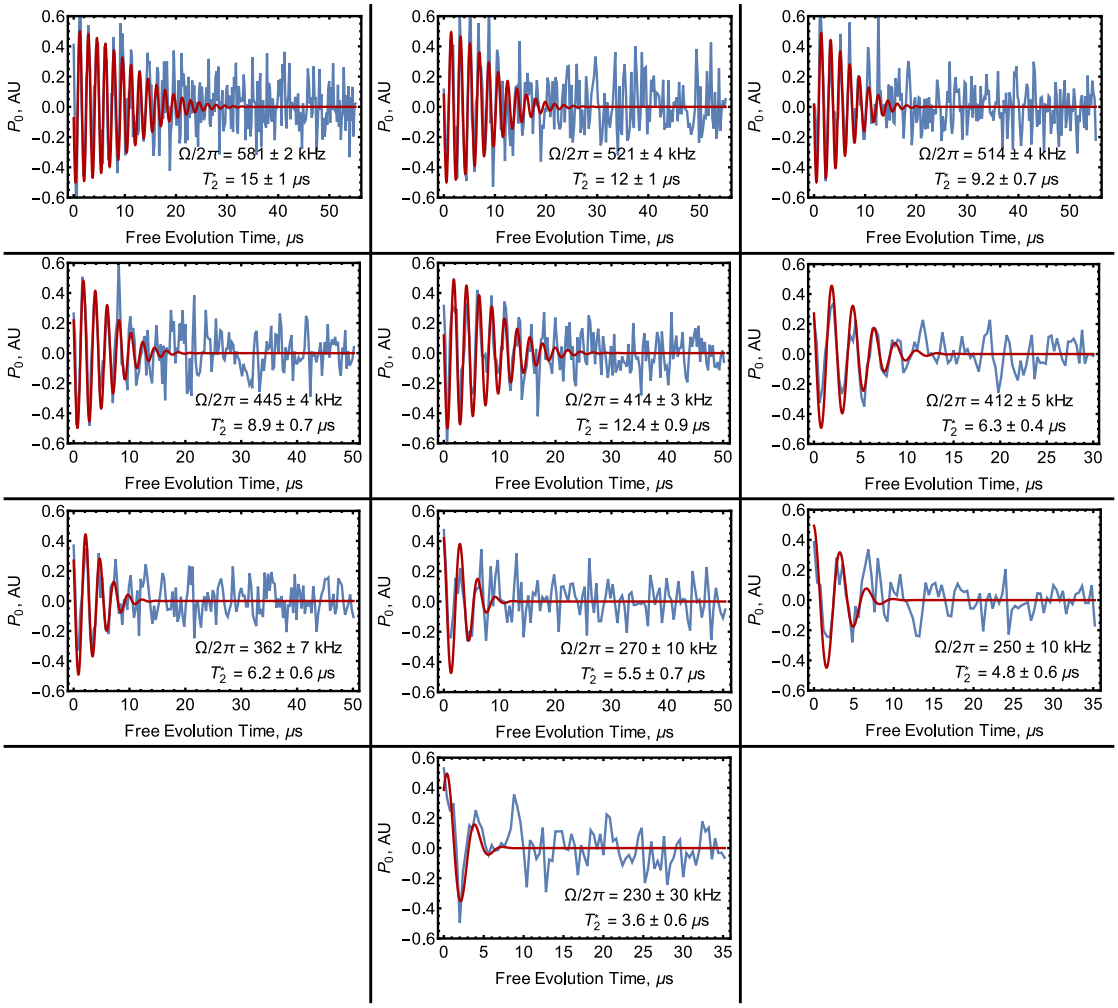

Figure 6.7: Data and fits for CDD Ramsey measurements of the $\{m, p\}$ qubit when Ω was actively stabilized.

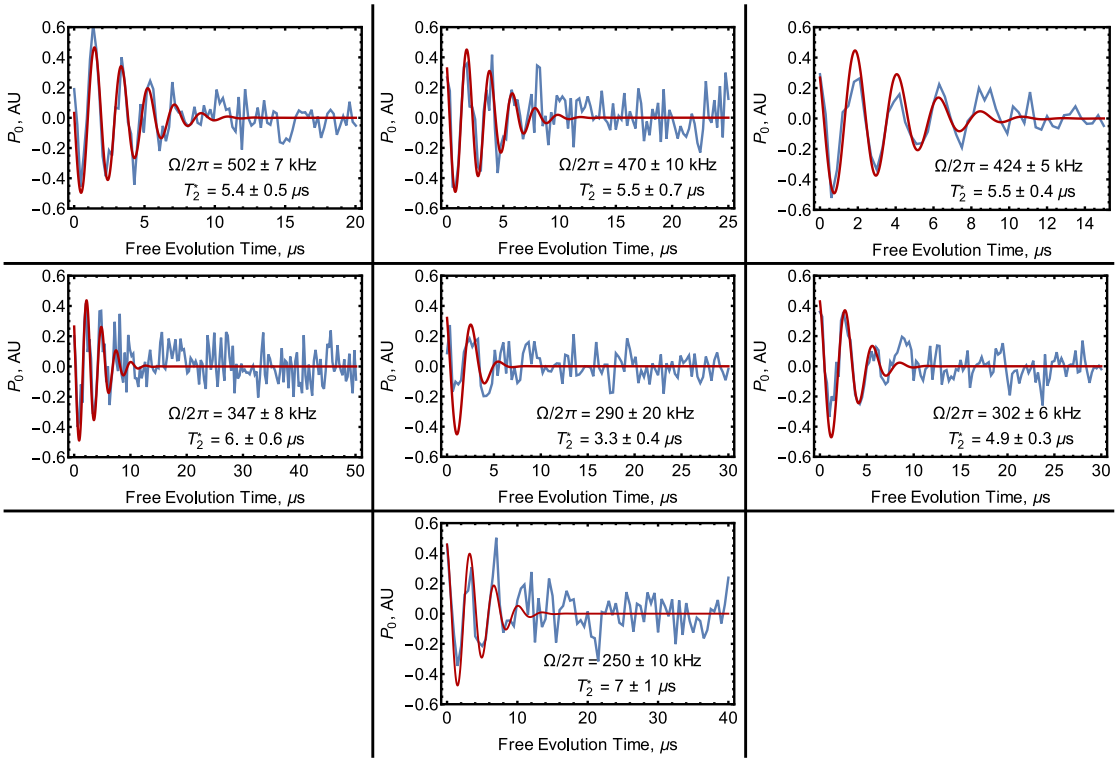

Figure 6.8: Data and fits for CDD Ramsey measurements of the $\{m, p\}$ qubit when Ω was given a Gaussian noise profile.

6.3.9 Second Order Magnetic Field Fluctuations

The decay envelope of a Ramsey measurement is given by the expression $f(\tau, \Omega, \sigma_b, A_\parallel) = |\langle e^{i\delta\phi}\rangle|$ where $\delta\phi$ is the random phase accumulated in a given duty cycle of the measurement [117]. For the $\{m, p\}$ qubit in the case when $\Delta = 0$ and $\delta\Omega = 0$, the Larmor frequency is $\omega_{m,p} = \sqrt{\Omega^2 + (A_\parallel + 2\gamma b)^2}$. To second order in δb, fluctuations in $\omega_{m,p}$ from magnetic field fluctuations are then given by

$$\begin{aligned}\delta\omega_{m,p} &= \frac{\partial\omega_{m,p}}{\partial b}\Big|_{\delta b=0}\delta b + \frac{\partial^2\omega_{m,p}}{\partial b^2}\Big|_{\delta b=0}\frac{\delta b^2}{2} + O(\delta b^3) \\ &= \frac{2\gamma\delta b(A_\parallel^3 + A_\parallel\Omega^2 + \gamma\delta b\Omega^2)}{(A_\parallel^2 + \Omega^2)^{3/2}}\end{aligned}, \tag{6.16}$$

and the random phase accumulated is $\delta\phi = \delta\omega_{m,p}\tau$. By averaging this phase over a Gaussian distribution of magnetic field fluctuations, we find an expression for the decoherence envelope

$$\begin{aligned} f(\tau, \Omega, \sigma_b, A_\parallel) &= \left| \frac{1}{\sqrt{2\pi}\sigma_b} \int_{-\infty}^{\infty} e^{i\delta\omega_{m,p}\tau} e^{-\frac{\delta b^2}{2\sigma_b^2}} \mathrm{d}\delta b \right| \\ &= \sqrt{\beta} e^{-\frac{2(\gamma\sigma_b A_\parallel \beta\tau)^2}{A_\parallel^2 + \Omega^2}} \end{aligned} \tag{6.17}$$

where

$$\beta(\tau, \Omega, \sigma_b, A_\parallel) \equiv \sqrt{\frac{(A_\parallel^2 + \Omega^2)^3}{(A_\parallel^2 + \Omega^2)^3 + (2\gamma\sigma_b\Omega)^4\tau^2}}. \tag{6.18}$$

To produce the second order model curves in Fig. 6.3b,c, we numerically solve this expression for the value of τ such that $f(\tau, \Omega, \sigma_b, A_\parallel) = \frac{1}{e}$.

When $\Delta = -|A_\parallel|$, the two ^{13}C sublevels follow different decay envelopes that can be computed by setting $A_\parallel \to 0$ and $A_\parallel \to 2A_\parallel$ in Eq. 6.17. In the former case, $f(\tau, \Omega, \sigma_b, 0)$ reduces to

$$h(\tau, \Omega, \sigma_b) = \sqrt{\frac{\Omega}{\sqrt{\Omega^2 + (2\gamma\sigma_b)^4\tau^2}}} \tag{6.19}$$

as seen in Sect. 6.2.8. For the case of $A_\parallel \to 2A_\parallel$, we approximate the decay as Gaussian. The fitting function for Fig. 6.4e then becomes

$$\begin{aligned} P_{\{m,p\}} = \frac{\langle P_{0,U} \rangle}{4} \Bigg\{ &\sqrt{\frac{\Omega}{\sqrt{\Omega^2 + (2\gamma\sigma_b)^4\tau^2}}} \cos\left[\Omega\tau + \phi\right] \\ &+ e^{-\frac{t^2}{T_{2,\uparrow}^{*2}}} \cos\left[\tau\sqrt{\Omega^2 + 4A_\parallel^2} + \phi\right] \Bigg\} + c \end{aligned} \tag{6.20}$$

where only Ω, ϕ, c, and $T_{2,\uparrow}^*$ were allowed to vary as free parameters. We use $\langle P_{0,U} \rangle$ and the value of c returned from the fit to rescale the y-axis of Fig. 6.4e in terms of Re$[\rho_{m,p}]$.

For simplicity, this derivation of $f(\tau, \Omega, \sigma_b, A_\parallel)$ does not include driving field noise. Including amplitude noise in the mechanical driving field on the scale of

our power-leveled measurements produces no noticeable change in the results of the model over the range of mechanical driving fields addressed here.

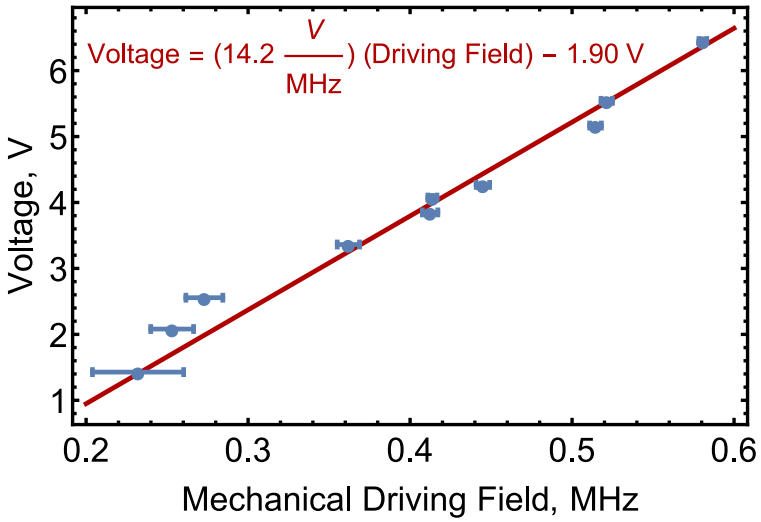

Figure 6.9: Voltage reflected from the mechanical resonator plotted as a function of the mechanical driving field.

6.3.10 Measuring the Voltage Reflected from the HBAR

We monitor the mechanical driving field amplitude by tracking the RF power reflected from the mechanical resonator. An RF circulator redirects the reflected power to an RF diode that converts the ac signal into the dc voltage that we measure. As shown in Fig. 6.9, this measured voltage scales linearly with the mechanical driving field. However, due to the diode's nonzero threshold voltage, that linear dependence has a nonzero intercept.

We introduce driving field noise to our experiment by periodically shifting the applied power such that the spread of voltages measured by the RF diode over the course of a measurement is normally distributed with a standard deviation of $\eta\langle V_R\rangle$ where V_R is the reflected voltage and η is a constant.

Because Fig. 6.9 has a nonzero intercept, such a distribution of voltages will correspond to a Gaussian distribution of driving fields with a standard deviation of $\sigma_\Omega = (\langle\Omega\rangle + \alpha)\eta$ where $\alpha/2\pi = -133 \pm 7$ kHz is the ratio of the intercept to the slope for the line of best fit in Fig. 6.9.

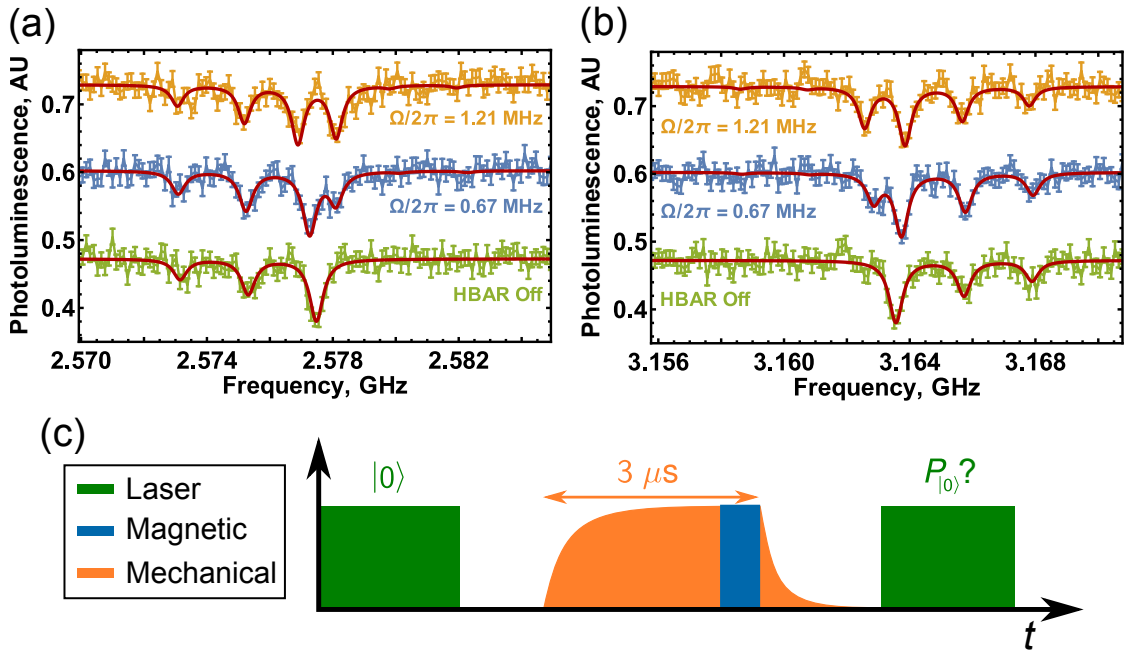

Figure 6.10: (a) Dressed state spectrum for a magnetic pulse swept through the undressed $|0\rangle \leftrightarrow |-1\rangle$ transition. (b) Dressed state spectrum for a magnetic pulse swept through the undressed $|+1\rangle \leftrightarrow |0\rangle$ transition. (c) Pulse sequence used in these measurements.

6.3.11 Dressed Spectra Through the $|+1\rangle \leftrightarrow |0\rangle$ Transition

Fig. 6.10 shows spectral measurements of the dressed state splitting as measured by sweeping the detuning of a $\Omega_{\text{mag}}/2\pi = 350$ kHz magnetic pulse through the resonance of the undressed (a) $|0\rangle \leftrightarrow |-1\rangle$ and (b) $|+1\rangle \leftrightarrow |0\rangle$ transitions. All three ^{14}N hyperfine sublevels are visible in the spectra. Because ω_{mech} is tuned into resonance with the $|(m_s =) + 1, (m_I =) + 1\rangle \leftrightarrow |-1, +1\rangle$ transition within

the ^{14}N hyperfine manifold, only the $m_I = +1$ peak splits into the dressed states $|m, +1\rangle$ and $|p, +1\rangle$. In these measurements, the HBAR was powered in 3 μs pulses as shown in Fig. 6.10c. This reduced the average power load and allowed us to reach higher driving fields than we were able to reach in the CDD Ramsey experiments where the mechanical resonator operates in a pseudo-cw mode.

6.4 Acknowledgments

We thank J. Maxson, A. Bartnik, B. Dunham, and I. Bazarov at the Cornell University Cornell Laboratory for Accelerator-Based Sciences and Education (CLASSE) for electron irradiating the diamond sample used in this work for the creation of NV centers. We thank P. Maletinksy for interesting and useful discussions.

Research support for Chapter 6 was provided by the Office of Naval Research (ONR) (Grant N000141410812). ERM received support from the Department of Energy Office of Science Graduate Fellowship Program (DOE SCGF), made possible in part by the American Recovery and Reinvestment Act of 2009, administered by ORISE-ORAU under contract no. DE-AC05-06OR23100. Device fabrication was performed in part at the Cornell NanoScale Science and Technology Facility, a member of the National Nanotechnology Coordinated Infrastructure, which is supported by the National Science Foundation (Grant ECCS-15420819), and at the Cornell Center for Materials Research Shared Facilities which are supported through the NSF MRSEC program (DMR-1120296).

CHAPTER 7

COOLING A MECHANICAL RESONATOR WITH NITROGEN-VACANCY CENTERS USING A ROOM TEMPERATURE EXCITED STATE SPIN-STRAIN INTERACTION [4]

7.1 Chapter Abstract

Cooling a mechanical resonator mode to a sub-thermal state has been a long-standing challenge in physics. This pursuit has recently found traction in the field of optomechanics in which a mechanical mode is coupled to an optical cavity. An alternate method is to couple the resonator to a well-controlled two-level system. Here we propose a protocol to dissipatively cool a room temperature mechanical resonator using a nitrogen-vacancy center ensemble. The spin ensemble is coupled to the resonator through its orbitally-averaged excited state, which has a spin-strain interaction that has not been previously studied. We experimentally demonstrate that the spin-strain coupling in the excited state is 13.5 ± 0.5 times stronger than the ground state spin-strain coupling. We then theoretically show that this interaction, combined with a high-density spin ensemble, enables the cooling of a mechanical resonator from room temperature to a fraction of its thermal phonon occupancy.

7.2 Main Text

Cooling a mechanical resonator to a sub-thermal phonon occupation can enhance sensing by lowering the resonator's thermal noise floor and extending a

sensor's linear dynamic range [120, 121, 122, 123]. Taken to the extreme, cooling a mechanical mode to the ground state of its motion enables the exploration of quantum effects at the mesoscopic scale [124, 125, 126]. These goals have motivated researchers in the field of optomechanics to invent methods for cooling mechanical resonators through their interactions with light. Such techniques have been able to achieve cooling to the ground state from cryogenic starting temperatures [125, 126] and to near the ground state from room temperature [127, 128, 129, 130, 131].

A well-controlled quantum system coupled to the motion of a resonator can also be used to cool a mechanical mode [35, 42]. Recently, nitrogen-vacancy (NV) centers in diamond have been coupled to mechanical resonators through coherent interactions with lattice strain [1, 31, 32, 2, 33, 3, 29, 30]. The opportunity to use these interactions has stimulated the development of single-crystal diamond mechanical resonators [49, 47, 50, 132] and motivated several theoretical proposals for cooling such resonators with a single NV center [35, 42, 133, 134]. In principle, replacing the single NV center with a many-NV ensemble can provide a collective enhancement to the strain coupling, which could increase the cooling power of these protocols. In practice, however, ensembles can shorten spin coherence times and introduce inhomogeneities that may make collective enhancement impractical, depending on the proposed mechanism. To make ensemble coupling a useful resource, it thus becomes crucial to design a cooling protocol that is insensitive to these side effects.

In this work, we study the hybrid quantum system composed of an NV center spin ensemble collectively coupled to a mechanical resonator with the goal of developing a method for cooling the resonator from ambient temperature.

Experimentally, we characterize the previously unstudied spin-strain coupling within the room temperature NV center excited state (ES), and we find that it is 13.5 ± 0.5 times stronger than the ground state (GS) spin-strain interaction. We then propose a dissipative cooling protocol that uses this ES spin-strain interaction and theoretically show that a dense NV center ensemble can cool a high-Q mechanical resonator from room temperature to a fraction of its thermal phonon population. The proposed protocol requires neither long spin coherence times nor strong spin-phonon coupling, and the cooling power scales directly with the NV center density. These properties make our proposed protocol a practical approach to cooling a room temperature resonator.

7.2.1 Results

NV Center-Strain Interactions

To achieve substantial cooling from ambient conditions, we require a room temperature NV center-strain interaction that can be enhanced by an ensemble. We first consider the orbital-strain coupling that exists within the NV center ES at cryogenic temperatures. This 850 ± 130 THz per strain interaction offers a promising route towards single NV center-mechanical resonator hybrid quantum systems [29, 30]. For ensemble coupling, however, inevitable static strain inhomogeneities will strongly broaden the orbital transition and prohibit collective enhancement. Moreover, the orbital coherence begins to dephase above 10 K due to phonon interactions [34], limiting applications of orbital-strain coupling to cryogenic operation.

A weaker (21.5 ± 1.2 GHz per strain) spin-strain coupling exists at room temperature within the NV center GS [32]. The resonance condition for this interaction is determined by a static magnetic bias field which can be very uniform across an ensemble. This GS spin-strain interaction thus offers a path towards coupling an ensemble to a mechanical resonator. As the NV center density grows, however, the GS spin coherence will decrease [135, 136], limiting the utility of the collective enhancement.

Finally, we consider spin-strain interactions in the room temperature ES, which have not been thoroughly investigated but might provide the desired compatibility with dense ensembles. For temperatures above ~ 150 K, orbital-averaging from the dynamic Jahn-Teller effect erases the orbital degree of freedom from the NV center ES Hamiltonian, resulting in an effective orbital singlet ES at room temperature [137, 138, 34, 139]. Previously, magnetic spectroscopy measured an unidentified spin splitting within the room temperature ES that is on the order of ten times stronger than the GS spin-strain interaction. These measurements hinted that this splitting might be a spin-strain interaction in the ES [140, 7]. Like the GS spin-strain coupling, the resonance condition for such an interaction would be determined by a static magnetic bias field, enabling collective enhancement with an ensemble. Furthermore, the NV center density is not expected to affect the ES coherence time, which is limited by the ES motional narrowing rate [141, 139]. Such an ES spin-strain interaction could thus offer a promising path towards coupling a dense NV center ensemble to a mechanical resonator. Our first goal then becomes to understand and precisely quantify this coupling.

Assuming this ES coupling is the result of a spin-strain interaction, we can write the spin Hamiltonian for an NV center in the presence of a magnetic field **B** and non-axial strain ϵ_x. Both the GS and room temperature ES Hamiltonians then take the form ($\hbar = 1$) [70, 7]

$$H = D_0 S_z^2 + \gamma_{\mathrm{NV}} \mathbf{S} \cdot \mathbf{B} - d_\perp \epsilon_x (S_x^2 - S_y^2) + A_\parallel S_z I_z \tag{7.1}$$

where $D_0^{\mathrm{e}}/2\pi = 1.42$ GHz and $D_0^{\mathrm{g}}/2\pi = 2.87$ GHz are the ES and GS zero-field splittings, $\gamma_{\mathrm{NV}}/2\pi = 2.8$ MHz/G is the NV center gyromagnetic ratio, $A_\parallel^{\mathrm{e}}/2\pi = +40$ MHz [81] and $A_\parallel^{\mathrm{g}}/2\pi = -2.166$ MHz are the ES and GS hyperfine couplings to the ^{14}N nuclear spin, **S** (**I**) is the electronic (nuclear) spin-1 Pauli vector, and the z-axis runs along the NV center symmetry axis. Perpendicular strain ϵ_x couples the $|(m_{\mathrm{s}} =) + 1\rangle$ and $|-1\rangle$ spin states with a strength $d_\perp^{\mathrm{e}}$ in the ES and $d_\perp^{\mathrm{g}}/2\pi = 21.5 \pm 1.2$ GHz per strain in the GS [32]. As shown in Fig. 7.1a, this interaction enables direct control of the magnetically-forbidden $|+1\rangle \leftrightarrow |-1\rangle$ spin transition within each orbital through resonant strain.

Device Details

The combination of a large hyperfine splitting in the ES and a short ES lifetime broadens the spectral features of the ES spin-strain interaction. Measuring such a spectrum then requires large magnetic field sweeps ($\Delta B_z \sim 150$ G), which in turn require a mechanical driving field with a high carrier frequency ($\omega_{\mathrm{m}}/2\pi \gtrsim 420$ MHz). To this end, we fabricate a high-overtone bulk acoustic resonator (HBAR) capable of generating large amplitude strain at gigahertz-scale frequencies. The resonator used in this work was driven at a $\omega_{\mathrm{m}}/2\pi = 529$ MHz mechanical mode that has a quality factor of $Q = 1790 \pm 20$. An antenna fab-

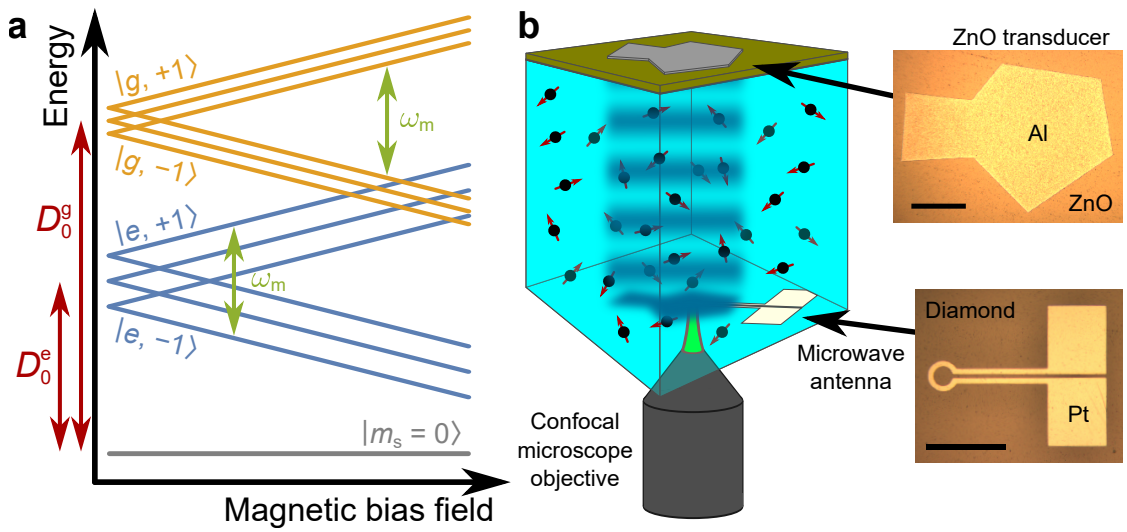

Figure 7.1: (a) NV center ground state and excited state energy levels as a function of the magnetic bias field. Energies have been plotted relative to the $m_s = 0$ state in each orbital, and a mechanical mode of frequency ω_m has been drawn connecting the $m_I = +1$ hyperfine sublevels. (b) Schematic of the device used in these measurements along with optical micrographs of the ZnO transducer used to generate the strain standing wave (150 μm scale bar) and the microwave antenna used to generate magnetic control fields (200 μm scale bar).

ricated on the opposite diamond face provides high-frequency magnetic fields for magnetic spin control. The final device is pictured in Fig. 7.1b.

Spin-Strain Spectroscopy

To measure mechanical spin driving within the ES, we execute the pulse sequences shown in Fig. 7.2a as a function of the magnetic bias field B_z. In the first sequence, a 532 nm laser initializes the NV center ensemble into the GS level $|g, (m_s =)0\rangle$. A magnetic adiabatic passage (AP) then moves the spin population to $|g, -1\rangle$. At this point, we pulse the mechanical resonator at its resonance frequency ω_m for 3 μs. Just before the end of the mechanical pulse, we apply a $\tau_{opt} = 125$ ns optical pulse with the 532 nm laser. This excites the ensemble to

$|e,-1\rangle$ and allows the spins to interact with the mechanical driving field in the ES. If the driving field is resonant with the $|e,+1\rangle \leftrightarrow |e,-1\rangle$ splitting, population will be driven into $|e,+1\rangle$. The spins then follow either a spin-conserving relaxation down to $|g,\pm1\rangle$ or a relaxation to the singlet state $|S_1\rangle$ through an intersystem crossing. The former preserves the spin state information, while relaxing to $|S_1\rangle$ re-initializes the state, erases the stored signal, and reduces the overall contrast of the measurement. After allowing the ensemble to relax, we apply a second magnetic AP to return the spin population in $|g,-1\rangle$ to $|g,0\rangle$ and measure the $|g,0\rangle$ population via fluorescence read out. We define this signal as S_1 and plot it as a function of τ_{opt} in Fig. 7.2b.

In the second pulse sequence, the mechanical pulse occurs between the second AP and fluorescence read out. Applying the mechanical pulse with the ensemble in $|g,0\rangle$ maintains the same power load on the device but does not drive spin population. This sequence measures S_2, the re-initialization of the ensemble from the τ_{opt} optical pulse (Fig. 7.2b). Subtracting $S_2 - S_1$ gives the probability of finding the ensemble in $|+1\rangle$ at the end of the first sequence. A third sequence with a single AP and a fourth with two APs (both with $\tau_{\text{opt}} = 0$) normalize the spin contrast at each B_z.

Fig. 7.2c shows the resulting experimental signal. The three broad, low peaks correspond to the hyperfine-split $|e,-1\rangle \rightarrow |e,+1\rangle$ transition, providing definitive evidence of a spin-strain interaction within the room temperature ES. Population is also driven into $|g,+1\rangle$ by the GS spin-strain interaction when the mechanical driving field is resonant with the $|g,+1\rangle \leftrightarrow |g,-1\rangle$ splitting. Fig. 7.2c thus contains both ES and GS spectra. We fit the data to the sum of three low, broad Lorentzians describing the ES spin-strain interaction and three taller, nar-

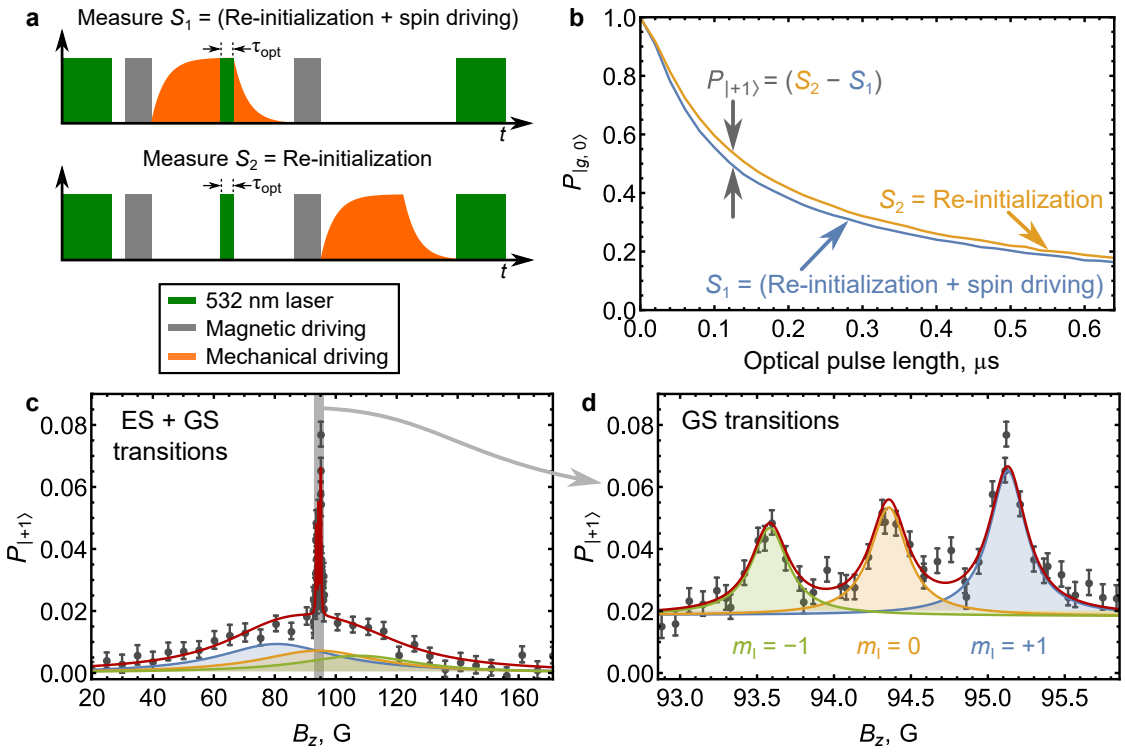

Figure 7.2: (a) Pulse sequences used to measure excited state (ES) spin driving. (b) Population in $|g, 0\rangle$ at the end of the pulse sequences in (a) plotted against τ_{opt}. (c) Spectrum of the spin population driven mechanically into $|+1\rangle$ by the ES and ground state (GS) spin-strain interactions. The red curve is a least squares fit to the sum of six Lorentzians. (d) Zoomed in view of the GS spin transitions in (c). The data in (c,d) were measured on one device with an NV center ensemble, and error bars are from the standard deviation in photon counting.

rower Lorentzians describing the GS interaction (see Methods). Fig. 7.2d highlights the GS driving with a zoomed in view of Fig. 7.2c about the GS resonances. The GS peaks have larger amplitudes than the ES peaks because the GS interaction acts for the entire duration of the $3\ \mu$s mechanical pulse, whereas the ES interaction only acts during the ~ 125 ns that the spin population is in the ES. Also, the reversed sign of $A_{\parallel}^{\text{e}}$ relative to $A_{\parallel}^{\text{g}}$ is consistent with *ab initio* calculations [142] and was confirmed by measurements presented in Sect. 7.3.1 that were conditional on the nuclear spin state.

Quantification of $d_{\perp}^{e}$

To quantify the strength of the ES spin-phonon interaction, we first calibrate the strain amplitude generated by the HBAR by mechanically driving Rabi oscillations within the GS and extracting the GS mechanical Rabi field Ω_g as a function of the applied power (Fig. 7.3a). Next, we spectrally isolate the $|e,+1\rangle \leftrightarrow |e,-1\rangle$ transition by fixing $B_z = 80$ G. At this field, the applied strain is on resonance in the ES but off resonance in the GS (see Fig. 7.2c). We then execute a modified version of the pulse sequence described above. Here, we use ~ 20 ns magnetic π-pulses to address the $|g,0\rangle \leftrightarrow |g,-1\rangle$ transition and measure both S_1 and S_2 as a function of τ_{opt} for each power level applied to the HBAR.

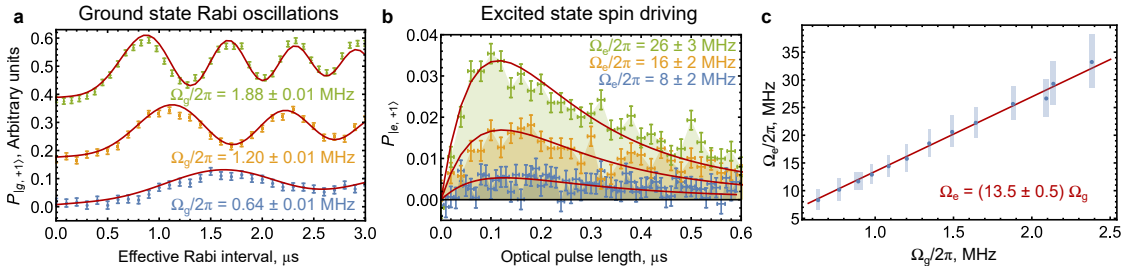

Figure 7.3: (a) Mechanically driven Rabi oscillations within the ground state (GS) that have been fit using the procedure described in Sect. 7.3.2. (b) Population in $|e,+1\rangle$ plotted as a function of τ_{opt}. The red curves are least squares fits to a seven-level master equation model of the measurement. The data in (a,b) were measured on a single device with an NV center ensemble, and error bars are from the standard deviation in photon counting. (c) The excited state mechanical driving field plotted against the GS mechanical driving field and fit with a linear scaling. Each point corresponds to a single measurement, and error bars are standard error from fits.

As Fig. 7.3b shows, taking $S_2 - S_1$ reveals a competition between mechanical driving into $|e,+1\rangle$ and re-initialization into $|0\rangle$ via optical pumping. For nonzero τ_{opt}, the ES mechanical driving field Ω_e drives spin population from $|e,-1\rangle$ to $|e,+1\rangle$, increasing $P_{|e,+1\rangle}$, but as τ_{opt} grows, optical pumping re-

initializes the ensemble into $|0\rangle$, vacating the $m_s = \{+1, -1\}$ subspace and reducing $P_{|e,+1\rangle}$ to zero. A seven-level master equation model recreates this competition and provides good fits to the data. From these fits, we extract the value of Ω_e. The Methods section includes a detailed description of this model, which was designed to account for inhomogeneities within the NV center ensemble and for the polarization of the nuclear spin sublevels, among other effects. Plotting Ω_e against Ω_g (Fig. 7.3c) shows that the transverse spin-strain coupling in the ES is 13.5 ± 0.5 times stronger than the GS coupling, or $d_\perp^e/2\pi = 290 \pm 20$ GHz per strain.

Resonator Cooling Protocol

With $d_\perp^e$ quantified, we now present a dissipative protocol for cooling a mechanical resonator with an NV center spin ensemble. In our proposed protocol, a 532 nm laser continuously pumps the phonon sidebands of the ensemble's optical transition, and a gigahertz frequency magnetic field continuously drives the $|g, 0\rangle \leftrightarrow |g, -1\rangle$ spin transition. This generates a steady state population surplus in $|e, -1\rangle$ as compared to $|e, +1\rangle$, enabling the net absorption of phonons by the ensemble. Spontaneous relaxation and subsequent optical pumping continually re-initialize the system, allowing the phonon absorption cycle to continue. Fig. 7.4a summarizes this process.

The dissipative nature of this protocol enables resonator cooling without requiring strong spin-phonon coupling. Here, we define strong coupling as a single spin cooperativity $\eta = \lambda^2 T_2^*/\gamma n_{th} > 1$, where λ is the is the single spin-single phonon coupling strength, T_2^* is the inhomogeneous spin dephasing time, $\gamma = \omega_m/Q$ is the mechanical dissipation rate, and $n_{th} \sim k_B T/\hbar\omega_m$ is the thermal

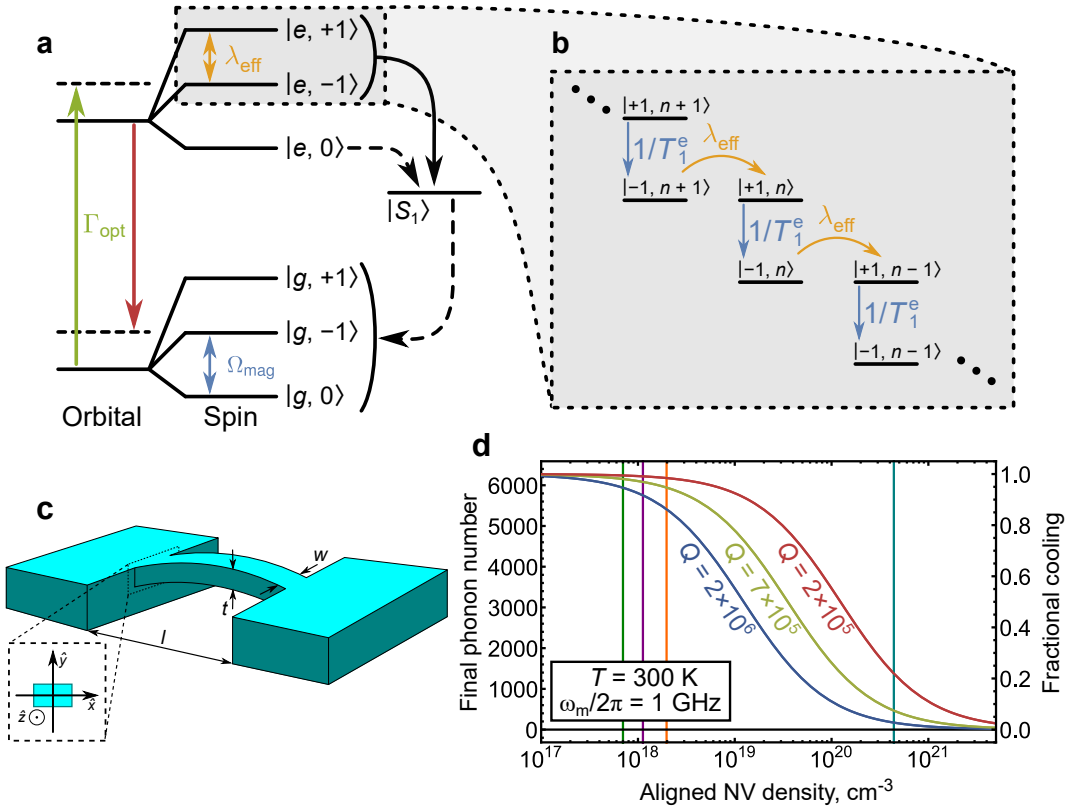

Figure 7.4: (a) The seven NV center orbital and spin states at room temperature. Fast (slow) transitions are indicated by solid (dashed) one-way arrows. Coherent couplings are indicated by two-way arrows. (b) The toy model depiction of the proposed cooling protocol. (c) Schematic of a doubly-clamped beam. (d) Final phonon number achieved by the cooling protocol as a function of the density of properly aligned NV centers. Vertical lines indicate densities that have been realized in single-crystal diamonds (7.0×10^{17} cm^{-3} [136], 1.1×10^{18} cm^{-3} [143], 2.0×10^{18} cm^{-3} [144]) and nanodiamonds (4×10^{20} cm^{-3} [145]).

phonon occupancy of the resonator mode [41]. A cooperativity of $\eta > 1$ marks the threshold for coherent interactions between the spin and the mechanical mode. Non-idealities in spin coherence and resonator fabrication have thus far prevented the experimental realization of NV center cooperativities approaching unity, especially at room temperature. This makes the proposed dissipative protocol a practical and attractive approach because it does not require coherent interactions for resonator cooling to occur.

To analyze the performance of the protocol we start by considering a single two-state spin system coupled to a mechanical resonator. The resulting dynamics obey the master equation ($\hbar = 1$)

$$\dot{\rho} = -i[H, \rho] + \mathcal{L}_\Gamma \rho + \mathcal{L}_\gamma \rho \tag{7.2}$$

where H describes the coherent coupling between the spin and the resonator, $\mathcal{L}_\Gamma$ describes the incoherent spin processes, and $\mathcal{L}_\gamma$ describes the resonator rethermalization. For resonant coupling, the quantized Hamiltonian in the Jaynes-Cummings form is [146]

$$H = \omega_{\mathrm{m}}(a^\dagger a + S_+ S_-) + \lambda(S_+ + S_-)(a^\dagger + a) \tag{7.3}$$

where $a^\dagger$ (a) is the creation (annihilation) operator for the mechanical mode and $S_\pm$ are the ladder operators for the spin state. The spin relaxation term in Eq. 7.2 takes the form $\mathcal{L}_\Gamma \rho = (2T_1)^{-1}\mathcal{D}[S_-]\rho + (2T_2^*)^{-1}(S_z \rho S_z - \rho)$ where $\mathcal{D}[S_-]\rho = (2S_-\rho S_+ - S_+ S_- \rho - \rho S_+ S_-)$ is the Lindblad superoperator and T_1 (T_2^*) is the transverse (longitudinal) spin coherence time. The resonator rethermalization is described by $\mathcal{L}_\gamma \rho = \frac{\gamma}{2}(n_{\mathrm{th}} + 1)\mathcal{D}[a]\rho + \frac{\gamma}{2} n_{\mathrm{th}} \mathcal{D}[a^\dagger]\rho$.

Within this two-state model, an analytic expression for the steady state phonon number n_{f} can be found by using the matrix of second order moments (Sect. 7.3.3) [147]. Under the secular approximation and working in the limit $\gamma, \lambda \ll 1/T_1, 1/T_2^*$, the dynamical equation for the phonon occupancy $n = \langle a^\dagger a \rangle$ can be simplified to

$$\frac{dn}{dt} = \gamma\,(n_{\mathrm{th}} - n) - \frac{4\lambda^2}{2/T_2^* + 1/T_1} n. \tag{7.4}$$

For an ensemble of N spins coupled to the resonator but not to one another, each spin will add an additional damping term to the resonator dynamical equation. This allows us to rewrite the last term in Eq. 7.4 as $\sum_{i=1}^{N} \frac{4\lambda_i^2}{2/T_{2,i}^* + 1/T_{1,i}} n$. If

each spin within the ensemble has the same T_1 and T_2^*, we can factorize this expression and replace the individual λ_i with an effective ensemble-resonator coupling $\lambda_{\text{eff}} = \sqrt{\sum_{i=1}^{N} \lambda_i^2}$. For the case of uniform coupling, this simplifies to $\lambda_{\text{eff}} = \sqrt{N}\lambda$, which is equivalent to the effective coupling in the Tavis-Cummings model [148, 149]. Solving for the steady state of the system then gives

$$n_{\text{f}} = \frac{\gamma n_{\text{th}}}{\gamma + \frac{4\lambda_{\text{eff}}^2}{2/T_2^* + 1/T_1}}. \tag{7.5}$$

The problem now becomes mapping the seven-level NV center structure pictured in Fig. 7.4a onto this two-state spin system. We do this by distilling the seven-level landscape to a toy model that contains only the two states that couple to the mechanical resonator, $|e, +1\rangle$ and $|e, -1\rangle$, as shown in Fig. 7.4b. Within this simplified landscape, we assign T_2^* to be the ES coherence time ($T_{2\text{e}}^* = 6.0$ ns [150]) and T_1 to be the ES lifetime of $|e, +1\rangle$ ($T_{1\text{e}} = 6.89$ ns [151]). At any one moment, only a fraction α of the spins within the ensemble will be in the proper $\{|e, +1\rangle, |e, -1\rangle\}$ subspace to participate in the cooling. We account for this by modifying $\lambda_{\text{eff}} \rightarrow \sqrt{\alpha}\lambda_{\text{eff}}$. To determine α, we solve for the 7×7 density matrix describing the steady state of the ensemble in the absence of the mechanical resonator, calculate the population difference between $|e, -1\rangle$ and $|e, +1\rangle$, and obtain $\alpha = 0.017$ for optimized control fields (Sect. 7.3.4).

Elasticity theory provides a means of calculating the remaining device parameters. For a doubly-clamped beam of length l, thickness t, and width w, we compute λ_{eff} from the strain due to the zero-point motion of the resonator $\epsilon_0(y, z)$ with coordinates as defined in Fig. 7.4c (see Methods). For a uniform

distribution of properly aligned NV centers at a density ν, we obtain [25, 41]

$$\lambda_{\text{eff}} = d_{\perp}^{\text{e}} \sqrt{\alpha \nu w} \sqrt{\int_0^l \int_{-t/2}^{t/2} \epsilon_0^2(y,z) dy dz}. \tag{7.6}$$

Evaluating Eq. 7.6, we find that λ_{eff} is independent of w and scales as $\lambda_{\text{eff}} = G_0 \sqrt{\nu t}/l$ where $G_0 = d_{\perp}^{\text{e}} \sqrt{\hbar \alpha \kappa_0 / E}$, $\kappa_0 = 120$ GHz·μm, and $E = 1200$ GPa is the Young's modulus of diamond. The frequency of the resonator's fundamental mode scales as $\omega_{\text{m}} = \kappa_0 t / l^2$. As described in Sect. 7.3.5, higher order mechanical modes are spectrally isolated from the NV center spin dynamics in the devices considered here [41, 32]. For any thin-beam resonator in the resolved-sideband regime ($\omega_{\text{m}}/2\pi > 1/T_{2\text{e}}^* \sim 170$ MHz), the fractional cooling $n_{\text{f}}/n_{\text{th}}$ is insensitive to the physical dimensions of the resonator because the size of the ensemble scales with the size of the resonator. This can be seen by rewriting Eq. 7.5 as $n_{\text{f}}/n_{\text{th}} = (1+\chi)^{-1}$ where $\chi = \frac{4\hbar Q \nu \alpha (d_{\perp}^{\text{e}})^2}{E\left(2/T_{2\text{e}}^* + 1/T_{1\text{e}}\right)}$ is independent of the resonator dimensions. For illustrative purposes, we choose to examine a resonator with a $\omega_{\text{m}}/2\pi = 1$ GHz fundamental mode and assume fully polarized nuclear spins [152]. Potential device dimensions then become $(l, t) = (1.9, 0.19)$ μm. Finally, phonon-phonon interactions limit the Q of an ideal diamond mechanical resonator at room temperature. For modes satisfying $\omega_{\text{m}}/2\pi > 1/T_{2\text{e}}^*$, the maximum $Q = 2 \times 10^6$ is independent of ω_{m} [153], and we now have all the parameters needed to study the performance of the protocol.

At this point, we note that distilling a seven-state model to the toy model we employ certainly requires validation. To justify our simplified model, we calculate the cooling predicted within the toy model and compare this both to an analytical Lamb-Dicke treatment of the seven-level model [154, 42] and to numerical simulations of a small number of seven-level NV centers coupled to a resonator. Due to the exponential growth of the Hilbert space, full

seven-level numerical simulations were performed on the Titan supercomputer at Oak Ridge National Laboratory, with the most intensive simulations taking $\sim 10^4$ core-hours. Comparing the toy model and Lamb-Dicke results to the numerical simulations, we determined that the two-level distillation outperforms the Lamb-Dicke approach in all test cases and provides an upper bound on n_{f} (Sect. 7.3.6). This indicates that the proposed protocol cools a resonator more efficiently than our toy model predicts [155, 156, 157, 158].

Cooling Performance

The lowest phonon occupancy that can be reached depends strongly on the density of properly aligned NV centers ν. For instance, Choi, *et al* reported measurements of an NV center ensemble with $\nu = 2.0 \times 10^{18}$ cm^{-3} in single-crystal diamond [144]. For this density and $Q = 2\times10^6$, we find that the proposed protocol cools a room temperature resonator to $n_{\mathrm{f}} = 0.86 n_{\mathrm{th}}$. Using the same Q and the density of $\nu = 4 \times 10^{20}$ cm^{-3} reported by Baranov, *et al* in nanodiamonds [145], however, the protocol can cool to $n_{\mathrm{f}} = 0.03 n_{\mathrm{th}}$.

Increasing the size of the ensemble can thus dramatically increase the protocol's cooling power. The magnetic field noise from paramagnetic impurities will also grow with ν, degrading the GS coherence time. However, for large magnetic driving fields, this cooling protocol does not require a lengthy GS coherence time (Sect. 7.3.4). The only coherence time that effects the protocol is $T_{2\mathrm{e}}^*$, which is not expected to change with the defect density [141, 139]. This means that large NV center densities could in principle be used to cool a resonator with the ES spin-strain interaction. To study how increasing ν affects the protocol, we plot n_{f} against ν in Fig. 7.4d for several different Q-values. For ref-

erence, we have included lines marking values of ν that have been realized in single-crystal diamonds [136, 143, 144] and in nanodiamonds [145]. The limiting density of NV centers in a single-crystal diamond nanostructure is currently unknown. Furthermore, while high defect densities have been shown to degrade the Q of $\omega_{\rm m}/2\pi \sim 10$ kHz frequency resonators [159], it remains to be seen how the gigahertz frequency resonators of interest here will be affected by the incorporation of a dense defect ensemble. These questions motivate future experimental work.

7.2.2 Discussion

The insensitivity of the proposed protocol to the GS coherence time makes an ES cooling protocol an attractive and practical route to cooling a room temperature mechanical resonator with NV centers. Alternative approaches that use the GS spin-strain coupling [2, 33, 50] are incompatible with the collective enhancement from a dense ensemble that makes the proposed protocol viable. Although the GS inhomogeneous dephasing time $T_{2\rm g}^*$ can be $\sim \mu$s long in high purity diamonds, $T_{2\rm g}^*$ scales roughly as $\sim 1/\nu$ in bulk diamond and can be < 100 ns for dense ensembles [135, 136]. Within a nanostructure, effects such as exchange narrowing and the truncation of the spin bath mitigate this reduction in $T_{2\rm g}^*$ [160, 145] and make it difficult to predict the decrease in $T_{2\rm g}^*$ inside a doubly-clamped beam. Nevertheless, we can roughly compare the ES and GS spin-strain interactions by calculating η using coherence times measured in bulk diamond (Sect. 7.3.7). For a moderate NV center density of $\nu = 2.8 \times 10^{13}$ cm^{-3} [2], the single-spin cooperativity for the ES spin-strain interaction is 2.4-times larger than in the GS, and for $\nu = 7.0 \times 10^{17}$ cm^{-3} [136], η is 19-times larger in the ES.

In both cases, the ES offers the more efficient route to cooling, and as the collective enhancement grows, the ES interaction becomes increasingly more efficient than the GS interaction. A dense ensemble coupled via the ES spin-strain interaction thus becomes the more promising route to cooling a room temperature mechanical resonator with NV centers.

It is important to note that this analysis of the proposed protocol only applies for operation at room temperature. Reducing the bath temperature will lower n_{th} and would thus ideally lower n_{f}. However, the ES coherence time is limited by the ES motional narrowing rate, which increases as the bath temperature decreases [141, 139]. This is expected to lead to a reduction in $T_{2\mathrm{e}}^{*}$ at lower temperatures, followed by a complete loss of ES spin coherence below ~ 150 K [137]. As seen from Eq. 7.5, a reduction in $T_{2\mathrm{e}}^{*}$ will lead to a loss of cooling power. For cryogenic starting temperatures, it thus becomes necessary to use either the GS spin-phonon interaction or the orbital-strain interaction to cool a mechanical resonator with NV centers.

Finally, n_{f} could be lowered further by simultaneously implementing an optomechanical cooling protocol [127, 128, 129, 130, 131] alongside the proposed protocol. Optomechanical cooling has been demonstrated to cool gigahertz frequency resonators to $n_{\mathrm{f}} \sim 0.01 n_{\mathrm{th}}$ [125, 161]. The cooling rate from an optimized realization of the proposed protocol would combine additively with the optomechanical cooling rate, allowing the two complementary techniques to operate in conjunction and enhance the total cooling.

In conclusion, we have proposed a dissipative protocol for cooling a room temperature mechanical resonator that utilizes an ensemble of NV center spins to realize a collective enhancement in the spin-phonon coupling. After experi-

mentally determining that the spin-strain coupling in the room temperature ES is 13.5 ± 0.5 times stronger than the GS spin-strain coupling, we analyzed the performance of the cooling protocol. For very dense NV center ensembles, the proposed protocol can cool a room temperature resonator to a fraction of its thermal phonon occupancy. These results shed further light on the orbitally-averaged room temperature ES of the NV center and demonstrate a practical path towards cooling a room temperature mechanical resonator with NV centers.

7.2.3 Methods

Sample Details

Our HBAR consists of a 2.5 μm-thick ZnO piezoelectric film sandwiched between a $25/200$ nm Ti/Pt ground plane and a 250 nm thick apodized Al top electrode, all sputtered on one face of a $\langle 100 \rangle$ single-crystal diamond substrate. Applying a high-frequency voltage to this transducer launches acoustic waves into the diamond, which then serves as a Fabry-Pérot cavity to generate a comb of standing wave resonances. By apodizing the shape of the Al electrode, we mitigate the loss of power into lateral modes formed across the diameter of the HBAR. The antenna fabricated on the opposite diamond face was patterned from $25/225$ nm Ti/Pt with a lift-off process.

The CVD-grown diamond used in these measurements contained NV centers at a density of $\sim 4 \times 10^{14}$ cm^{-3} as purchased. Our measurements thus address an ensemble of ~ 70 NV centers oriented with their symmetry axis parallel

to B_z. NV centers of different orientations are spectrally isolated and contribute only a constant background to the measurements.

Spectrum Fitting

The spectrum pictured in Fig. 7.2 was fit to the function

$$P_{|+1\rangle} = c_{\mathrm{e}}\left(\frac{a_+[B_z]}{\frac{1}{4}\Gamma_{\mathrm{e}}^2+(B_z-B_0+A_{\parallel}^{\mathrm{e}}/\gamma_{\mathrm{NV}})^2}+\frac{a_0[B_z]}{\frac{1}{4}\Gamma_{\mathrm{e}}^2+(B_z-B_0)^2}+\frac{a_-[B_z]}{\frac{1}{4}\Gamma_{\mathrm{e}}^2+(B_z-B_0-A_{\parallel}^{\mathrm{e}}/\gamma_{\mathrm{NV}})^2}\right) + c_{\mathrm{g}}\left(\frac{a_+[B_z]}{\frac{1}{4}\Gamma_{\mathrm{g}}^2+(B_z-B_0+A_{\parallel}^{\mathrm{g}}/\gamma_{\mathrm{NV}})^2}+\frac{a_0[B_z]}{\frac{1}{4}\Gamma_{\mathrm{g}}^2+(B_z-B_0)^2}+\frac{a_-[B_z]}{\frac{1}{4}\Gamma_{\mathrm{g}}^2+(B_z-B_0-A_{\parallel}^{\mathrm{g}}/\gamma_{\mathrm{NV}})^2}\right) \tag{7.7}$$

where c_{e} and c_{g} are constant amplitudes that quantify the driven spin contrast for the ES and GS resonances, $a_i[B_z]$ are field-dependent scaling factors that account for the dynamic nuclear polarization of the hyperfine sublevels [152], Γ_{e} (Γ_{g}) is the FWHM of the ES (GS) resonances, B_0 is the resonant field for the $m_{\mathrm{I}} = 0$ hyperfine sublevel, and the other parameters are as defined above. Of these variables, c_i, Γ_i, and B_0 are free parameters in our fitting procedure.

We calibrate $a_i[B_z]$ by performing hyperfine-resolved magnetically-driven electron spin resonance (ESR) measurements within the NV center GS at different values of the magnetic bias field B_z. This is done by fixing B_z and monitoring the NV center photoluminescence as the carrier frequency of a magnetic driving field oriented along B_x is swept through the $|g,0\rangle \leftrightarrow |g,-1\rangle$ spin reso-

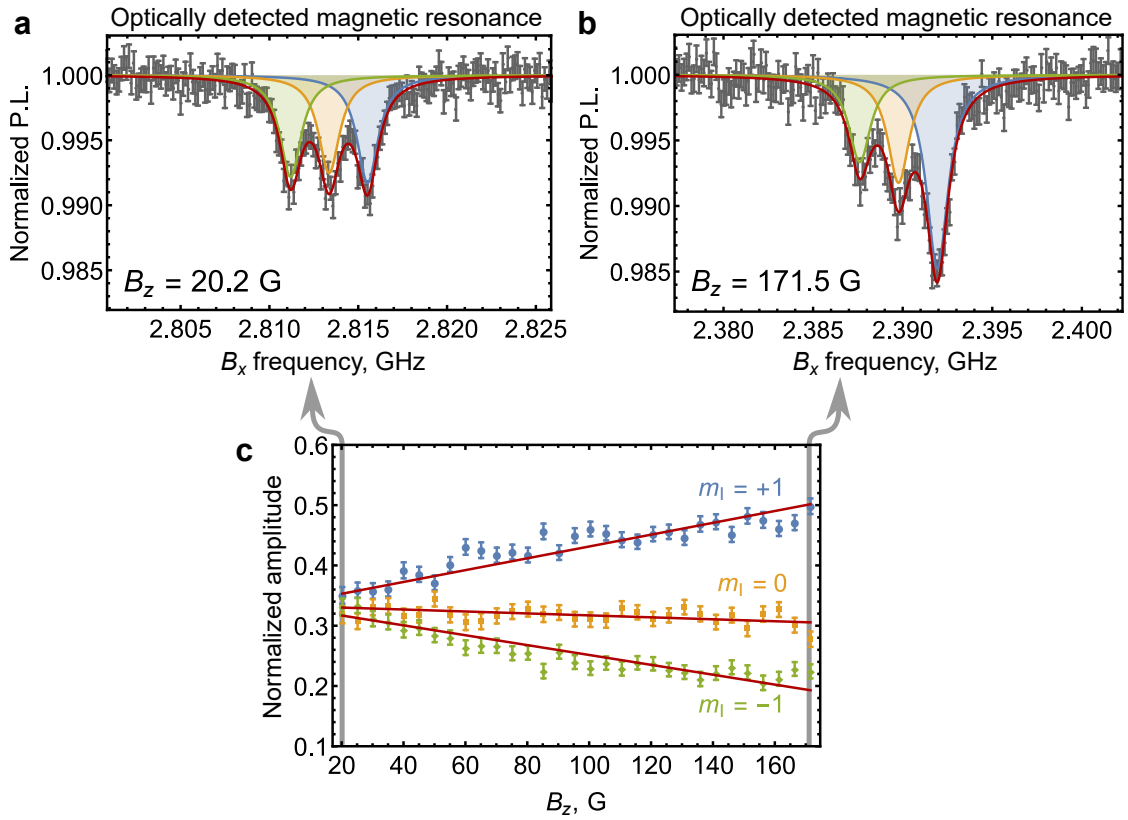

Figure 7.5: (a,b) Normalized photoluminescence (P.L.) plotted as a function of the magnetic driving field carrier frequency for (a) $B_z = 20.2$ G and (b) $B_z = 171.5$ G. The solid line in each plot is a least squares fit to the sum of three Lorentzians. The data in (a,b) was measured on a single device with an NV center ensemble, and error bars are from the standard deviation in photon counting. (c) Normalized amplitude of each m_I hyperfine sublevel as a function of B_z. The solid lines are least squares fits to a linear model, each point corresponds to a single measurement, and error bars are standard error from fits.

nance. We fit the resulting curves to the function

$$P = C\left(\frac{A_+}{\frac{1}{4}\Gamma_\mathrm{g}^2 + (B_z - B_0 + A_\parallel^\mathrm{g})^2} + \frac{A_0}{\frac{1}{4}\Gamma_\mathrm{g}^2 + (B_z - B_0)^2} + \frac{A_-}{\frac{1}{4}\Gamma_\mathrm{g}^2 + (B_z - B_0 - A_\parallel^\mathrm{g})^2}\right) + P_0 \tag{7.8}$$

where P is the measured photoluminescence, C accounts for the driven spin contrast, A_i is the relative amplitude of each hyperfine sublevel, P_0 is the back-

ground photoluminescence, and we fix $\sum A_i = 1$. Fig. 7.5a,b show ESR curves measured at $B_z = 20.2$ G and 171 G. We have used the values of P_0 returned from the fits to normalize the photoluminescence.

Fig. 7.5c shows the normalized amplitude of each nuclear sublevel plotted as a function of B_z. As expected, the nuclear polarization increases in the direction of the ES level anti-crossing at $B_z^{\mathrm{LAC}} = 507$ G. In this figure, we have fit each curve to a straight line with a fixed y-intercept of $\frac{1}{3}$ to obtain the linear scaling functions $a_i[B_z]$ in Eq. 7.7. The sum of these scaling functions satisfies $\sum a_i[B_z] = 1$.

Seven-Level Master Equation Model

The master equation used to model our ES spin driving measurements is derived in the room temperature NV center basis defined by the states $\{g_{+1}, g_0, g_{-1}, e_{+1}, e_0, e_{-1}, S_1\}$ where, within the e and g subspaces, a subscript denotes the m_{s} value. The 7×7 density matrix evolves according to ($\hbar = 1$)

$$\dot{\rho} = -i[H, \rho] + \mathcal{L}_\Gamma \rho. \tag{7.9}$$

In the rotating frame, the Hamiltonian is given by

$$H = \frac{\Omega_{\mathrm{e}}}{2} \left(|e_{+1}\rangle \langle e_{-1}| + |e_{-1}\rangle \langle e_{+1}| \right) + \Delta_{\mathrm{m}} |e_{+1}\rangle \langle e_{+1}| \tag{7.10}$$

where Δ_{m} is the mechanical detuning. The incoherent NV center processes are described by the superoperator

$$\begin{aligned} \mathcal{L}_\Gamma \rho = & \Gamma_{\mathrm{opt}} \sum_{i=\pm 1,0} L_{g_i,e_i} + k_{42} \sum_{i=\pm 1} L_{e_i,g_i} + k_{45} \sum_{i=\pm 1} L_{e_i,S_1} + k_{52} \sum_{i=\pm 1} L_{S_1,g_i} \\ & + k_{31} L_{e_0,g_0} + k_{35} L_{e_0,S_1} + k_{51} L_{S_1,g_0} + \frac{1}{T_{2\mathrm{e}}^*} \sum_{i=\pm 1,0} L_{e_i,e_i} \end{aligned} \tag{7.11}$$

Parameter	Value	Relaxation From:
k_{42}	65.3 ± 1.6 MHz	ES $\|\pm 1\rangle$ to GS $\|\pm 1\rangle$
k_{31}	64.9 ± 1.5 MHz	ES $\|0\rangle$ to GS $\|0\rangle$
k_{45}	79.8 ± 1.6 MHz	ES $\|\pm 1\rangle$ to $\|S_1\rangle$
k_{35}	10.6 ± 1.5 MHz	ES $\|0\rangle$ to $\|S_1\rangle$
k_{52}	2.61 ± 0.06 MHz	$\|S_1\rangle$ to GS $\|\pm 1\rangle$
k_{51}	3.00 ± 0.06 MHz	$\|S_1\rangle$ to GS $\|0\rangle$

Table 7.1: Relaxation rates used in our seven-level master equation model [151].

where we define

$$L_{i,f}\rho = |f\rangle \langle i| \rho |i\rangle \langle f| - \frac{1}{2} \left(|i\rangle \langle i| \rho + \rho |i\rangle \langle i| \right). \tag{7.12}$$

Here, Γ_{opt} is the optical pumping rate of our 532 nm laser, $T_{2\text{e}}^* = 6.0 \pm 0.8$ ns is the ES coherence time [150], and the relaxation rates k_{ij} are listed in Table 7.1. Fig. 7.6a summarizes this landscape.

Because optical initialization does not generate a pure state, we first simulate the optical pumping process to obtain an initialized density matrix. To do so, we start with a thermal state $\rho_{\text{NV}} = \frac{1}{3} \left(\sum_{i=\pm 1,0} |g_i\rangle \langle g_i| \right)$ and apply Eq. 7.9 with $\Omega_{\text{e}}, \Delta_{\text{m}} = 0$ and $\Gamma_{\text{opt}} \neq 0$ for 10 μs. We take the resulting density matrix and apply Eq. 7.9 for 5 μs with $\Omega_{\text{e}}, \Delta_{\text{m}}, \Gamma_{\text{opt}} = 0$ to simulate the relaxation to $|g\rangle$. A simulated π-pulse then swaps ρ_{22} and ρ_{33}, providing the appropriate starting density matrix ρ_0 for a given Γ_{opt}. From ρ_0, we also extract the minimum and maximum spin contrast ($s_{\text{min}} = \langle g_0| \rho_0 |g_0\rangle$ and $s_{\text{max}} = \langle g_{-1}| \rho_0 |g_{-1}\rangle$), which allow us to properly normalize our simulations.

Next, we model the measurement of S_2, the spin re-initialization. To do so, we apply Eq. 7.9 to ρ_0 with $\Omega_{\text{e}}, \Delta_{\text{m}} = 0$ and $\Gamma_{\text{opt}} \neq 0$ for a length of time τ_{opt}. Allowing the spin to relax as before gives us the measured density matrix ρ_2.

We normalize $\langle g_{-1}| \rho_2 |g_{-1}\rangle$ using s_{min} and s_{max}, and repeat this simulation as a function of τ_{opt} to obtain a simulated S_2 curve.

To account for spatial inhomogeneities in the optical power within the NV center ensemble, we perform a weighted average of this simulation over the point spread function (PSF) of our microscope. We approximate the PSF by the function

$$\Gamma_{\text{opt}}(z) = \Gamma_0 \left\{ \frac{\sin\{\kappa[z_0](z - z_0)\}}{\kappa[z_0](z - z_0)} \right\}^2 \tag{7.13}$$

where Γ_0 is the peak optical pumping rate, $\kappa[z_0]$ defines the depth-dependent PSF width [1], z is the distance below the diamond surface, and $z_0 = 7.9 \pm 0.9\ \mu$m is the focus depth of the PSF. An ensemble measurement is then given by

$$S_2^{\text{ens}}(\tau_{\text{opt}}) = \frac{\int_0^\infty S_2[\tau_{\text{opt}}, \Gamma_{\text{opt}}(z)]dz}{\int_0^\infty \Gamma_{\text{opt}}(z)dz}. \tag{7.14}$$

We discretize this integral to make it computationally tractable and perform a least squares fit of $S_2^{\text{ens}}(\tau_{\text{opt}})$ to the measured data. Γ_0 is the only free parameter in the fitting procedure.

With the exception of the datum indicated in Fig. 7.6b, all of the measurements were taken at the same optical power. We simultaneously fit each of these S_2 curves and find $\Gamma_0 = 19.1 \pm 1.6$ MHz. For the measurement at a different optical power, we find $\Gamma_0 = 16.5 \pm 1.7$ MHz.

To extract Ω_{e}, we then fix Γ_0 and repeat this procedure with $\Omega_{\text{e}} \neq 0$ to simulate the $S_2 - S_1$ measurement pictured in Fig. 7.3b. To account for inhomogeneities in the mechanical driving field, we must also include the spatial profile of the strain standing wave inside the weighted average. This function takes the form $\Omega_{\text{e}}(z) = \Omega_0 |\sin[2\pi z/\lambda]|$ where $\lambda = 31 \pm 4\ \mu$m is the wavelength of the strain wave. Defining the results of such a simulation as $P_{|+1\rangle}(\Omega_{\text{e}}, \Delta_{\text{m}})$, we account for

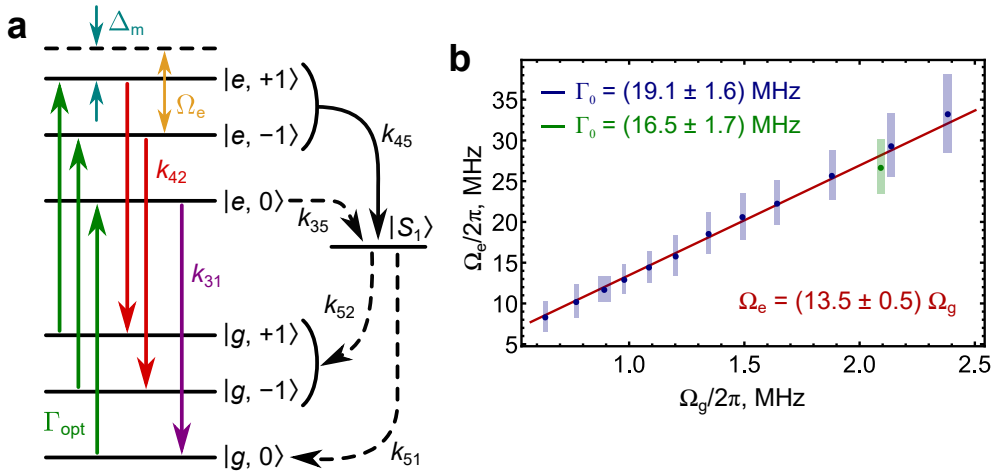

Figure 7.6: (a) States and transitions included in our seven-level master equation model. The k_{ij} rates are listed in Table 7.1. (b) Excited state mechanical driving field Ω_e plotted as a function of the ground state mechanical driving field Ω_g with the data labeled by the optical pumping rate Γ_0 during each measurement. Each point corresponds to a single measurement, and error bars are standard error from fits.

the hyperfine sublevels by computing the sum

$$P_{|+1\rangle}\left(\Omega_e\right) = a_{+1}P_{|+1\rangle}\left(\Omega_e, 0\right) + a_0 P_{|+1\rangle}\left(\Omega_e, A_{\parallel}^e\right) + a_{-1}P_{|+1\rangle}\left(\Omega_e, 2A_{\parallel}^e\right) \tag{7.15}$$

where the normalized amplitudes ($\sum a_i = 1$) account for nuclear spin polarization and have been measured separately via magnetic ESR. A least squares fit of Eq. 7.15 to the data then provides Ω_e. Here, Ω_e is the only free parameter in the fitting procedure.

When fitting the relation between Ω_e and Ω_g (Fig. 7.3c), we fix the y-intercept of the linear fitting function to be zero.

Elasticity Theory

To analyze how strain couples to NV centers within a resonator, we start by assuming that the NV centers are aligned with the direction of beam deflection

such that the strain in an oscillating beam is entirely perpendicular to the NV center symmetry axis. We then use elasticity theory to derive the scaling laws quoted above [41, 32].

The wave equation for doubly-clamped beams is

$$\rho_{\mathrm{d}} A \frac{\partial^2}{\partial t^2}\phi(t,z) = -EI\frac{\partial^4}{\partial z^4}\phi(t,z) \tag{7.16}$$

where $\phi(t,z)$ is the transverse displacement in the y-direction, $\hat{z}$ points along the beam as indicated in Fig. 7.4c, $A = wt$ is the cross-sectional area of the resonator, $E = 1200$ GPa is the Young's modulus of diamond, $\rho_{\mathrm{d}} = 3.515$ g·cm^{-3} is the mass density of diamond, and $I = wt^3/12$ is the resonator's moment of inertia. Solutions are of the form $\phi(z,t) = u(z)e^{-i\omega t}$ where

$$u_n(z) = a_n\left(\cos k_n z - \cosh k_n z\right) - b_n\left(\sin k_n z - \sinh k_n z\right), \tag{7.17}$$

and the allowed k-vectors satisfy $\cos\left(k_n z\right)\cosh\left(k_n z\right) = 1$. The wave vector and amplitudes of the fundamental mode satisfy $k_0 l = 4.73$ and $a_0/b_0 = 1.0178$.

We normalize $u_n\left(z\right)$ by setting the free energy of the beam equal to the zero point energy of the mode:

$$W = \frac{1}{2}EI\int_0^L \left(\frac{\partial^2 u_n}{\partial z^2}\right)^2 dz = \frac{1}{2}\hbar\omega_n \tag{7.18}$$

where the eigenfrequencies of the resonator are given by $\omega_n = k_n^2\sqrt{EI/\rho_{\mathrm{d}}A}$. This expression for ω_n can be simplified to $\omega_n = \kappa_n t/l^2$ where $\kappa_n = (k_n l)^2\sqrt{E/12\rho_{\mathrm{d}}}$. For the fundamental mode, $\kappa_0 = 120$ GHz·μm as quoted above.

The spin-phonon coupling for a single NV center located at (y,z) is given by $\lambda = d_\perp \epsilon_0\left(y,z\right)$ where $\epsilon_0\left(y,z\right) = -y\frac{\partial^2}{\partial z^2}u_n(z)$ is the strain from the zero point motion of the resonator mode. Here, the y-axis is zeroed at the neutral axis of the resonator. To compute the effective ensemble-resonator coupling, we assume a

uniform distribution of properly aligned NV centers within the resonator and sum the individual couplings in quadrature according to $\lambda_{\text{eff}} = \sqrt{\alpha}\sqrt{\sum_{i=1}^{N}\lambda_i^2}$, which gives Eq. 7.6.

7.3 Supplementary Information

7.3.1 Sign of $A_{\parallel}^{\text{e}}$

To confirm the reversal in the sign of the hyperfine coupling $A_{\parallel}$ between the ground state (GS) and excited state (ES) orbitals, we mechanically drive spin population in the ES conditional on the spin state of the ^{14}N nucleus as established within the GS orbital. These measurements follow the pulse sequence depicted in Fig. 7.7a. This modified pulse sequence replaces the hard π-pulses used to quantify $d_{\perp}^{\text{e}}$ in the main text with weak π-pulses conditional on the nuclear spin state.

As shown in Fig. 7.7b, we perform this measurement at the high-field and low-field ES hyperfine resonances. We observe mechanically-driven spin population in the $m_{\text{I}} = +1$ manifold at the $B_z = 80$ G resonance and in the $m_{\text{I}} = -1$ manifold at the $B_z = 109$ G resonance. The resonance condition for spin driving is $\omega_{\text{m}} = 2\gamma_{\text{NV}}B_z + 2A_{\parallel}^{\text{e}}m_{\text{I}}$, giving $A_{\parallel}^{\text{e}} = \left(\frac{1}{2}\omega_{\text{m}} - \gamma_{\text{NV}}B_z\right)/m_{\text{I}}$. Using the parameter values given in the main text, this gives $A_{\parallel}^{\text{e}}/2\pi = +40$ MHz and confirms the sign of $A_{\parallel}^{\text{e}}$.

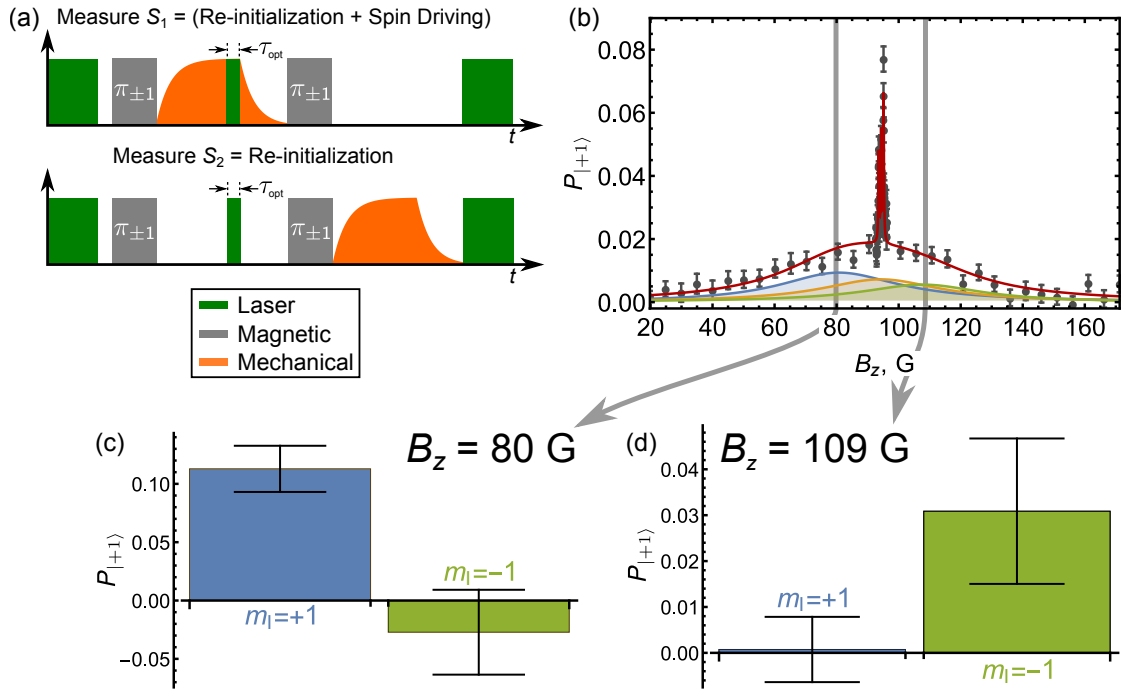

Figure 7.7: (a) Pulse sequence used to verify the sign of $A_{\parallel}^{e}$. (b) Mechanically driven spin contrast as a function of B_z. The red curve is a least squares fit to the sum of six Lorentzians. (c,d) Measurements taken at the (c) low-field and (d) high-field hyperfine resonances that were conditional on the ^{14}N nuclear spin state. The data in (b-d) were measured on a single device with an NV center ensemble, and error bars are from the standard deviation in photon counting.

7.3.2 Ground State Mechanically Driven Rabi Oscillations

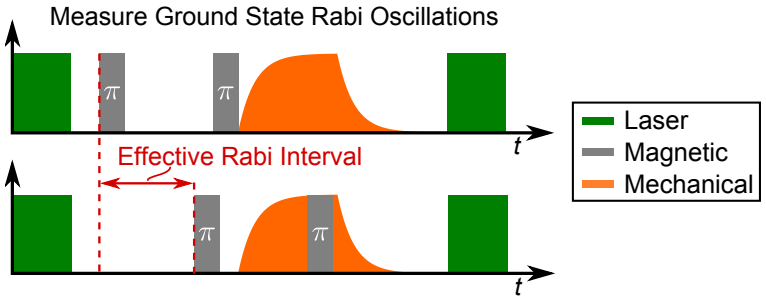

Figure 7.8: Pulse sequence used to measure mechanically driven ground state Rabi oscillations.

The GS mechanically driven Rabi oscillations used to quantify $\Omega_{\rm g}$ were measured using the pulse sequence shown in Fig. 7.8. As described in detail in Ref. [2], varying the pulse length of our mechanical driving field introduces bandwidth-related artifacts to a Rabi measurement. Instead, we fix the length of the mechanical pulse and vary the interaction time by sweeping a pair of magnetic π-pulses through the mechanical pulse. This yields the data seen in Fig. 3a of the main text where the "Effective Rabi Interval" label on the x-axis corresponds to the delay of the π-pulse pair.

For a single NV center, a GS Rabi measurement is described by the function

$$P_{|+1\rangle}(t,\Omega_{\rm g}) = \frac{1}{2}\left\{1 - e^{-t/T_{\rm Rabi}}\cos[\Omega_{\rm g}\tau(t)]\right\} \tag{7.19}$$

where $\tau(t) = \int_0^t \left(1 - e^{-t'/\tau_Q}\right) dt' = \left[\left(e^{-t/\tau_Q} - 1\right)\tau_Q + t\right]$ accounts for the ring-up of the mechanical resonator and $\tau_Q = 2Q/\omega_0$. For an ensemble measurement, we account for spatial inhomogeneities by taking the weighted average of Eq. 7.19 over the PSF of our microscope:

$$P^{\rm ens}_{|+1\rangle} = \frac{\int_0^\infty P_{|+1\rangle}(t,\Omega_{\rm g}|\sin\left[2\pi z/\lambda\right]|)\Gamma_{\rm opt}(z)dz}{\int_0^\infty \Gamma_{\rm opt}(z)dz}. \tag{7.20}$$

Here, we approximate the PSF by the function

$$\Gamma_{\rm opt}(z) = \Gamma_0\left\{\frac{\sin\{\kappa[z_0](z-z_0)\}}{\kappa[z_0](z-z_0)}\right\}^2 \tag{7.21}$$

where Γ_0 is the peak optical pumping rate, $\kappa[z_0]$ defines the depth-dependent PSF width [1], z is the distance below the diamond surface, and $z_0 = 7.9 \pm 0.9\ \mu$m is the focus depth of the PSF. We discretize the integral in Eq. 7.20 and fit each GS Rabi curve, fixing τ_Q to be the same across the fits.

7.3.3 Steady State Phonon Occupancy

Within the two-level toy model used to analyze the proposed cooling protocol, the spin-resonator dynamics for a single NV center coupled to a mechanical resonator are governed by

$$\dot{\rho} = -i[H, \rho] + \mathcal{L}_{\Gamma}\rho + \mathcal{L}_{\gamma}\rho \tag{7.22}$$

where H, $\mathcal{L}_{\Gamma}\rho$, and $\mathcal{L}_{\gamma}\rho$ are defined in the main text. Using these expressions and the ladder operator commutation relations, we derive the system of ordinary differential equations that governs the time evolution of the second order moments [147]. This system is given by

$$\begin{aligned}
&\frac{d}{dt}\langle a^{\dagger}a\rangle = (-i\lambda)\left(\langle S_{+}a^{\dagger}\rangle - \langle S_{-}a\rangle - \langle S_{+}a\rangle + \langle S_{-}a^{\dagger}\rangle\right) + \gamma n_{\text{th}} - \gamma\langle a^{\dagger}a\rangle,\\
&\frac{d}{dt}\langle S_{+}S_{-}\rangle = (-i\lambda)\left(\langle S_{+}a^{\dagger}\rangle - \langle S_{-}a\rangle - \langle S_{-}a^{\dagger}\rangle + \langle S_{+}a\rangle\right) - \Gamma_{\perp}\langle S_{+}S_{-}\rangle,\\
&\frac{d}{dt}\langle S_{+}a^{\dagger}\rangle = (i\lambda)\left(1 + \langle a^{\dagger}a^{\dagger}\rangle + \langle S_{+}S_{+}\rangle + \langle S_{+}S_{-}\rangle + \langle a^{\dagger}a\rangle\right) - \left(\frac{1}{2}\Gamma_{\perp} + \frac{1}{2}\gamma - 2i\omega_{\text{m}} + \Gamma_{\parallel}\right)\langle S_{+}a^{\dagger}\rangle,\\
&\frac{d}{dt}\langle S_{-}a^{\dagger}\rangle = (-i\lambda)\left(\langle a^{\dagger}a\rangle + \langle a^{\dagger}a^{\dagger}\rangle - \langle S_{+}S_{-}\rangle - \langle S_{-}S_{-}\rangle\right) - \left(\frac{1}{2}\Gamma_{\perp} + \frac{1}{2}\gamma + \Gamma_{\parallel}\right)\langle S_{-}a^{\dagger}\rangle,\\
&\frac{d}{dt}\langle S_{+}a\rangle = (i\lambda)\left(\langle a^{\dagger}a\rangle + \langle aa\rangle - \langle S_{+}S_{-}\rangle - \langle S_{+}S_{+}\rangle\right) - \left(\frac{1}{2}\Gamma_{\perp} + \frac{1}{2}\gamma + \Gamma_{\parallel}\right)\langle S_{+}a\rangle,\\
&\frac{d}{dt}\langle S_{-}a\rangle = (-i\lambda)\left(1 + \langle aa\rangle + \langle S_{-}S_{-}\rangle + \langle S_{+}S_{-}\rangle + \langle a^{\dagger}a\rangle\right) - \left(\frac{1}{2}\Gamma_{\perp} + \frac{1}{2}\gamma + 2i\omega_{\text{m}} + \Gamma_{\parallel}\right)\langle S_{-}a\rangle,\\
&\frac{d}{dt}\langle S_{-}S_{-}\rangle = (-2i\lambda)\left(\langle S_{-}a^{\dagger}\rangle + \langle S_{-}a\rangle\right) - \left(\Gamma_{\perp} + 2i\omega_{\text{m}} + \frac{1}{2}\Gamma_{\parallel}\right)\langle S_{-}S_{-}\rangle,\\
&\frac{d}{dt}\langle S_{+}S_{+}\rangle = (2i\lambda)\left(\langle S_{+}a^{\dagger}\rangle + \langle S_{+}a\rangle\right) - \left(\Gamma_{\perp} - 2i\omega_{\text{m}} + \frac{1}{2}\Gamma_{\parallel}\right)\langle S_{+}S_{+}\rangle,\\
&\frac{d}{dt}\langle a^{\dagger}a^{\dagger}\rangle = (2i\lambda)\left(\langle S_{+}a^{\dagger}\rangle + \langle S_{-}a^{\dagger}\rangle\right) - (\gamma - 2i\omega_{\text{m}})\langle a^{\dagger}a^{\dagger}\rangle,
\end{aligned}$$

and

$$\frac{d}{dt}\langle aa\rangle = (-2i\lambda)\left(\langle S_{+}a\rangle + \langle S_{-}a\rangle\right) - (\gamma + 2i\omega_{\text{m}})\langle aa\rangle \tag{7.23}$$

where $\Gamma_{\parallel} = 1/T_{2e}^{*}$, $\Gamma_{\perp} = 1/T_{1e}$, and the other parameters are as defined in the main text.

We make the secular approximation of ignoring the fast-oscillating double-raising and double-lowering terms and solve this system in the limit $\gamma, \lambda \ll \Gamma_{\perp}, \Gamma_{\parallel}$. The time evolution of the phonon occupancy $n = \langle a^{\dagger} a \rangle$ can then be rewritten

$$\frac{dn}{dt} = \gamma \left(n_{\text{th}} - n \right) - \frac{4\lambda^2}{2\Gamma_{\parallel} + \Gamma_{\perp}} n \tag{7.24}$$

as quoted in the main text.

7.3.4 Control Fields for Cooling

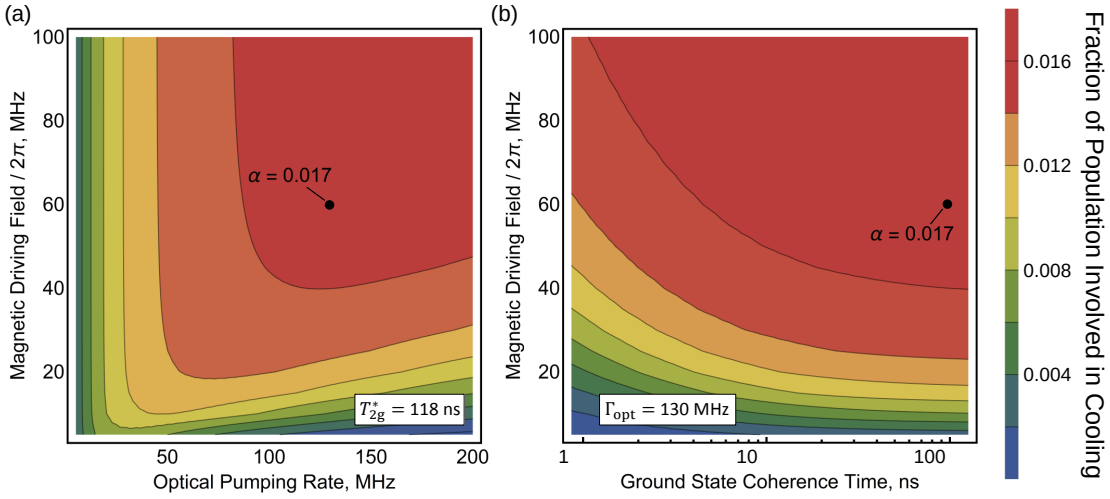

Figure 7.9: The fraction α of the ensemble population involved in the cooling plotted as a function of the magnetic driving field Ω_{mag} and (a) the optical pumping rate Γ_{opt} or (b) the ground state coherence time T_{2g}^{*}.

The proposed cooling protocol requires a static magnetic bias field B_z to bring the spin-strain interaction into resonance, a continuous gigahertz-

frequency magnetic field Ω_{mag} to address the $|g,0\rangle \leftrightarrow |g,-1\rangle$ transition, and continuous optical illumination Γ_{opt} to re-initialize the system.

For the $\omega_0/2\pi = 1$ GHz resonators considered in this work, $B_z = \left(\omega_{\text{m}}/2 - A_{\parallel}\right)/\gamma_{\text{NV}} = 160$ G. The magnitudes of Ω_{mag} and Γ_{opt} determine α, the fraction of the ensemble population involved in the cooling. A large Γ_{opt} is desired to saturate the steady state population in the NV center ES. A large Ω_{mag} is also required to maximize the spin population driven into $|g,-1\rangle$. As shown in Fig. 7.9a, α saturates for large control fields at $\alpha \sim 0.017$. Here, we have used a GS coherence time of $T^*_{2\text{g}} = 118$ ns as reported in Ref. [136] for an NV center ensemble with $\nu = 7 \times 10^{17}$ cm^{-3}.

This low value of α reduces the cooling performance of the proposed protocol and can be understood intuitively by comparing the decay rate from the ES to the GS through the metastable state $|S_1\rangle$ k_{esg} to the rate of decay directly to the GS k_{eg}. Using the rates quoted in Table 1 of the main text, this gives the ratio $k_{\text{esg}}/k_{\text{eg}} \sim 0.02$, which is comparable to $\alpha \sim 0.017$ and suggests that most of the spin population has become trapped in $|S_1\rangle$. Examining the steady state density matrix used to calculate α, we see that this is indeed the case, and $|S_1\rangle$ contains $\sim 73\%$ of the steady state spin population. Without a means of selectively depopulating $|S_1\rangle$, the average fraction of the ensemble involved in the cooling is thus maximized at $\alpha \sim 0.017$.

For the analysis of our cooling protocol presented in the main text, we use $\Omega_{\text{mag}}/2\pi = 60$ MHz and $\Gamma_{\text{opt}} = 130$ MHz, which gives $\alpha = 0.017$. The large Ω_{mag} required to achieve this α has been previously demonstrated in ground state spin control experiments [65], and NV centers are regularly optically pumped to saturation. The scale of these control fields is therefore experimentally reason-

able. As demonstrated by Fig. 7.9b, for $\Omega_{\text{mag}}/2\pi = 60$ MHz and $\Gamma_{\text{opt}} = 130$ MHz, α remains robust until $T^*_{2\text{g}}$ becomes comparable to $T^*_{2\text{e}} = 6$ ns.

7.3.5 Higher Order Mechanical Modes

The eigenfrequencies of the mechanical modes scale with the resonator dimensions as $\omega_n = \kappa_n t/l^2$. For a beam, $\kappa_n = 120, 330, 628, ...$ GHz·μm. We limit our analysis to $\omega_0/2\pi = 1$ GHz resonators. The next order mode of such a resonator will be $\omega_1/2\pi = 2.8$ GHz. Assuming a transform-limited ES linewidth of $\sim 1/T^*_{2\text{e}} = 170$ MHz, the resulting spectral isolation is more than enough to isolate the spin dynamics from higher order mechanical modes.

7.3.6 Validation of Two-Level Model

As the main text explains, to study our proposed cooling protocol we simplify the full seven-level NV center to an effective two-level spin system. To validate our use of this two-state distillation (TSD), we compare the results of the TSD analysis to the cooling predicted a Lamb-Dicke (LD) treatment of the seven-level NV model and to numerical simulations of the full seven-level NV center-plus-resonator Hamiltonian. Our simplification has two potential sources of error: the reduction from the seven-level system to the two-level system for one NV and the scaling from one NV to many NVs.

The LD treatment offers a powerful route to calculating n_{f} when a dissipative, multi-level system such as an NV center spin is coupled to a mechanical resonator and the multi-level system's dynamics are much faster than the res-

onator dynamics. Under the LD approximation, the NV center spin can be adiabatically eliminated from the resonator dynamical equation, and the cooling rate from a single NV center is given by $\Gamma_{c,i} = 2\lambda^2 \{\mathrm{Re}\,[S(\omega_m)] - \mathrm{Re}\,[S(-\omega_m)]\}$. Here, $S(\omega)$ is the spectral function of the ES spin-strain interaction, which we calculate as described in Refs. [154] and [42] for analogous systems. For an ensemble of N spins, the total cooling rate is the sum of the individual rates, giving $\Gamma_c = 2\{\mathrm{Re}\,[S(\omega_m)] - \mathrm{Re}\,[S(-\omega_m)]\}\sum_{i=1}^{N}\lambda_i^2$. This allows us to define the effective ensemble-resonator coupling $\lambda_{\mathrm{eff}} = \sqrt{\sum_{i=1}^{N}\lambda_i^2}$, just as we do in the TSD. In the limit $\gamma n_{\mathrm{th}}, \lambda_{\mathrm{eff}}\sqrt{\langle n\rangle + 1/2} \ll 1/T_{2e}^*, 1/T_{1e}, \omega_m$, the ensemble-resonator coupling can be treated in perturbation theory and the resonator dynamical equation can be solved to find the steady state phonon number

$$n_f^{\mathrm{LD}} = \frac{\Gamma_c N_0 + \gamma n_{\mathrm{th}}}{\Gamma_c + \gamma} \tag{7.25}$$

where $N_0 = \mathrm{Re}\,[S(-\omega_m)] \,/\, \{\mathrm{Re}\,[S(\omega_m)] - \mathrm{Re}\,[S(-\omega_m)]\}$ is the minimal achievable occupancy.

To compare the error in the LD and TSD methods, we numerically solve the seven-level model explicitly, solving for the steady state using the full Hilbert space, similar to the method used in Ref. [155]. To efficiently solve for the steady state ($\mathbf{A}x = 0$) we represent the master equation in superoperator space and explicitly construct the $\mathbf{A}$ matrix as

$$\mathbf{A}x = (-i(\mathbf{I}\otimes H - H\otimes\mathbf{I}) + \tilde{L})x, \tag{7.26}$$

where $x = vec(\rho)$, the vectorization of ρ, constructed by stacking the columns of ρ into a single column vector, H is the Hamiltonian of the system, $\mathbf{I}$ is the identity matrix in the total Hilbert space, and $\tilde{L}$ is the collection of Lindblad superoperators represented in superoperator space. For example, using the single

Lindblad superoperator $\gamma D[a]\rho = \gamma(2a\rho a^\dagger - a^\dagger a\rho - \rho a^\dagger a)$, gives

$$\tilde{L} = \gamma(2a \otimes a - \mathbf{I} \otimes a^\dagger a - a^\dagger a \otimes \mathbf{I}). \tag{7.27}$$

The superoperator form of both H and the Lindblad terms are derived from the identity $\mathbf{AXB} = (\mathbf{B^T} \otimes \mathbf{A})vec(\mathbf{X})$, where $\mathbf{A}, \mathbf{B}$, and $\mathbf{X}$ are all matrices. H in Eq. 7.26 can generally represent any system, but we used the seven-level Hamiltonian of Eq. 9 in the main text (or multiple instances of this, in the case of more than one NV).

$\mathbf{A}$ is an extremely large matrix, but it is also extremely sparse. For our system, $\mathbf{A}$ has less than 10 non-zeros per row, but, for the seven-level Hamiltonian, has matrix dimensions $M^2 \times M^2$, where $M = 7^N n_{\text{ph}}$ and n_{ph} is the largest phonon state accessible in the simulation. We utilize the software package PETSc [157, 158] to perform these large, but very sparse, calculations. $\mathbf{A}$ is stored in compressed sparse row format, ensuring we do the minimal amount of calculations and use the minimum amount of storage. $\mathbf{A}$ is a complex, nonsymmetric matrix, restricting us to use GMRES [156] as our parallel iterative solver, which has slow convergence, especially with increasing system size. Explicitly constructing $\mathbf{A}$ allows us to use efficient preconditioners, such as the additive Schwarz method, to accelerate the convergence. We solve for the steady state rather than doing explicit time dynamics because of the wide separation of time scales in our model. The NV dynamics are very fast, while the cooling is much slower. For an explicit time stepping approach, millions of time steps are necessary to get to the steady state solution, whereas the steady state results typically converge in less than 5000 iterations.

To understand the error from the model reduction, we first focus on simulations using just a single NV. To see significant cooling in manageable computa-

tional time, we increase the spin-strain coupling by a factor of 100 and reduce the resonator frequency to $\omega_{\rm m}/2\pi = 475$ MHz, causing observable cooling but ensuring that the resonator is still only a small perturbation upon the NV center dynamics. We also restrict ourselves to small $n_{\rm th}$ values (equivalently, small temperatures) so that the Hilbert space size needed to approximate the infinite phonon bath is small and the computation remains tractable.

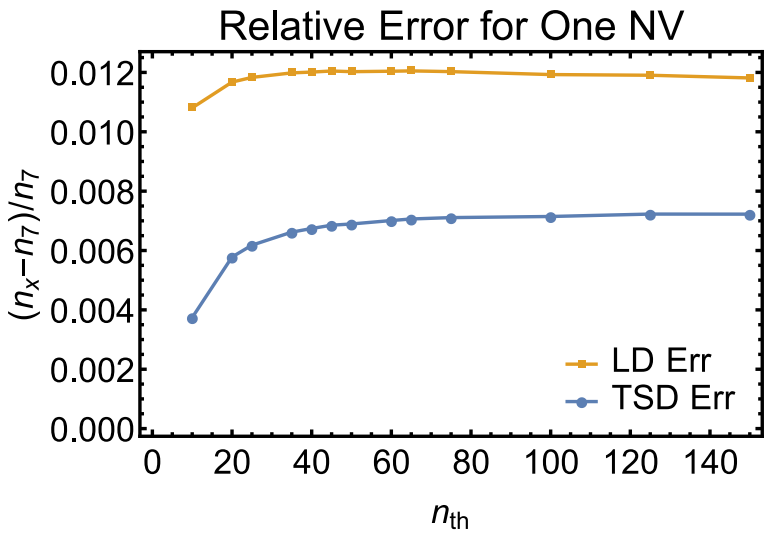

Figure 7.10: Error in the final phonon number predicted by the analytical two-state distillation (TSD) and Lamb-Dicke (LD) treatments compared to that predicted by the numerical seven-level simulation for one NV.

Fig. 7.10 shows the relative error in the final phonon number n_x predicted by the TSD and the LD treatments with respect to that predicted by the seven-level simulation n_7 for one NV center. We see that, compared to LD, the TSD better approximates the numerical simulations at all values of $n_{\rm th}$. As $n_{\rm th}$ increases, the error in the TSD results increases and then levels off at an asymptotic value of less than 0.0075, less than 1% error. At room temperature, where $n_{\rm th}$ is on the order of 10,000 this simplification would only give an error of only 75 phonons in the final phonon number, showing that the TSD is justified, at least for a single NV. Furthermore, it is important to note that both analytical models underesti-

mate the cooling as compared to the numerical simulations. The LD and TSD treatments thus serve as upper bounds on the final phonon number n_f.

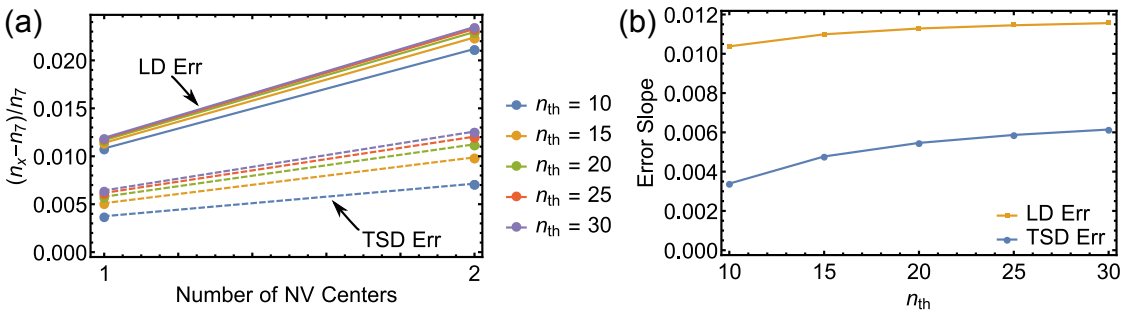

Figure 7.11: (a) Relative error of the analytical two-state distillation (TSD) and Lamb-Dicke (LD) treatments with respect to the numerical seven-level simulation for different numbers of NVs and different n_{th} values. (b) Slope of the lines fit to the curves in (a) plotted as a function of n_{th}.

It is also important to understand how the error scales when the number of NVs is increased. This is a much more computationally challenging task, since each additional seven-level NV increases the total Hilbert space size by a factor of seven. It is only feasible to use two or three NVs, in addition to the mechanical resonator. As such, we did several calculations with one and two NVs, and a few small n_{th} values, as show in Fig. 7.11a. For both TSD and LD, the error gets worse going from one NV to two NVs, but the slope of this change is different for the different n_{th} values. In fact, for both treatments the slope seems to converge with increasing n_{th}, as shown in Fig. 7.11b. While it is hard to make any conclusion about the error for a dense ensemble, we can at least see that the increase in error is such that the two-level simplification is still an upper bound to the cooling, though a slightly worse one. We also did calculations with three NVs where possible, and verified that the linear behavior extends to at least three NVs. Explicitly including enough NVs to see the many NV behavior is computationally intractable, and motivates further theoretical

	$n_{\mathrm{f}}/n_{\mathrm{th}}$	
	$\nu = 2.0 \times 10^{18}$ cm^{-3}	$\nu = 4 \times 10^{20}$ cm^{-3}
Two State Distillation	0.861	0.0300
Lamb-Dicke	0.889	0.0389

Table 7.2: Comparison of different cooling protocol treatments.

study, such as investigations into extensions to the Tavis-Cummings model for systems with more than two states. Nevertheless, these results imply that n_{f} predicted by the analytical models once again serves as an upper bound, and the protocol may cool better than the models suggest.

In all cases examined here, the TSD analysis outperforms LD. Most importantly, as the number of NV centers in the ensemble grows, the TSD error grows more slowly than the LD error. This is because as λ_{eff} grows the spin ensemble becomes less of a perturbation on the resonator and the system departs from the LD regime. More specifically, the approximation $\lambda_{\mathrm{eff}}\sqrt{\langle n\rangle + 1/2} \ll 1/T_{2\mathrm{e}}^{*}, 1/T_{1\mathrm{e}}$ begins to fail. This failure of the LD treatment for dense ensembles at high temperature motivated our development of the TSD analysis. Nevertheless, both methods predict approximately equal cooling power for the device studied in the main text as shown in Table 7.2.

7.3.7 Comparing Different Spin-Strain Interactions

The GS spin-strain interaction could also be employed to cool a mechanical resonator from room temperature. To compare the cooling efficiency of the GS interaction with that of the ES interaction, we compute the ratio of the single-spin

cooperativities

$$\begin{aligned}\frac{\eta_{\mathrm{e}}}{\eta_{\mathrm{g}}} &= \frac{\lambda_{\mathrm{e}}^2 T_{2\mathrm{e}}^*}{\lambda_{\mathrm{g}}^2 T_{2\mathrm{g}}^*} \\ &= \left(\frac{d_\perp^{\mathrm{e}}}{d_\perp^{\mathrm{g}}}\right)^2 \frac{T_{2\mathrm{e}}^*}{T_{2\mathrm{g}}^*} \\ &= (13.5)^2 \, \frac{T_{2\mathrm{e}}^*}{T_{2\mathrm{g}}^*}\end{aligned} \tag{7.28}$$

where the variables are as defined in the main text. As discussed in the main text, effects like exchange narrowing and the truncation of the spin bath make it difficult to predict $T_{2\mathrm{g}}^*$ in a nanostructure. Nevertheless, we can roughly estimate $\eta_{\mathrm{e}}/\eta_{\mathrm{g}}$ by using coherence times measured in bulk diamond.

We first treat the ensemble with an aligned NV center density $\nu = 7.0 \times 10^{17}$ cm^{-3} studied by Ref. [136]. The GS $\{0, -1\}$ qubit coherence time for this ensemble was reported to be $T_{2\mathrm{g}}^{\{0,-1\}} = 118$ ns [136]. Because the spin-strain interaction couples the $|+1\rangle$ and $|-1\rangle$ states, the $\{+1, -1\}$ qubit coherence time sets the single-spin cooperativity. If we assume the spin dephasing is dominated by magnetic field noise, the $\{+1, -1\}$ qubit coherence of this ensemble is $T_{2\mathrm{g}}^{\{+1,-1\}} = 59$ ns. Taking $T_{2\mathrm{e}}^* = 6.0$ ns [150], the ratio of cooperativities becomes $\eta_{\mathrm{e}}/\eta_{\mathrm{g}} = 19$ as quoted in the main text.

For a more moderate density, we turn to the ensemble with $\nu = 2.8 \times 10^{13}$ cm^{-3} measured in Ref. [2], for which $T_{2\mathrm{g}}^{\{+1,-1\}}$ was measured directly to be 450 ns [2]. This gives $\eta_{\mathrm{e}}/\eta_{\mathrm{g}} = 2.4$ as quoted in the main text.

Finally, we note that experimental demonstrations of linewidth narrowing effects in nanostructures suggest that the ES spin coherence of a dense ensemble will remain limited by the motional narrowing rate within a nanostructure [160, 145]. Our analysis of the proposed cooling protocol is thus expected to remain valid, even at very large defect densities.

7.4 Acknowledgments

Research support for Chapter 7 was provided by the Office of Naval Research (ONR) (Grant N000141410812). Device fabrication was performed in part at the Cornell NanoScale Science and Technology Facility, a member of the National Nanotechnology Coordinated Infrastructure, which is supported by the National Science Foundation (Grant ECCS-15420819), and at the Cornell Center for Materials Research Shared Facilities which are supported through the NSF MRSEC program (DMR-1120296). Numerical simulations were performed in part at the Center for Nanoscale Materials, a U.S. Department of Energy Office of Science User Facility under Contract No. DE-AC02-06CH11357. This research used resources of the Oak Ridge Leadership Computing Facility at the Oak Ridge National Laboratory, which is supported by the Office of Science of the U.S. Department of Energy under Contract No. DE-AC05-00OR22725.

CHAPTER 8

CONCLUSION

We trust this has not wearied you, esteemed gentlemen of the panel
and that our research will attain, if not your unmerited theoretical approval,
then at least your paternal consent to carry on failing.
Thank you very much.

– Andrés Neuman (*Talking to Ourselves*)

The measurements described in this thesis have helped lay the experimental foundations for future efforts in NV center spin-optomechanical systems. We have presented the first demonstration of NV center spin transitions driven directly with resonant lattice strain (Chapter 4) and coherent control of NV center spins with a mechanical driving field (Chapter 5). We have employed this mechanical driving to perform continuous dynamical decoupling and extend the spin coherence time of a single NV center (Chapter 6). Finally, we have discovered a spin-strain interaction within the NV center room temperature orbital excited state and theoretically analyzed a dissipative protocol for cooling a mechanical resonator using this coupling (Chapter 7). These results help motivate the development of NV center-mechanical resonator hybrid quantum systems that could be used for precision metrology or as transducers between different quantum degrees of freedom.

BIBLIOGRAPHY

[1] E. R. MacQuarrie, T. A. Gosavi, N. R. Jungwirth, S. A. Bhave, and G. D. Fuchs, Phys. Rev. Lett. **111**, 227602 (2013).

[2] E. R. MacQuarrie, T. A. Gosavi, A. M. Moehle, N. R. Jungwirth, S. A. Bhave, and G. D. Fuchs, Optica **2**, 233 (2015).

[3] E. R. MacQuarrie, T. A. Gosavi, S. A. Bhave, and G. D. Fuchs, Phys. Rev. B **92**, 224419 (2015).

[4] E. R. MacQuarrie, M. Otten, S. K. Gray, and G. D. Fuchs, Nat. Commun. **8**, 14358 (2017).

[5] C. A. Klein and G. F. Cardinale, Diamond Relat. Mater. **2**, 918 (1993).

[6] M. W. Doherty, F. Dolde, H. Fedder, F. Jelezko, J. Wrachtrup, N. B. Manson, and L. C. L. Hollenberg, Phys. Rev. B **85**, 205203 (2012).

[7] M. W. Doherty, N. B. Manson, P. Delaney, F. Jelezko, J. Wrachtrup, and L. C. L. Hollenberg, Phys. Rep. **528**, 1 (2013).

[8] N. Bar-Gill, L. M. Pham, A. Jarmola, D. Budker, and R. L. Walsworth, Nat. Commun. **4**, 1743 (2013).

[9] J. R. Maze, P. L. Stanwix, J. S. Hodges, S. Hong, J. M. Taylor, P. Capellaro, L. Jiang, M. V. G. Dutt, E. Togan, A. S. Zibrov, A. Yacoby, R. L. Walsworth, and M. D. Lukin, Nature **455**, 644 (2008).

[10] G. Balasubramanian, I. Y. Chan, R. Kolesov, M. Al-Hmoud, J. Tisler, C. Shin, C. Kim, A. Wojcik, P. R. Hemmer, A. Krueger, T. Hanke, A. Leitenstorfer, R. Bratschitsch, F. Jelezko, and J. Wrachtrup, Nature **455**, 648 (2008).

[11] P. Maletinsky, S. Hong, M. S. Grinolds, B. Hausmann, M. D. Lukin, R. L. Walsworth, M. Lončar, and A. Yacoby, Nat. Nanotechnol. **7**, 320 (2012).

[12] M. S. Grinolds, S. Hong, P. Maletinsky, L. Luan, M. D. Lukin, R. L. Walsworth, and A. Yacoby, Nat. Phys. **9**, 215 (2013).

[13] V. M. Acosta, E. Bauch, M. P. Ledbetter, A. Waxman, L.-S. Bouchard, and D. Budker, Phys. Rev. Lett. **104**, 070801 (2010).

[14] D. M. Toyli, C. F. de las Casas, D. J. Christle, V. V. Dobrovitski, and D. D. Awschalom, Proc. Natl. Acad. Sci. USA **110**, 8417 (2013).

[15] G. Kucsko, P. C. Maurer, N. Y. Yao, M. Kubo, H. J. Noh, P. K. Lo, H. Park, and M. D. Lukin, Nature **500**, 54 (2013).

[16] F. Dolde, H. Fedder, M. W. Doherty, T. Nöbauer, F. Rempp, G. Balasubramanian, T. Wolf, F. Reinhard, L. C. L. Hollenberg, F. Jelezko, and J. Wrachtrup, Nat. Phys. **7**, 459 (2011).

[17] T. H. Taminiau, J. Cramer, T. van der Sar, V. V. Dobrovitski, and R. Hanson, Nat. Nanotechnol. **9**, 171 (2014).

[18] W. Pfaff, B. J. Hensen, H. Bernien, S. B. van Dam, M. S. Blok, T. H. Taminiau, M. J. Tiggelman, R. N. Schouten, M. Markham, D. J. Twitchen, and R. Hanson, Science **345**, 532 (2014).

[19] B. Hensen, H. Bernien, A. E. Dréau, A. Reiserer, N. Kalb, M. S. Blok, J. Ruitenberg, R. F. L. Vermeulen, R. N. Schouten, C. Abellán, W. Amaya, V. Pruneri, M. W. Mitchell, M. Markham, J. Twitchen, D. Elkouss, S. Wehner, T. H. Taminiau, and R. Hanson, Nature **526**, 682 (2015).

[20] P. Rabl, S. J. Kolkowitz, F. H. L. Koppens, J. G. E. Harris, and P. Z. M. D. Lukin, Nat. Phys. **6**, 602 (2010).

[21] K. Stannigel, P. Rabl, A. S. Sørensen, P. Zoller, and M. D. Lukin, Phys. Rev. Lett. **105**, 220501 (2010).

[22] S. J. M. Habraken, K. Stannigel, M. D. Lukin, P. Zoller, and P. Rabl, New J. Phys. **14**, 115004 (2012).

[23] P. R. Hemmer, A. V. Turukhin, M. S. Shahriar, and J. A. Musser, Opt. Lett. **26**, 361 (2001).

[24] E. Togan, Y. Chu, A. S. Trifonov, L. Jiang, J. Maze, L. Childress, M. V. G. Dutt, A. S. S. rensen, P. R. Hemmer, A. S. Zibrov, and M. D. Lukin, Nature **466**, 730 (2010).

[25] D. I. Schuster, A. P. Sears, E. Ginossar, L. DiCarlo, L. Frunzio, J. J. L. Morton, H. Wu, G. A. D. Briggs, B. B. Buckley, D. D. Awschalom, and R. J. Schoelkopf, Phys. Rev. Lett. **105**, 140501 (2010).

[26] Y. Kubo, F. R. Ong, P. Bertet, D. Vion, V. Jacques, D. Zheng, A. Dréau, J.-F. Roch, A. Auffeves, F. Jelezko, J. Wrachtrup, M. F. Barthe, P. Bergonzo, and D. Esteve, Phys. Rev. Lett. **105**, 140502 (2010).

[27] R. Amsüss, C. Koller, T. Nöbauer, S. Putz, S. Rotter, K. Sandner, S. Schneider, M. Schramböck, G. Steinhauser, H. Ritsch, J. Schmiedmayer, and J. Majer, Phys. Rev. Lett. **107**, 060502 (2011).

[28] C. G. Yale, B. B. Buckley, D. J. Christle, G. Burkard, F. J. Heremans, L. C. Bassett, and D. D. Awschalom, Proc. Natl. Acad. Sci. USA **110**, 19 (2013).

[29] D. A. Golter, T. Oo, M. Amezcua, K. A. Stewart, and H. Wang, Phys. Rev. Lett. **116**, 143602 (2016).

[30] K. W. Lee, D. Lee, P. Ovartchaiyapong, J. Minguzzi, J. R. Maze, and A. C. Bleszynski Jayich, Phys. Rev. Applied **6**, 034005 (2016).

[31] J. Teissier, A. Barfuss, P. Appel, E. Neu, and P. Maletinsky, Phys. Rev. Lett. **113**, 020503 (2014).

[32] P. Ovartchaiyapong, K. W. Lee, B. A. Myers, and A. C. Bleszynski Jayich, Nat. Commun. **5**, 4429 (2014).

[33] A. Barfuss, J. Teissier, E. Neu, A. Nunnenkamp, and P. Maletinsky, Nat. Phys. **11**, 820 (2015).

[34] K.-M. C. Fu, C. Santori, P. E. Barclay, L. J. Rogers, N. B. Manson, and R. G. Beausoleil, Phys. Rev. Lett. **103**, 256404 (2009).

[35] P. Rabl, P. Cappellaro, M. V. G. Dutt, L. Jiang, J. R. Maze, and M. D. Lukin, Phys. Rev. B **79**, 041302 (2009).

[36] O. Arcizet, V. Jacques, A. Siria, P. Poncharal, P. Vincent, and S. Seidelin, Nat. Phys. **7**, 879 (2011).

[37] S. Kolkowitz, A. C. Bleszynski Jayich, Q. P. Unterreithmeier, S. D. Bennett, P. Rabl, J. G. E. Harris, and M. D. Lukin, Science **335**, 6076 (2012).

[38] S. Hong, M. S. Grinolds, P. Maletinsky, R. L. Walsworth, M. D. Lukin, and A. Yacoby, Nano Lett. **12**, 3920 (2012).

[39] S. D. Bennett, S. Kolkowitz, Q. P. Unterreithmeier, P. Rabl, A. C. Bleszynski Jayich, J. G. E. Harris, and M. D. Lukin, New J. Phys. **14**, 125004 (2012).

[40] P.-B. Li, Z.-L. Xiang, P. Rabl, and F. Nori, Phys. Rev. Lett. **117**, 015502 (2016).

[41] S. D. Bennett, N. Y. Yao, J. Otterbach, P. Zoller, P. Rabl, and M. D. Lukin, Phys. Rev. Lett. **110**, 156402 (2013).

[42] K. V. Kepesidis, S. D. Bennett, S. Portolan, M. D. Lukin, and P. Rabl, Phys. Rev. B **88**, 064105 (2013).

[43] G. Davies and M. F. Hamer, Proc. R. Soc. Lond. A **348**, 285 (1976).

[44] A. Mainwood, Phys. Rev. B **49**, 7934 (1994).

[45] D. A. Feld, R. Parker, R. Ruby, P. Bradley, and S. Dong, Ultrasonics Symposium, 2008. IUS 2008. IEEE pp. 431–436 (2008).

[46] M. J. Burek, N. P. de Leon, B. J. Shields, B. J. M. Hausmann, Y. Chu, Q. Quan, A. S. Zibrov, H. Park, M. D. Lukin, and M. Lončar, Nano Lett. **12**, 6084 (2012).

[47] B. Khanaliloo, H. Jayakumar, A. C. Hryciw, D. P. Lake, H. Kaviani, and P. E. Barclay, Phys. Rev. X **5**, 041051 (2015).

[48] M. Mitchell, B. Khanaliloo, D. P. Lake, T. Masuda, J. P. Hadden, and P. E. Barclay, Optica **3**, 963 (2016).

[49] M. J. Burek, J. D. Cohen, S. M. Meenehan, N. El-Sawah, C. Chia, T. Ruelle, S. Meesala, J. Rochman, H. A. Atikian, M. Markham, D. J. Twitchen, M. D. Lukin, O. Painter, and M. Lončar, Optica **3**, 1404 (2016).

[50] S. Meesala, Y.-I. Sohn, H. A. Atikian, S. Kim, M. J. Burek, J. T. Choy, and M. Lončar, Phys. Rev. Applied **5**, 034010 (2016).

[51] B. A. Myers, A. Das, M. C. Dartiailh, K. Ohno, D. D. Awschalom, and A. C. Bleszynski Jayich, Phys. Rev. Lett. **113**, 027602 (2014).

[52] Y.-I. Sohn, M. J. Burek, V. Kara, R. Kearns, and M. Lončar, Appl. Phys. Lett. **107**, 243106 (2015).

[53] A. Albrecht, A. Retzke, F. Jelezko, and M. B. Plenio, New J. Phys. **15**, 083014 (2013).

[54] H. Bernien, B. Hensen, W. Pfaff, G. Koolstra, M. S. Blok, L. Robledo, T. H. Taminiau, M. Markham, D. J. Twitchen, L. Childress, and R. Hanson, Nature **497**, 86 (2013).

[55] L. Childress, M. V. Gurudev Dutt, J. M. Taylor, A. S. Zibrov, F. Jelezko, J. Wrachtrup, P. R. Hemmer, and M. D. Lukin, Science **314**, 5797 (2006).

[56] K. Fang, V. M. Acosta, C. Santori, Z. Huang, K. M. Itoh, H. Watanabe, S. Shikata, and R. G. Beausoleil, Phys. Rev. Lett. **110**, 130802 (2013).

[57] D. M. Toyli, C. F. de las Casas, D. J. Christle, V. V. Dobrovitski, and D. D. Awschalom, Proc. Natl. Acad. Sci. USA **110**, 8417 (2013).

[58] G. Kucsko, P. C. Maurer, N. Y. Yao, M. Kubo, H. J. Noh, P. K. Lo, H. Park, and M. D. Lukin, Nature **500**, 54 (2013).

[59] H. J. Mamin, M. Kim, M. H. Sherwood, C. T. Rettner, K. Ohno, D. D. Awschalom, and D. Rugar, Science **339**, 6119 (2013).

[60] T. Staudacher, F. Shi, S. Pezzagna, J. Meijer, J. Du, C. A. Meriles, F. Reinhard, and J. Wrachtrup, Science **339**, 6119 (2013).

[61] B. D'Urso, M. V. G. Dutt, S. Dhingra, and N. M. Nusran, New J. Phys. **13**, 4 (2011).

[62] P. Ovartchaiyapong, L. M. A. Pascal, B. A. Myers, P. Lauria, and A. C. Bleszynski Jayich, Appl. Phys. Lett. **101**, 163505 (2012).

[63] V. V. Dobrovitski, G. D. Fuchs, A. L. Falk, C. Santori, and D. D. Awschalom, Annu. Rev. Cond. Mat. Phys. **4**, 23 (2013).

[64] F. Jelezko, T. Gaebel, I. Popa, A. Gruber, and J. Wrachtrup, Phys. Rev. Lett. **92**, 076401 (2004).

[65] G. D. Fuchs, V. V. Dobrovitski, D. M. Toyli, F. J. Heremans, and D. D. Awschalom, Science **326**, 1520 (2009).

[66] C. G. Yale, B. B. Buckley, D. J. Christle, G. Burkard, F. J. Heremans, L. C. Bassett, and D. D. Awschalom, Proc. Natl. Acad. Sci. USA **110**, 7595 (2013).

[67] D. I. Bolef and R. K. Sundfors, *Nuclear Acoustic Resonance* (Acedemic Press, 1993).

[68] K. M. Lakin, G. R. Kline, and K. T. McCarron, Microwave Symposium Digest, 1993., IEEE MTT-S International pp. 1517–1520 (1993).

[69] K. F. Graff, *Wave Motion in Elastic Solids* (Dover Publications, 1991).

[70] C. P. Slichter, *Princples of Magnetic Resonance* (Springer, 1990), 3rd ed.

[71] E. Vanoort and M. Glasbeek, Chem. Phys. Lett. **168**, 529 (1990).

[72] S. Hell, G. Reiner, C. Cremer, and E. H. K. Stelzer, J. Microsc. **169**, 3 (1993).

[73] B. P. Sorokin, G. M. Kvashnin, A. P. Volkov, V. S. Bormashov, V. V. Aksenenkov, M. S. Kuznetsov, G. I. Gordeev, and A. V. Telichko, Appl. Phys. Lett. **102**, 113507 (2013).

[74] T. Cheng, J. Hsiao, S. A. Bhave, and A. Duwel, in preparation (2013).

[75] A. Ajoy and P. Cappellaro, Phys. Rev. A **86**, 062104 (2012).

[76] M. P. Ledbetter, K. Jensen, R. Fischer, A. Jarmola, and D. Budker, Phys. Rev. A **86**, 052116 (2012).

[77] P. L. Stanwix, L. M. Pham, J. R. Maze, D. L. Sage, T. K. Yeung, P. Cappellaro, P. R. Hemmer, A. Yacoby, M. D. Lukin, and R. L. Walsworth, Phys. Rev. B **82**, 201201(R) (2010).

[78] F. Irgens, *Continuum Mechanics* (Springer, 2008).

[79] C. A. Klein and G. F. Cardinale, Diamond Relat. Mater. **2**, 918 (1993).

[80] B. Smeltzer, J. McIntyre, and L. Childress, Phys. Rev. A **80**, 050302(R) (2009).

[81] M. Steiner, P. Neumann, J. Beck, F. Jelezko, and J. Wrachtrup, Phys. Rev. B **81**, 035205 (2010).

[82] O. O. Soykal, R. Ruskov, and C. Tahan, Phys. Rev. Lett. **107**, 235502 (2011).

[83] R. Hanson, V. V. Dobrovitski, A. E. Feiguin, O. Gywat, and D. D. Awschalom, Science **320**, 5874 (2008).

[84] E. Togan, Y. Chu, A. Imamoglu, and M. D. Lukin, Nature **478**, 497 (2011).

[85] M. J. Burek, D. Ramos, R. Patel, I. W. Frank, and M. Lončar, Appl. Phys. Lett. **103**, 131904 (2013).

[86] H. J. Mamin, M. H. Sherwood, M. Kim, C. T. Rettner, K. Ohno, D. D. Awschalom, and D. Rugar, Phys. Rev. Lett. **113**, 030803 (2014).

[87] C. D. Aiello, M. Hirose, and P. Cappellaro, Nat. Commun. **4**, 1419 (2013).

[88] W. M. Seibert, *Circuits, Signals, and Systems* (The MIT Press, 1985).

[89] X. Xu, Z. Wang, C. Duan, P. Huang, P. Wang, Y. Wang, N. Xu, X. Kong, F. Shi, X. Rong, and J. Du, Phys. Rev. Lett. **109**, 070502 (2012).

[90] P. Huang, X. Kong, N. Zhao, F. Shi, P. Wang, X. Rong, R. B. Liu, and J. Du, Nat. Commun. **2**, 570 (2011).

[91] V. V. Dobrovitski, A. E. Feiguin, D. D. Awschalom, and R. Hanson, Phys. Rev. B **77**, 245212 (2008).

[92] C. Santori, D. Fattal, S. M. Spillane, M. Fiorentino, R. G. Beausoleil, A. D. Greentree, P. Olivero, M. Draganski, J. R. Rabeau, P. Reichart, B. C. Gibson, S. Rubanov, D. N. Jamieson, and S. Prawer, Opt. Expr. **14**, 17 (2006).

[93] C. Santori, P. Tamarat, P. Neumann, J. Wrachtrup, D. Fattal, R. G. Beausoleil, J. Rabeau, P. Olivero, A. D. Greentree, S. Prawer, F. Jelezko, and P. Hemmer, Phys. Rev. Lett. **97**, 247401 (2006).

[94] V. M. Acosta, K. Jensen, C. Santori, D. Budker, and R. G. Beausoleil, Phys. Rev. Lett. **110**, 213605 (2013).

[95] S. J. Buckle, S. M. Barnett, P. L. Knight, M. A. Lauder, and D. T. Pegg, Opt. Acta. **33**, 9 (1986).

[96] M. S. Shahriar and P. R. Hemmer, Phys. Rev. Lett. **65**, 1865 (1990).

[97] D. V. Kosachiov, B. G. Matisov, and Y. V. Rozhdestvensky, J. Phys. B: At. Mol. Opt. Phys. **25**, 2473 (1992).

[98] R. Schirhagl, K. Chang, M. Loretz, and C. L. Degen, Annu. Rev. Phys. Chem. **65**, 83 (2014).

[99] L. Childress, M. V. G. Dutt, J. M. Taylor, A. S. Zibrov, F. Jelezko, J. Wrachtrup, P. R. Hemmer, and M. D. Lukin, Science **314**, 5797 (2006).

[100] G. de Lange, Z. H. Wang, D. Ristè, V. V. Dobrovitski, and R. Hanson, Science **330**, 6000 (2010).

[101] C. A. Ryan, J. S. Hodges, and D. G. Cory, Phys. Rev. Lett. **105**, 200402 (2010).

[102] G. de Lange, D. Ristè, V. V. Dobrovitski, and R. Hanson, Phys. Rev. Lett. **106**, 080802 (2011).

[103] B. Naydenov, F. Dolde, L. T. Hall, C. Shin, H. Fedder, L. C. L. Hollenberg, F. Jelezko, and J. Wrachtrup, Phys. Rev. B **83**, 081201(R) (2011).

[104] Z.-H. Wang, G. de Lange, D. Ristè, R. Hanson, and V. V. Dobrovitski, Phys. Rev. B **85**, 155204 (2012).

[105] T. van der Sar, Z. H. Wang, M. S. Blok, H. Bernien, T. H. Taminiau, D. M. Toyli, D. A. Lidar, D. D. Awschalom, R. Hanson, and V. V. Dobrovitski, Nature **484**, 82 (2012).

[106] N. Timoney, I. Baumgert, M. Johanning, A. F. Varón, M. B. Plenio, A. Retzker, and C. Wunderlich, Nature **476**, 185 (2011).

[107] H. Fedder, F. Dolde, F. Rempp, T. Wolf, P. Hemmer, F. Jelezko, and J. Wrachtrup, Appl. Phys. B **102**, 497 (2011).

[108] X. Xu, Z. Wang, C. Duan, P. Huang, P. Wang, Y. Wang, N. Xu, X. Kong, F. Shi, X. Rong, and J. Du, Phys. Rev. Lett. **109**, 070502 (2012).

[109] M. Hirose, C. D. Aiello, and P. Cappellaro, Phys. Rev. A **86**, 062320 (2012).

[110] V. V. Mkhitaryan and V. V. Dobrovitski, Phys. Rev. B **89**, 224402 (2014).

[111] D. A. Golter, T. K. Baldwin, and H. Wang, Phys. Rev. Lett. **113**, 237601 (2014).

[112] Y. Matsuzaki, X. Zhu, K. Kakuyanagi, H. Toida, T. Shimo-Oka, N. Mizuochi, K. Nemoto, K. Semba, W. J. Munro, H. Yamaguchi, and S. Saito, Phys. Rev. Lett. **114**, 120501 (2015).

[113] V. V. Mkhitaryan, F. Jelezko, and V. V. Dobrovitski, Sci. Rep. **5**, 15402 (2015).

[114] J.-M. Cai, B. Naydenov, R. Pfeiffer, L. P. McGuinness, K. D. Jahnke, F. Jelezko, M. B. Plenio, and A. Retzker, New J. Phys. **14**, 113023 (2012).

[115] S. K. Mishra, L. Chotorlishvili, A. R. P. Rau, and J. Berakdar, Phys. Rev. A **90**, 033817 (2014).

[116] M. W. Doherty, V. M. Acosta, A. Jarmola, M. S. J. Barson, N. B. Manson, D. Budker, and L. C. L. Hollenberg, Phys. Rev. B **90**, 041201 (2014).

[117] G. Ithier, E. Collin, P. Joyez, P. J. Meeson, D. Vion, D. Esteve, F. Chiarello, A. Shnirman, Y. Makhlin, J. Schriefl, and G. Schön, Phys. Rev. B **72**, 134519 (2005).

[118] A. Bermudez, F. Jelezko, M. B. Plenio, and A. Retzker, Phys. Rev. Lett. **107**, 150503 (2011).

[119] P. Siyushev, F. Kaiser, V. Jacques, I. Gerhardt, S. Bischof, H. Fedder, J. Dodson, M. Markham, D. Twitchen, F. Jelezko, and J. Wrachtrup, Appl. Phys. Lett. **97**, 241902 (2010).

[120] T. R. Albrecht, P. Grütter, D. Horne, and D. Rugar, J. Appl. Phys. **69**, 668 (1991).

[121] A. N. Cleland and M. L. Roukes, Nature **392**, 160 (1998).

[122] D. Rugar, R. Budakian, H. J. Mamin, and B. W. Chui, Nature **430**, 329 (2004).

[123] M. Poggio, C. L. Degen, H. J. Mamin, and D. Rugar, Phys. Rev. Lett. **99**, 017201 (2007).

[124] A. D. O'Connell, M. Hofheinz, M. Ansmann, R. C. Bialczak, M. Lenander, E. Lucero, M. Neeley, D. Sank, H. Wang, M. Weides, J. Wenner, J. M. Martinis, and A. N. Cleland, Nature **464**, 697 (2010).

[125] J. Chan, T. P. M. Alegre, A. H. Safavi-Naeini, J. T. Hill, A. Krause, S. Gröblacher, M. Aspelmeyer, and O. Painter, Nature **478**, 89 (2011).

[126] J. D. Teufel, T. Donner, D. Li, J. W. Harlow, M. S. Allman, K. Cicak, A. J. Sirois, J. D. Whittaker, K. W. Lehnert, and R. W. Simmonds, Nature **475**, 359 (2011).

[127] C. H. Metzger and K. Karrai, Nature **432**, 1002 (2004).

[128] S. Gigan, H. R. Böhm, M. Paternostro, F. Blaser, G. Langer, J. B. Hertzberg, K. C. Schwab, D. Bäuerle, M. Aspelmeyer, and A. Zeilinger, Nature **444**, 67 (2006).

[129] O. Arcizet, P.-F. Cohadon, T. Briant, M. Pinard, and A. Heidmann, Nature **444**, 71 (2006).

[130] D. Kleckner and D. Bouwmeester, Nature **444**, 75 (2006).

[131] A. Schliesser, P. Del'Haye, N. Nooshi, K. J. Vahala, and T. J. Kippenberg, Phys. Rev. Lett. **97**, 243905 (2006).

[132] M. Mitchell, B. Khanaliloo, D. P. Lake, T. Masuda, J. P. Hadden, and P. E. Barclay, Optica **3**, 963 (2016).

[133] Y. Ma, Z.-q. Yin, P. Huang, W. L. Yang, and J. Du, Phys. Rev. A **94**, 053836 (2016).

[134] H.-K. Lau and M. B. Plenio, Phys. Rev. B **94**, 054305 (2016).

[135] C. Kittel and E. Abrahams, Phys. Rev. **90**, 238 (1953).

[136] V. M. Acosta, E. Bauch, M. P. Ledbetter, C. Santori, K.-M. C. Fu, P. E. Barclay, R. G. Beausoleil, H. Linget, J. F. Roch, F. Treussart, S. Chemerisov, W. Gawlik, and D. Budker, Phys. Rev. B **80**, 115202 (2009).

[137] A. Batalov, V. Jacques, F. Kaiser, P. Siyushev, P. Neumann, L. J. Rogers, R. L. McMurtrie, N. B. Manson, F. Jelezko, and J. Wrachtrup, Phys. Rev. Lett. **102**, 195506 (2009).

[138] L. J. Rogers, R. L. McMurtrie, M. J. Sellars, and N. B. Manson, New J. Phys. **11**, 063007 (2009).

[139] T. Plakhotnik, M. W. Doherty, and N. B. Manson, Phys. Rev. B **92**, 081203 (2015).

[140] G. D. Fuchs, V. V. Dobrovitski, R. Hanson, A. Batra, C. D. Weis, T. Schenkel, and D. D. Awschalom, Phys. Rev. Lett. **101**, 117601 (2008).

[141] G. D. Fuchs, V. V. Dobrovitski, D. M. Toyli, F. J. Heremans, C. D. Weis, T. Schenkel, and D. D. Awschalom, Nat. Phys. **6**, 668 (2010).

[142] A. Gali, M. Fyta, and E. Kaxiras, Phys. Rev. B **77**, 155206 (2008).

[143] T.-L. Wee, Y.-K. Tzeng, C.-C. Han, H.-C. Chang, W. Fann, J.-H. Hsu, K.-M. Chen, and Y.-C. Yu, J. Phys. Chem. A **111**, 9379 (2007).

[144] S. Choi, J. Choi, G. Kucscko, P. C. Maurer, B. J. Shields, H. Sumiya, S. Onoda, J. Isoya, E. Demler, F. Jelezko, N. Y. Yao, and M. D. Lukin, arXiv:1608.05471 (2016).

[145] P. G. Baranov, A. A. Soltamova, D. O. Tolmachev, N. G. Romanov, R. A. Babunts, F. M. Shakhov, S. V. Kidalov, A. Y. Vul, G. V. Mamin, S. B. Orlinskii, and N. I. Silkin, Small **7**, 1533 (2011).

[146] E. T. Jaynes and F. W. Cummings, Proceedings of the IEEE **51**, 89 (1963).

[147] I. Wilson-Rae, N. Nooshi, J. Dobrindt, T. J. Kippenberg, and W. Zwerger, New J. Phys. **10**, 095007 (2008).

[148] M. Tavis and F. W. Cummings, Phys. Rev. **170**, 379 (1968).

[149] B. M. Garraway, Phil. Trans. R. Soc. A **369**, 1137 (2011).

[150] G. D. Fuchs, A. L. Falk, V. V. Dobrovitski, and D. D. Awschalom, Phys. Rev. Lett. **108**, 157602 (2012).

[151] L. Robledo, H. Bernien, T. van der Sar, and R. Hanson, New J. Phys. **13**, 025013 (2011).

[152] V. Jacques, P. Neumann, J. Beck, M. Markham, D. Twitchen, J. Meijer, F. Kaiser, G. Balasubramanian, F. Jelezko, and J. Wrachtrup, Phys. Rev. Lett. **102**, 057403 (2009).

[153] R. Tabrizian, M. Rais-Zadeh, and F. Ayazi, in *Solid-State Sensors, Actuators and Microsystems Conference, 2009. TRANSDUCERS 2009.* (IEEE, 2009), pp. 2131–2134.

[154] K. Jaehne, K. Hammerer, and M. Wallquist, New J. Phys. **10**, 095019 (2008).

[155] M. Otten, R. A. Shah, N. F. Scherer, M. Min, M. Pelton, and S. K. Gray, Phys. Rev. B **92**, 125432 (2015).

[156] Y. Saad and M. Schultz, SIAM J. Sci. Comput. **7**, 856 (1986).

[157] S. Balay, S. Abhyankar, M. F. Adams, J. Brown, P. Brune, K. Buschelman, L. Dalcin, V. Eijkhout, W. D. Gropp, D. Kaushik, M. G. Knepley, L. C. McInnes, K. Rupp, B. F. Smith, S. Zampini, H. Zhang, and H. Zhang, Tech. Rep. ANL-95/11 - Revision 3.7, Argonne National Laboratory (2016).

[158] S. Balay, W. D. Gropp, L. C. McInnes, and B. F. Smith, in *Modern Software Tools in Scientific Computing*, edited by E. Arge, A. M. Bruaset, and H. P. Langtangen (Birkhäuser Press, 1997), pp. 163–202.

[159] Y. Tao, J. M. Boss, B. A. Moores, and C. L. Degen, Nat. Commun. **5**, 3638 (2014).

[160] M. J. A. Smith, B. R. Angel, and R. G. Emmons, Nature **210**, 692 (1966).

[161] A. H. Safavi-Naeini, J. Chan, J. T. Hill, T. P. M. Alegre, A. Krause, and O. Painter, Phys. Rev. Lett. **108**, 033602 (2012).